Acta Polytechnica

Editorial Board:

Zdeněk P. Bažant
Northwestern University McCormick School of Engineering, Illinois, USA

Lenka Bodnárová
Brno University of Technology, Czech Republic, Czech Republic

Steffen Bohrmann
Hochschule Mannheim University of Applied Sciences, Germany

Reinhard Harte
Department of Civil Engineering, Bergische Universität, Wuppertal, Germany

Taťána Jarošíková
Faculty of Biomedical Engineering, Czech Technical University in Prague, Czech Republic

Jitka Jírová
Faculty of Transportation Sciences, Czech Technical University in Prague, Czech Republic

Petr Jizba
Faculty of Nuclear Sciences and Physical Engineering, Czech Technical University in Prague, Czech Republic

Pavel Kalina
Faculty of Architecture, Czech Technical University in Prague, Czech Republic

Tomáš Kozik
Department of Technology and Information Technologies, Constantine the Philosopher University in Nitra, Slovakia

František Kraus
ETH Zürich, Switzerland

Libor Makovička
Université de Franche Comté, France, France

Zuzana Masáková
Faculty of Nuclear Sciences and Physical Engineering, Czech Technical University in Prague, Czech Republic

David Murray-Smith
School of Engineering, University of Glasgow, United Kingdom

Drahomír Novák
Faculty of Civil Engineering, Brno University of Technology, Czech Republic

Marián Peciar
Institute of Chemical and Hydraulic Machines and Equipment (FME), Slovak University of Technology in Bratislava, Slovakia

Jan Píchal
Faculty of Electrical Engineering, Czech Technical University in Prague, Czech Republic

Miroslav Sýkora
Klokner Institute, Czech Technical University in Prague, Czech Republic

Zbyněk Škvor (Head of Editorial Board)
Faculty of Electrical Engineering, Department of Electromagnetic Field, Czech Technical University in Prague, Czech Republic

Radek Šulc
Faculty of Mechanical Engineering, Czech Technical University in Prague, Czech Republic

Martin Vohralík
INRIA de Paris, Institut universitaire de technologie, France

Pavel Trtik
Paul Scherrer Institut (PSI), Villigen, Switzerland, Switzerland

Jan Zeman
Faculty of Civil Engineering, Czech Technical University in Prague, Czech Republic

Title of journal: ACTA POLYTECHNICA. **Volume:** 62. **Number:** 4.
Periodicity: Bimonthly; 6 issues per year. **Date of issue:** August 31, 2022.
Published by: Czech Technical University in Prague,
Jugoslávských partyzánů 1580/3, 160 00 Praha 6 – Dejvice, Czech Republic.
IČO: 68407700.

Editorial Office: CTU — Central Library,
Technická 6, 160 80 Praha 6, Czech Republic.
`acta@cvut.cz`

Acta Polytechnica is available at `http://ojs.cvut.cz/ojs/index.php/ap`
Each article is assigned a digital object identifier `https://doi.org/10.14311/AP.2022.62.`⟨*4-digit article page number*⟩

ISSN 1805–2363 (online) MK ČR E 4923

Dear Reader

The Acta Polytechnica journal that you have just opened is a scientific journal published by the Czech Technical University in Prague. This journal first appeared in 1961 under the name "Proceedings of the Czech Technical University". The main purpose of the journal was to support publication of the results of scientific and research activities at the Czech technical universities. Five years later, in 1966, the name of the journal was changed to Acta Polytechnica, and it started appearing quarterly. The main title Acta Polytechnica is accompanied by the subtitle Journal of Advanced Engineering, which expresses the scope of the journal more precisely. Acta Polytechnica covers a wide spectrum of engineering topics in civil engineering, mechanical engineering, electrical engineering, nuclear sciences and physical engineering, architecture, transportation science, biomedical engineering and computer science and engineering. The scope of the journal is not limited to the realm of engineering. We also publish articles from the area of natural sciences, in particular physics and mathematics.

Acta Polytechnica is now being published in an enlarged format. Our aim is to be a high-quality multi-disciplinary journal publishing the results of basic research and also applied research. We place emphasis on the quality of all published papers. The journal should also serve as a bridge between basic research in natural sciences and applied research in all technical disciplines.

We invite researchers to submit high-quality original papers. The conditions of the submission process are explained in detail on: `http://ojs.cvut.cz/ojs/index.php/ap`. All papers will be reviewed, and accepted papers are published in English.

We hope that you will find our journal interesting, and that it will serve as a valuable source of scientific information.

Editorial Board

Contents

Acta Polytechnica **62**(4):409–417, 2022
`https://doi.org/10.14311/AP.2022.62.0409`

PERFORMANCE OF A HYDROMAGNETIC SQUEEZE FILM ON A ROUGH CIRCULAR STEP BEARING: A COMPARISION OF DIFFERENT POROUS STRUCTURES

Jatinkumar V. Adeshara[a], Hardik P. Patel[b,*], Gunamani B. Deheri[c], Rakesh M. Patel[d]

[a] *Vishwakarma Government Engineering College, Chandkheda, Ahmedabad - 382424 Gujarat State, India*
[b] *L. J. Institute of Engineering and Technology, Department of Humanity and Science, Ahmedabad, Gujarat State, India*
[c] *Sardar Patel University, Department of Mathematics, Vallabh Vidyanagar - 388 120 Gujarat State, India*
[d] *Gujarat Arts and Science College, Department of Mathematics, Ahmedabad - 380 006 Gujarat State, India*
[*] corresponding author: `hardikanny82@gmail.com`

Abstract.

This investigation deals with a comparative analysis of the impact of spongy structure based on the model of Kozeny-Carman and Irmay on a hydromagnetic squeeze film in a rough circular step bearing. Christensen and Tonder's stochastic averaging process has been utilized to determine the role of an arbitrary transverse surface irregularity. The distribution of the pressure in the bearing is obtained by solving the concerned generalised stochastically averaged equation of Reynolds' with appropriate boundary conditions. The outcomes show that increasing values of magnetization results in an augmented load. The impact of the surface irregularity (transverse) has been found to be adverse. In addition, the negative effect of the surface irregularity and porosity can be minimised by the positive impact of magnetization, at least in the case of the globular sphere model of Kozeny-Carman. Furthermore, the lower strength of the magnetic field results in an approximately similar performance for both these models. This study offers the possibility that the Kozeny-Carman model could be deployed in comparison with Irmay's model.

Keywords: Hydromagnetic fluid, squeeze film, circular step bearing, surface irregularity, spongy structure.

1. Introduction

The efficiency of bearings was substantially improved as compared to traditional lubricants. The magnetohydrodynamic squeeze film performance between curved annular plates was inspected by Lin. et al. [1]. Patel & Deheri [2] examined the influence of a magnetic fluid lubricant on a squeeze film in conical plates. It was found that the overall efficiency improved with this bearing system. Of course, the feature of the cone's semi-vertical angle was crucial in enhancing the performance. The approach adopted in the Patel & Deheri investigation [2] has been amended and improved by Vadher et al. [3]. Calculating the negative impact of the surface irregularity (transverse) between rough spongy conical plates of a magnetic-fluid-based squeeze film. They found that in the case of the negative skewed surface irregularity, the already-increased load increased even further.

Andharia & Deheri [4] examined the longitudinal effect of a surface irregularity between conical plates on the magnetic-fluid-dependent squeeze film. In relation to the surface irregularity (transverse), the squeeze film associated with the surface irregularity increased the load for a cylindrical squeeze film, Lin [5] developed a ferrofluid lubrication equation that takes into account convective fluid inertia forces for a circular disc application. Compared to the non-inertia non-ferrofluid case, a longer elapsed period was found. The product of a squeeze film based on magnetic fluid between rough (longitudinally) elliptical plates has already been considered by Andharia & Deheri [6]. It was noted that due to the combination of the squeeze film and the negative skewed surface irregularity, the load increased significantly due to the magnetisation. The Shliomis-model-based ferrofluid lubrication of a squeeze film was discussed by Patel & Deheri [7] for rotating rough (transversely) curved circular plates. Such a type of bearing structure allows a certain amount of load even though there is no flow of a typical lubricant. Very recently, Patel et al. [8]) investigated a squeeze film behaviour of different spongy structures on rough conical plates. The Kozeny-Carman model is preferred over the Irmay's model for spongy structure in the case of a surface irregularity (transverse). Hydromagnetic squeeze film in rough truncated conical plates, using the Kozeny-Carman-model-based spongy structure, was discussed by Adeshara et al. [9].

A new kind of bearing is introduced by Robert Goraj [10], where the thickness of the lubricant is also used as an electromagnetic system air gap. Here, under hydrodynamic, electromagnetic, and gravity stresses, a new

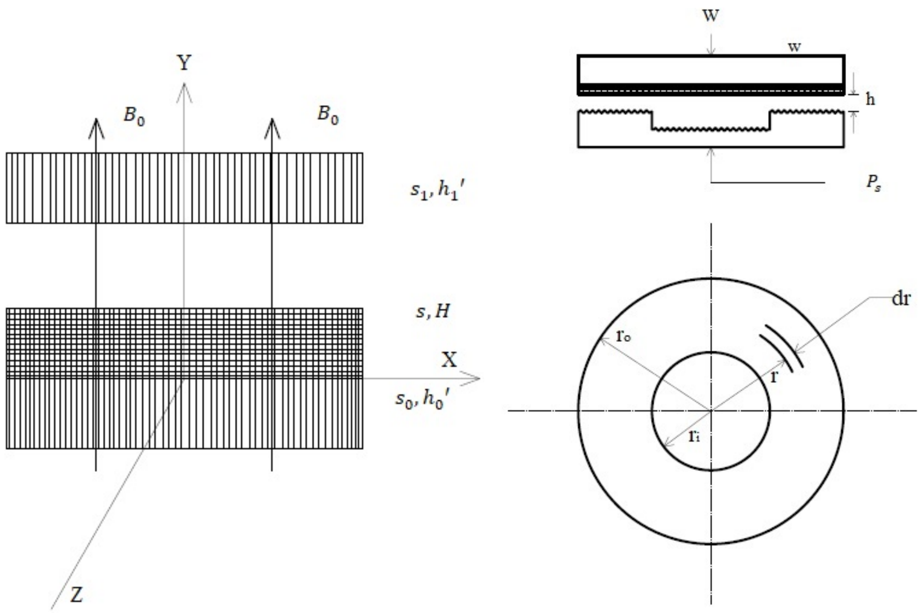

Figure 1. The bearing system design and specification are given.

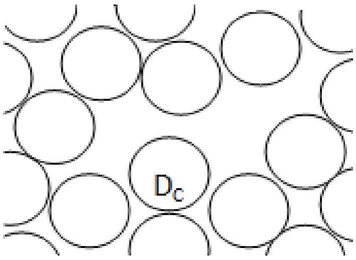

Figure 2. Configuration of spongy sheets given by Kozeny-Carman.

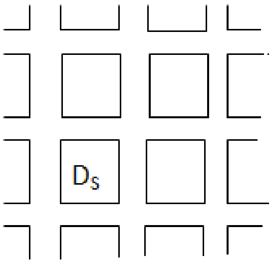

Figure 3. Configuration of spongy sheets provided by Irmay.

governing equation system defining steady loci of such an electromagnetically supported short hydrodynamic plain journal bearing is obtained and solved. Lu et al. [11] develops an analytic model to predict the static properties of a new hydrodynamic–rolling hybrid bearing. The findings demonstrate that the hydrodynamic–rolling hybrid bearing working states are split into two separate phases by a transition speed at which the hydrodynamics and contact models are separated. The impact of surface roughness and micropolar lubricant between two elliptical plates under the application of an external transverse magnetic field was analysed by Halambi et al. [12]. Younes et al. [13] have presented several strategies for increasing the thermal conductivity of these fluids by suspending nano/micro-sized particle materials in them. Patel and Deheri [14] discussed the influence of viscosity variation on ferrofluid-based long bearing. In this article, it is observed that the increased load carrying capacity, due to the magnetization, is not significantly affected by viscosity variation.

In this article, it has been sought to study and analyse the performance of hydromagnetic squeeze film on a rough circular step bearing with inclusion of two different porous structures: Kozeny-Carman and Irmay's model. Furthermore, the effect of transverse roughness on the bearing's performance is also discussed.

2. Analysis

The lower plate with a porous facing is assumed to be fixed while the upper plate moves along its normal towards the lower plate. The plates are considered electrically conductive and the clearance space between them is filled by an electrically conducting lubricant. A uniform transverse magnetic field is applied between the plates. The flow in the porous medium obeys the modified form of Darcy's law.

As shown in Figure 1, here, bearings are not in direct contact and the load is applied on the bearings. The load w is carried within the pocket and surface by the fluid. The fluid flows in a radial direction. Following the analyses of Majumdar [15], and Patel, Deheri & Vadher [8], one finds that the Reynolds-type equation for the pressure induced flow in a circular-step bearing is

$$Q = -\frac{2\pi r \dfrac{\mathrm{d}p}{\mathrm{d}r}\left[\dfrac{2A}{M^3}\left[\dfrac{M}{2} - \tanh\dfrac{M}{2}\right] + \dfrac{\psi l_1 A}{c^2}\right]\left[\dfrac{\phi_0 + \phi_1 + 1}{\phi_0 + \phi_1 + \left(\tanh\frac{M}{2}\right) / \left(\frac{M}{2}\right)}\right]}{12\mu}, \tag{1}$$

where

$$A = h^3 + 3h^2\alpha + 3h\left(\alpha^2 + \sigma^2\right) + \varepsilon + 3\sigma^2\alpha + \alpha^3. \tag{2}$$

2.1. Case – I (A globular sphere model as displayed in Figure 2)

This model includes the globular sphere to fill in the spongy content of particles. The mean particle size is D_c. The permeability of the spongy region was found to be

$$\psi = \frac{D_c^2 e_1^3}{180\left(1 - e_1\right)^2}, \tag{3}$$

where e_1 is the porosity. Integrate the above equation (1) with respect to the boundary condition. Using Reynolds' boundary condition

$$\begin{aligned} r &= r_0, \quad p = 0, \\ r &= r_i, \quad p = p_s. \end{aligned} \tag{4}$$

The leading film pressure equation p is given by the

$$p = p_s \frac{\ln\left(\frac{r}{r_o}\right)}{\ln\left(\frac{r_i}{r_o}\right)}, \tag{5}$$

where in

$$p_s = \frac{6\ln\left(\dfrac{r_o}{r_i}\right)}{\pi\left[\dfrac{2A}{M^3}\left[\dfrac{M}{2} - \tanh\dfrac{M}{2}\right] + \dfrac{D_c^2 e_1^3 l_1 A}{180\left(1 - e_1\right)^2 c^2}\right]\left[\dfrac{\phi_0 + \phi_1 + 1}{\phi_0 + \phi_1 + \left(\tanh\frac{M}{2}\right) / \left(\frac{M}{2}\right)}\right]}. \tag{6}$$

Here non-dimensional equation

$$P_s^* = \frac{6\ln\left(\dfrac{1}{k}\right)}{\pi\left[\dfrac{2B}{M^3}\left[\dfrac{M}{2} - \tanh\dfrac{M}{2}\right] + \dfrac{\overline{\psi} B e_1^3}{15\left(1 - e_1\right)^2 c^2}\right]\left[\dfrac{\phi_0 + \phi_1 + 1}{\phi_0 + \phi_1 + \left(\tanh\frac{M}{2}\right) / \left(\frac{M}{2}\right)}\right]}. \tag{7}$$

Introducing the non-dimensional quantities

$$\begin{gathered} B = 1 + 3\alpha^* + 3\left(\alpha^{*2} + \sigma^{*2}\right) + \varepsilon^* + 3\sigma^{*2}\alpha^* + \alpha^{*3}, \\ \alpha^* = \left(\frac{\alpha}{h}\right), \quad \sigma^* = \left(\frac{\sigma}{h}\right), \quad \varepsilon^* = \left(\frac{\varepsilon}{h^3}\right), \quad k = \left(\frac{r_i}{r_o}\right), \quad \overline{\psi} = \frac{D_c^2 l_1}{h^3}. \end{gathered} \tag{8}$$

By integrating the pressure that takes the dimensionless form, the load w is computed.

$$W = \frac{P_s^*\left(1 - k^2\right)}{2\ln\left(\frac{1}{k}\right)}. \tag{9}$$

2.2. Case – II (model with capillary fissures as revealed in Figure 3)

This model deals with three sets of mutually orthogonal fissures (mean solid size D_s). Irmay [16] assumed no loss of hydraulic gradient at the junction and derived the expression for the spongy structure parameter as

$$\psi = \frac{(1 - m)^{2/3} D_s^2}{12m}, \tag{10}$$

where $m = 1 - e_1$, e_1 being the porosity. The governing equation for the film pressure p is given by

$$p = p_s \frac{\ln\left(\frac{r}{r_o}\right)}{\ln\left(\frac{r_i}{r_o}\right)}, \tag{11}$$

$$p_s = \frac{6\ln\left(\dfrac{r_o}{r_i}\right)}{\pi\left[\dfrac{2A}{M^3}\left[\dfrac{M}{2} - \tanh\dfrac{M}{2}\right] + \dfrac{(1-m)^{2/3}D_s^2 l_1 A}{12mc^2}\right]\left[\dfrac{\phi_0+\phi_1+1}{\phi_0+\phi_1+\left(\tanh\frac{M}{2}\right)/\left(\frac{M}{2}\right)}\right]}. \tag{12}$$

Here, non-dimensional equation

$$P_s^* = \frac{6\ln\left(\dfrac{1}{k}\right)}{\pi\left[\dfrac{2B}{M^3}\left[\dfrac{M}{2} - \tanh\dfrac{M}{2}\right] + \dfrac{\overline{\psi}B(1-m)^{2/3}}{mc^2}\right]\left[\dfrac{\phi_0+\phi_1+1}{\phi_0+\phi_1+\left(\tanh\frac{M}{2}\right)/\left(\frac{M}{2}\right)}\right]}. \tag{13}$$

Introducing the non-dimensional quantities

$$B = 1 + 3\alpha^* + 3\left(\alpha^{*2} + \sigma^{*2}\right) + \varepsilon^* + 3\sigma^{*2}\alpha^* + \alpha^{*3}, \tag{14}$$

where

$$\overline{\psi} = \frac{D_s^2 l_1}{h^3}.$$

The load w is calculated by integrating the pressure, which takes the dimensionless form

$$W = \frac{P_s^*\left(1-k^2\right)}{2\ln\left(\frac{1}{k}\right)}. \tag{15}$$

3. Results and discussions

In the absence of porous structures, the current study reduces to the deliberation of hydromagnetic squeeze film in rough circular step bearing. Further, for smooth bearing surfaces, this analysis comes down to the discussion of circular step bearing (Majumdar [15]), when there is no magnetization. However, because of porous structures, there is an additional degree of freedom from a bearing design point of view. Equations (7) and (13) describe the dimensionless pressure profile, while equations (9) and (15) govern the non-dimensional load. These expressions clearly suggest that the load $W \propto P_s^*$ and

$$p_s = \frac{Q}{\pi\left[\dfrac{2A}{M^3}\left[\dfrac{M}{2} - \tanh\dfrac{M}{2}\right] + \dfrac{\psi l_1 A}{c^2}\right]\left[\dfrac{\phi_0+\phi_1+l}{\phi_0+\phi_1+\left(\tanh\frac{M}{2}\right)/\left(\frac{M}{2}\right)}\right]}.$$

This means that the load increases with a constant flow rate as the stochastically averaged squeeze film decreases in thickness. The bearing is thus self-compensating, provided that the flow rate is assumed to be constant. Equations (7) and (13), (9) and (15) indicate that the effect of conductivity parameters on the pressure distribution and load is determined by

$$\frac{\phi_0+\phi_1+\left(\tanh\dfrac{M}{2}\right)/\left(\dfrac{M}{2}\right)}{\phi_0+\phi_1+1},$$

which turns to

$$\frac{\phi_0+\phi_1}{\phi_0+\phi_1+1},$$

for big values of M, because as $\tanh M \cong 1$ and $(2/M) \cong 0$. Furthermore, it is observed that the pressure and load rise with growths in $\phi_0 + \phi_1$ because both the functions are growing functions of $\phi_0 + \phi_1$.

Figures 4, 5, 8, 9, 12, 13, 16, 17, 20, 21, 24, 26 deal with the pattern of the load with respect to different parameters for Kozeny-Carman's globular sphere model, Figures 6, 7, 10, 11, 14, 15, 18, 19, 22, 23, 25, 27 deal with the variance of the load in relation to Irmay's model of capillary fissures.

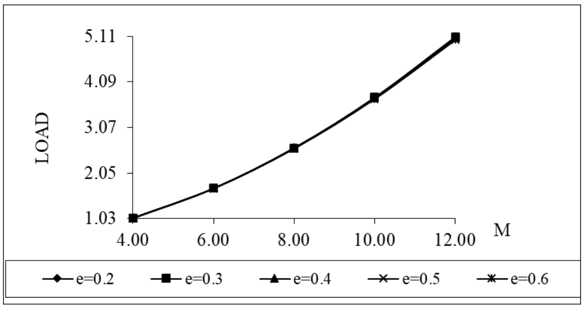

Figure 4. Profile of load with M & e.

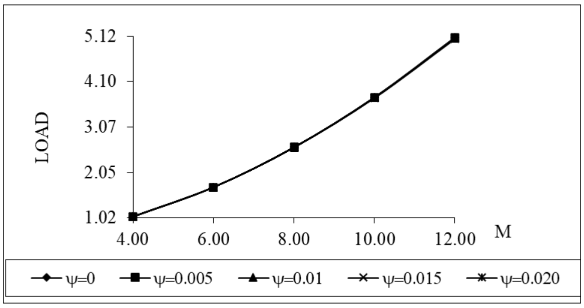

Figure 5. Data of load with M & ψ.

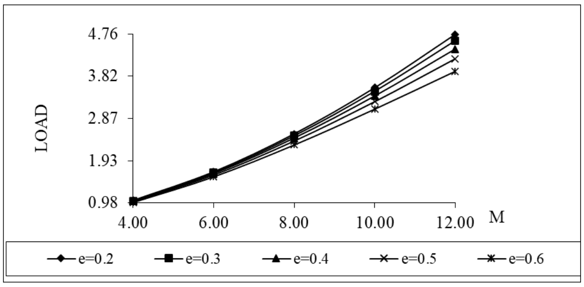

Figure 6. Data of load with M & e.

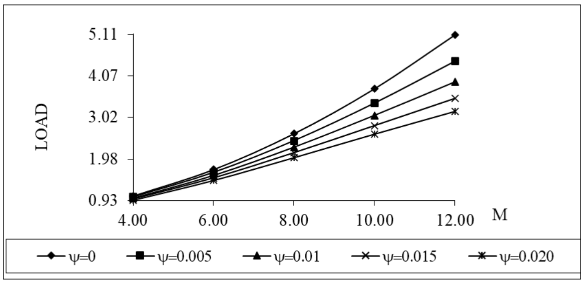

Figure 7. Change of load with M & ψ.

Increased magnetization parameters will then contribute to an increased load as can be seen in Figures 4 and 5 and Figures 6 and 7, it can be noted that the rate of the increase in the load is comparatively greater in Kozen-Carman's globular sphere model. However, in the case of the globular sphere model, the impact of spongy structure parameters and porosity on the variation of load with regard to magnetization is negligible to some degree. For both models, the load increases sharply.

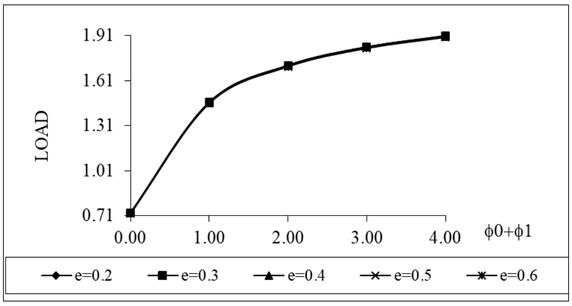

Figure 8. Change of load with $\phi_0 + \phi_1$ & e.

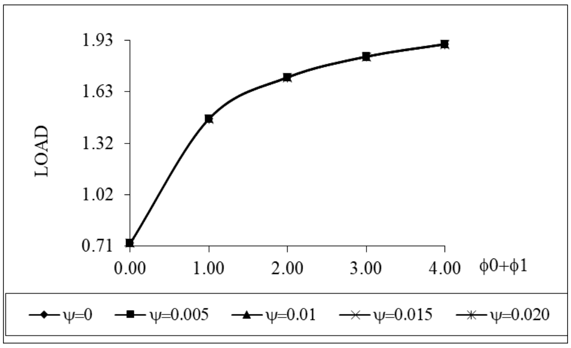

Figure 9. Profile of load with $\phi_0 + \phi_1$ & ψ.

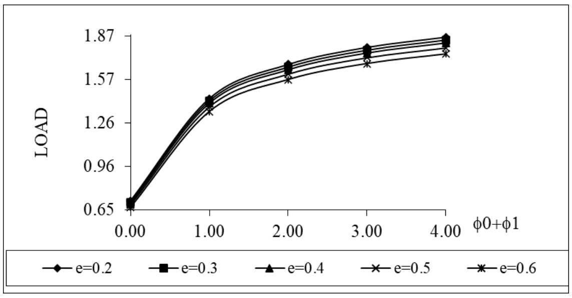

Figure 10. Data of load with $\phi_0 + \phi_1$ & e.

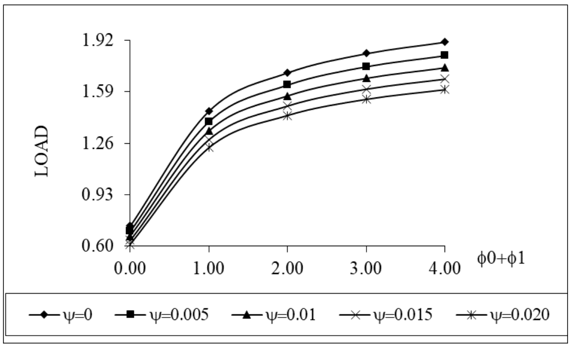

Figure 11. Change of load with $\phi_0 + \phi_1$ & ψ.

The effect of $\phi_0 + \phi_1$ on the distribution of the load with respect to the Kozeny-Carman model is shown in Figures 8 and 9, while the profile of the load for the Irmay model is given in Figures 10 and 11. The rate of the increase in the load is comparatively higher in Kozeny-Carman's globular sphere model as compared to Irmay's capillary fissures model.

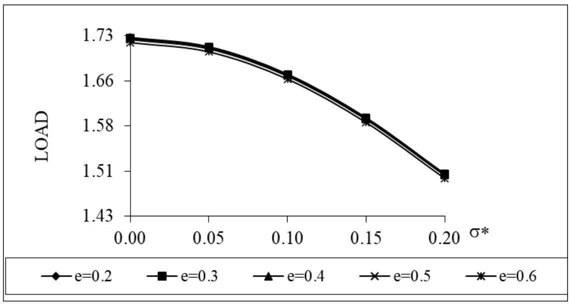

Figure 12. Variation of load with σ^* & e.

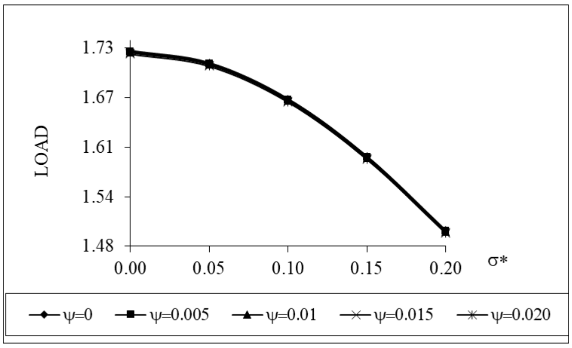

Figure 13. Data of load with σ^* & ψ.

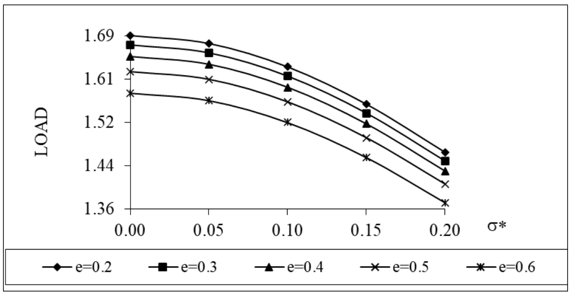

Figure 14. Data of load with σ^* & e.

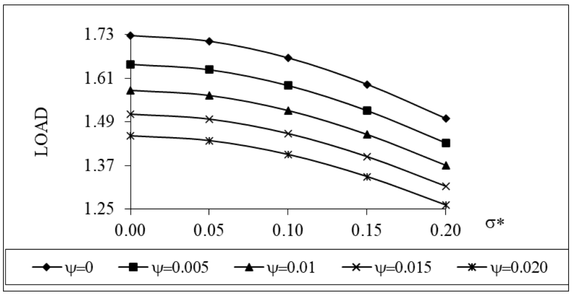

Figure 15. Profile of load with σ^* & ψ.

Figures 12 and 13 provide the squeeze film effect on the distribution of the load with respect to the Kozeny-Carman's model and Irmay model in Figures 14 and 15. It can be seen that an increase in the values of squeeze film results in an increased load and, consequently, adversely affects the squeeze film performance. As can be seen from Figures 12 and 13, for the Kozeny-Carman model, the effect of the spongy structure and porosity on the variance of the load carrying capacity with regard to the squeeze film is marginal, but in the Irmay model, it is negligible.

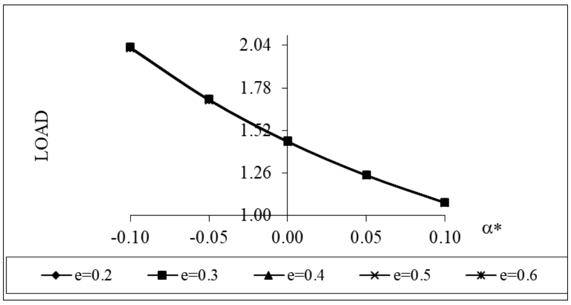

Figure 16. Change of load with α^* & e.

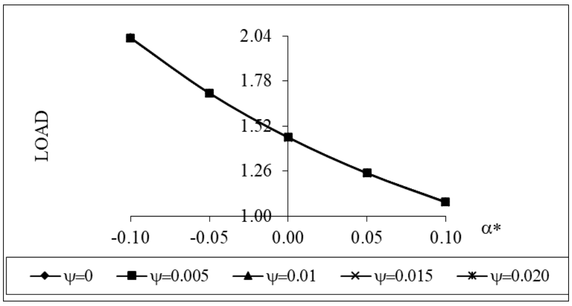

Figure 17. Variation of load with α^* & ψ.

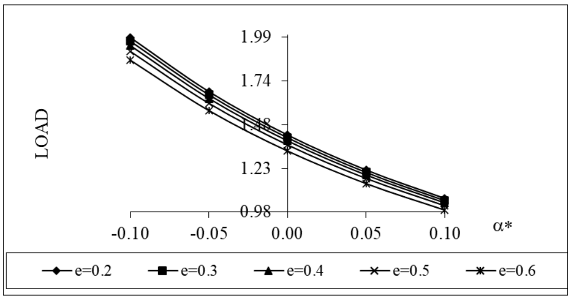

Figure 18. Trend of load with α^* & e.

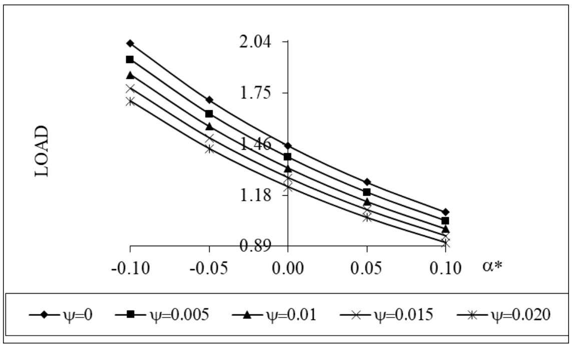

Figure 19. Profile of load with α^* & ψ.

It is found that the load bearing capacity decreases due to the positive variance. The opposite of this trend is visible in the case of the negative variance for both models (Kozeny-Carman and Irmay). It is important to note that the influence of the spongy structure parameter on the variation of the load remains negligible for the Kozeny-Carman model with respect to variance. (Figures 16 and 17) and Irmay's model (Figures 18 and 19).

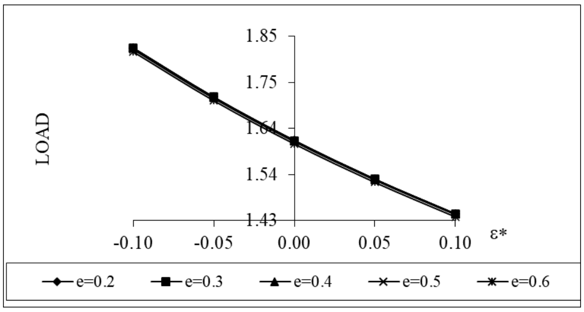

Figure 20. Data of load with ε^* & e.

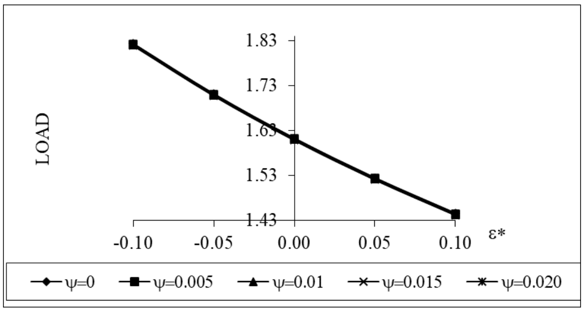

Figure 21. Change of load with ε^* & ψ.

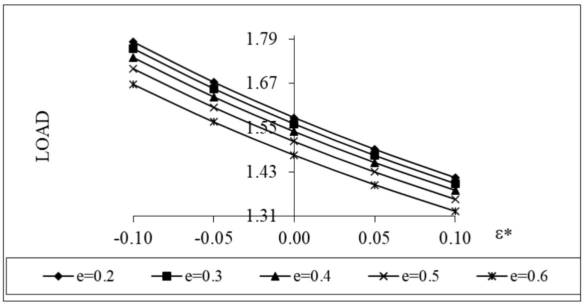

Figure 22. Variation of load with ε^* & e.

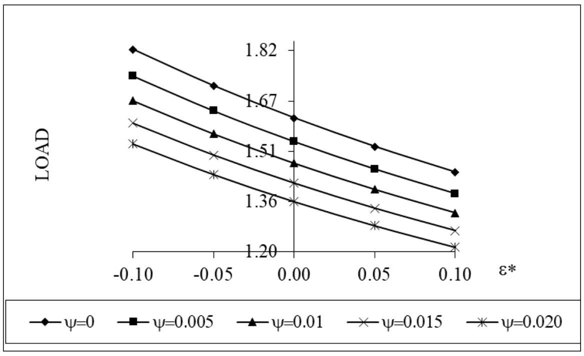

Figure 23. Profile of load with ε^* & ψ.

The effect of skewness for the Kozeny-Carman model and Irmay's model is presented in Figures 20 and 21 and Figures 22 and 23, respectively. The increased load due to variance (-ve) gets further increased as a result of the negatively skewed surface irregularity. Here, the effect of the spongy structure parameter and porosity is also negligible in the case of Kozeny-Carman model, while a better performance can be seen in the case of Irmay's model.

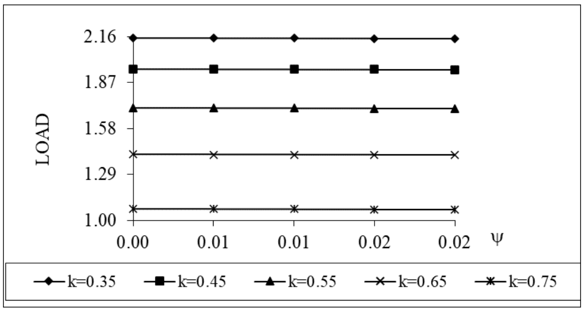

Figure 24. Profile of load with ψ & k.

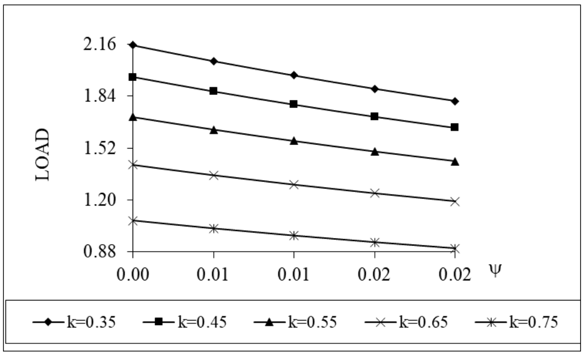

Figure 25. Trend of load with ψ & k.

The combined effect of the spongy structure parameter and radii ratio (k) appears to be adverse, which can be seen from Figures 24 and 25. However, at the outset, the decrease in load is more profound in the case of Irmay's model.

The effect of porosity and redii ratio is presented in Figure 26 for Kozeny-Carman model and Figure 27 for Irmay's model. For Irmay's model, only an increase can be seen, however, that is not the case for Kozeny-Carman model.

A comparison of both models is presented. From Table 1, one can see that Kozeny-Carman model provides a better performance as compared to Irmay's model with regards to the transverse roughness.

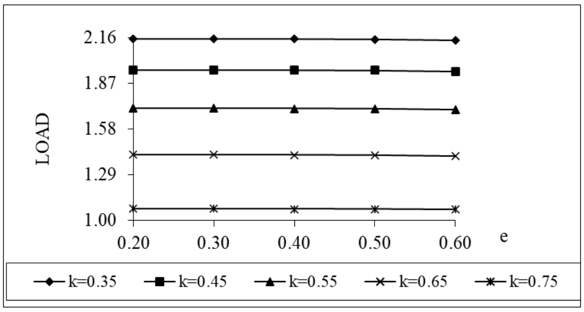

Figure 26. Variation of load with e & k.

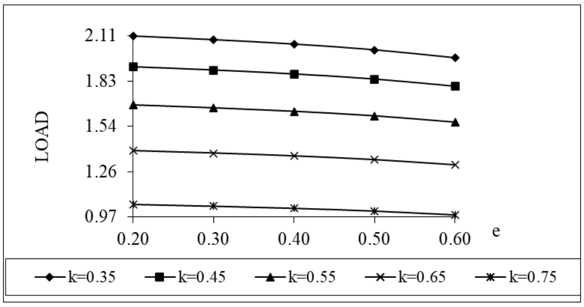

Figure 27. Change of load with e & k.

		Kozeny-Carman's globular sphere model		Irmay's model of capillary fissures	
Sr. No	Graph	Minimum	Maximum	Minimum	Maximum
1	$M \to e$	1.04178748	5.10051255	0.99169035	4.75745642
2	$M \to \psi$	1.04311200	5.10122332	0.94204858	5.10122332
3	$\phi_0 + \phi_1 \to e$	0.72690126	1.90743812	0.66815659	1.86550029
4	$\phi_0 + \phi_1 \to \psi$	0.72851122	1.90752098	0.61379908	1.90752098
5	$\sigma^* \to e$	1.49304632	1.72660919	1.37238548	1.68864716
6	$\sigma^* \to \psi$	1.49635317	1.72668420	1.26073582	1.72668420
7	$\alpha^* \to e$	1.07736948	2.03056534	0.99030164	1.98592038
8	$\alpha^* \to \psi$	1.07975567	2.03065355	0.90973620	2.03065355
9	$\varepsilon^* \to e$	1.43886631	1.82372390	1.32258403	1.78362666
10	$\varepsilon^* \to \psi$	1.44205315	1.82380313	1.21498594	1.82380313
11	$\psi \to k$	1.07109072	2.15361105	0.90243565	2.15361105
12	$e \to k$	1.06872368	2.15351750	0.98235456	2.10616926

Table 1. A comparison of both models.

4. Conclusion

This analysis demonstrates that the Kozeny-Carman model is a better choice for this type of bearing design. Furthermore, this research shows that the surface irregularity aspect must be carefully considered while designing the bearing systems, even if the required magnetic strength is employed. This can play a vital role in improving the overall performance in the case of Irmay's model. In addition, in the absence of flow, the bearing system supports some load for these two models, which never occurs for traditional lubricants and this load is comparatively higher in the case of Kozeny-Carman model.

Acknowledgements

The authors would like to thank the reviewers for their valuable remarks and suggestions for the overall improvement of the presentation and organization of the manuscript.

List of symbols

R	Radial coordinate
r_o	Outer radius
r_i	Inner radius
K	$= \frac{r_i}{r_o}$ – Radii ratio
H	Film thickness of lubricant
S	Lubricant's electrical conductivity
μ	Lubricant's viscosity
B_o	Uniform transverse magnetic field applied between the plates
M	$= B_0 h \left(\frac{s}{\mu}\right)^{1/2}$ – Hartmann Number
p_s	Supply Pressure
Q	Flow rate
P_s^*	Dimensionless supply pressure

P	Lubricant pressure
P^*	Non-dimensional pressure
W	Dimensionless L.C.C
h_0	Lower plate's surface width
h_1	Upper plate's surface width
s_0	Lower surface's electrical conductivity
s_1	Upper surface's electrical conductivity
$\phi_0(h)$	$= \frac{s_0 h'_0}{sh}$ – Electrical permeability of lower surface
$\phi_1(h)$	$= \frac{s_1 h'_1}{sh}$ – Electrical permeability of upper surface
σ^*	Non-dimensional S.F.
α^*	Dimensionless variance
ε^*	Non dimensional skewness
ψ	Spongy structure of the spongy region
e_1	Porosity
l_1	Thickness of spongy facing

REFERENCES

[1] J.-R. Lin, R.-F. Lu, W.-H. Liao. Analysis of magneto-hydrodynamic squeeze film characteristics between curved annular plates. *Industrial Lubrication and Tribology* **56**(5):300–305, 2004. `https://doi.org/10.1108/00368790410550714`.

[2] R. M. Patel, G. Deheri. Magnetic fluid based squeeze film between porous conical plates. *Industrial Lubrication and Tribology* **59**(3):143–147, 2007. `https://doi.org/10.1108/00368790710746110`.

[3] P. Vadher, G. Deheri, R. Patel. Performance of hydromagnetic squeeze films between conducting porous rough conical plates. *Meccanica* **45**(6):767–783, 2010. `https://doi.org/10.1007/s11012-010-9279-y`.

[4] P. I. Andharia, G. Deheri. Longitudinal roughness effect on magnetic fluid-based squeeze film between conical plates. *Industrial Lubrication and Tribology* **62**(5):285–291, 2010. `https://doi.org/10.1108/00368791011064446`.

[5] J.-R. Lin. Derivation of ferrofluid lubrication equation of cylindrical squeeze films with convective fluid inertia forces and application to circular disks. *Tribology International* **49**:110–115, 2012. `https://doi.org/10.1016/j.triboint.2011.11.006`.

[6] P. Andharia, G. Deheri. Performance of magnetic-fluid-based squeeze film between longitudinally rough elliptical plates. *International Scholarly Research Notices* **2013**:482604, 2013. `https://doi.org/10.5402/2013/482604`.

[7] J. R. Patel, G. Deheri. Shliomis model based magnetic fluid lubrication of a squeeze film in rotating rough curved circular plates. *Caribbean Journal of Sciences and Technology (CJST)* **1**:138–150, 2013.

[8] R. M. Patel, G. Deheri, P. Vahder. Hydromagnetic rough porous circular step bearing. *Eastern Academic Journal* **3**:71–87, 2015.

[9] J. Adeshara, H. Patel, G. Deheri. Theoretical study of hydromagnetic S.F. rough truncated conical plates with Kozeny-Carman model based spongy structure. *Proceeding on Engineering sciences* **2**(4):389–400, 2020. `https://doi.org/10.24874/PES0204.006`.

[10] R. Goraj. Theoretical study on a novel electromagnetically supported hydrodynamic bearing under static loads. *Tribology International* **119**:775–785, 2018. `https://doi.org/10.1016/j.triboint.2017.09.021`.

[11] D. Lu, W. Zhao, B. Lu, J. Zhang. Static characteristics of a new hydrodynamic–rolling hybrid bearing. *Tribology International* **48**:87–92, 2012. `https://doi.org/10.1016/j.triboint.2011.11.010`.

[12] B. Halambi, B. N. Hanumagowda. Micropolar squeeze film lubrication analysis between rough porous elliptical plates and surface roughness effects under the MHD. *Ilkogretim Online* **20**(4):307–319, 2021. `https://doi.org/10.17051/ilkonline.2021.04.33`.

[13] Y. Menni, A. J. Chamkha, A. Azzi. Nanofluid flow in complex geometries – A review. *Journal of Nanofluids* **8**(5):893–916, 2019. `https://doi.org/10.1166/jon.2019.1663`.

[14] J. Patel, G. Deheri. Influence of viscosity variation on ferrofluid based long bearing. *Reports in Mechanical Engineering* **3**(1):37–45, 2022. `https://doi.org/10.31181/rme200103037j`.

[15] B. C. Majumdar. *Introduction to tribology of bearings.* AH Wheeler & Company, India, 1986.

[16] S. Irmay. Flow of liquid through cracked media. *Bulletin of the Research Council of Israel* **5**(1):84, 1955.

Acta Polytechnica **62**(4):418–426, 2022
`https://doi.org/10.14311/AP.2022.62.0418`

DISINFECTION PERFORMANCE OF AN ULTRAVIOLET LAMP: A CFD INVESTIGATION

Cuong Mai Bui, Nguyen Duy Minh Phan*, Ngo Quoc Huy Tran,
Le Anh Doan, Quang Truong Vo, Duy Chung Tran,
Thi Thanh Vi Nguyen, Duc Long Nguyen, Van Sanh Huynh,
Tran Anh Ngoc Ho

The University of Danang - University of Technology and Education, 48 Cao Thang, Danang 550000, Viet Nam

* corresponding author: `pndminh@ute.udn.vn`

Abstract.

Ultraviolet(UV)-based devices have shown their effectiveness on various germicidal purposes. To serve their design optimisation, the disinfection effectiveness of a vertically cylindrical UV lamp, whose wattage ranges from $P = 30$–$100\,\mathrm{W}$, is numerically investigated in this work. The UV radiation is solved by the Finite Volume Method together with the Discrete Ordinates model. Various results for the UV intensity and its bactericidal effects against several popular virus types, i.e., *Corona-SARS*, *Herpes* (type 2), and *HIV*, are reported and analysed in detail. Results show that the UV irradiance is greatly dependent on the lamp power. Additionally, it is indicated that the higher the lamp wattage employed, the larger the bactericidal rate is observed, resulting in the greater effectiveness of the UV disinfection process. Nevertheless, the wattage of $P \leq 100\,\mathrm{W}$ is determined to be insufficient for an effective disinfection performance in a whole room; higher values of power must hence be considered in case intensive sterilization is required. Furthermore, the germicidal effect gets reduced with the viruses less sensitive to UV rays, e.g, the bactericidal rate against the *HIV* virus is only $\sim$8.98 % at the surrounding walls.

Keywords: UV-C, disinfection, discrete ordinates, *Corona-SARS*, CFD.

1. Introduction

The worldwide outbreak of Coronavirus (COVID-19), which terribly affects human health and the world economy, has drawn a great awareness of infectious diseases' danger. Numerous intensive studies have been carried out to improve the disinfection efficiency in hospitals where many patients with serious underlying medical conditions stay [1–5]. In order to prevent the virus spread, various controlling techniques, such as air filtration, heat sterilization, chemical disinfectants, and Ultraviolet Germicidal Irradiation (UVGI), have been employed [6]. Amongst them, the last one uses the spectral sensitivity to *Deoxyribonucleic Acid* (DNA) of Ultraviolet (UV) light of wavelength ranging between 100–280 nm [7]. In detail, under the so-called UVC conditions, the photochemical changes in nucleic acids would deactivate the reproduction of microorganisms [8]. To mention some advantages of this approach, in addition to dealing with virus growth efficiently within a short time, the UVGI approach could save a large amount of operating and maintenance costs. Furthermore, with the no-touch mechanism, UVGI is supposed to ensure a better safety for human activities and the environment during the disinfection process as compared to chemical treatments [9].

Recently, many UV-C-based devices and autonomous robots are developed for disinfection purposes in hospitals and/or medical centers [10–13]. To optimise their design, factors directly affecting the germ-killing efficiency, e.g., UV dose and intensity, should be taken into account. In recent years, the advanced development of the Computational Fluid Dynamics (CFD) approach allows to better predict the irradiation distribution and physical phenomenon occurring during the UV germicidal process. In fact, numerical simulation was first employed to investigate the water treatment performance of UV reactors. Pan and Orava [14] indicated that CFD integrated with fluence modelling approach could be an important tool to determine flow and radiation field characteristics. Ho [15] numerically investigated the influences of wall reflection and refraction at separating material interfaces (e.g., quartz sleeve or lamp surface) on the water disinfection inside a chamber; the Discrete Ordinates (DO) method was adopted to solve the radiation transfer equation. As illustrated, simulation results for the radiation intensity could be overestimated around the lamp but underestimated further away from it once the reflection and refraction were not considered at the quart sleeve. Additionally, Sobhani and Shokouhmand [16] investigated the influences of the lamp power, the flow rate, and the water temperature using both experimental and numerical approaches. It was claimed that the lower the flow rate and/or the greater the lamp power, the higher the UV reactors' efficiency was seen. Recently, the

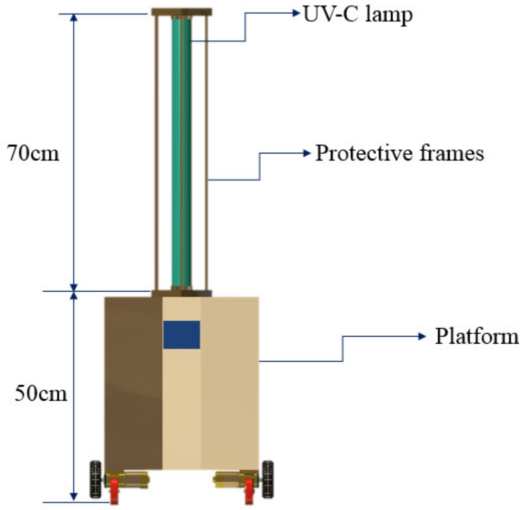

Figure 1. Example of a simple UV disinfection device.

CFD approach has been widely utilised to predict air disinfection performance. Capetillo et al. [17] and then Atci et al. [18] studied the UV germicidal efficiency in heating, ventilation, and air conditioning (HVAC) systems. Different arrangements of single and/or multiple lamps were assessed to determine the optimal in-duct configurations. Various results for the airflow field, the UV irradiation distribution, and UV dose were reported and analysed in detail therein. Moreover, a Lagrangian approach was realised for modelling the UV bactericidal influences at Reynolds numbers of $\mathrm{Re} = 4.11 \times 10^4 - 8.22 \times 10^4$ [19]. It was noted that the results obtained were well in line with experimental data; this technique showed a better prediction over an Eulerian one. Results also indicated that the disinfection rate for *P. alcaligenes* and *E. coli* viruses was 100 %. For the *Coronavirus*, Buchan et al. [20] carried out a series of simulations for a populated room with a UV-C device. It was indicated that the far UV-C lighting can increase the bactericidal rate up to 80 % rather than using a conventional ventilation system.

To our best knowledge, the research on the UV disinfection performance in hospitals is still very scarce [21]. In this study, we are aiming at evaluating the coverage region and then the bactericidal effects of a vertical UV lamp using a numerical approach. It is noted that this setting is equivalent to the simplest design of a disinfection device (see Figure 1). As a preliminary study, the influences of airflow and temperature variation are considered to be neglected.

The rest of this paper is organized as follows: theory background including governing equations and numerical approach is provided in Section 2; Section 3 presents and analyses the simulation results; some concluding remarks and recommendations for future works are revealed in Section 4.

2. THEORY BACKGROUND

2.1. MODELLING OF UV IRRADIANCE

The UV irradiance is governed by the radiative transfer equation (RTE) as follows:

$$\frac{dI(\mathbf{r},\mathbf{s})}{ds} + (\alpha + \sigma_s) I(\mathbf{r},\mathbf{s}) = \alpha n^2 \frac{\sigma T^4}{\pi} + \frac{\sigma_s}{4\pi} \int_0^{4\pi} I(\mathbf{r},\mathbf{s}') \Phi(\mathbf{s}\cdot\mathbf{s}') d\Omega' . \quad (1)$$

Here, I is the radiation intensity; $\mathbf{r}$, $\mathbf{s}$ and $\mathbf{s}'$ are, in turn, the position, direction, and the scattering direction vectors; respectively, α and σ_s stand for the absorption and scattering coefficients, respectively; n is the refractive index; $\sigma = 5.669 \times 10^{-8}$ W/m^{2}K^4 is the Stefan-Boltzmann constant; T is the local temperature; Φ is the phase function; Ω' is the solid angle.

To numerically solve Equation 1 with a finite discretization of solid angles, the DO radiation model for non-gray radiation is utilised as [15, 22]:

$$\nabla \cdot (I_\lambda(\mathbf{r},\mathbf{s})\mathbf{s}') + (\alpha_\lambda + \sigma_s) I_\lambda(\mathbf{r},\mathbf{s}) = \alpha_\lambda n^2 I_{b\lambda} + \frac{\sigma_s}{4\pi} \int_0^{4\pi} I(\mathbf{r},\mathbf{s}') \Phi(\mathbf{s}\cdot\mathbf{s}') d\Omega' , \quad (2)$$

with I_λ being the spectral intensity, $I_{b\lambda}$ the black body intensity, and α_λ the spectral absorption coefficient.

The correlation between the lamp wattage, P, and the initial intensity, I_0, applied on the UV lamp is expressed as [8]:

$$I_0 = \frac{P}{2\pi r l} , \quad (3)$$

with r and l being the radius and length of the UV lamp, respectively.

2.2. BACTERICIDAL RATE

The disinfection performance is assessed by the bactericidal rate, b, as [23]:

$$b = (1 - s_v) \times 100\,\% = (1 - e^{-kIt}) \times 100\,\% . \quad (4)$$

Here, s_v is the survival rate and t is the exposure duration. Moreover, k is the standard rate constant representing the microorganism susceptibility; the larger the k, the higher the virus sensitivity to the UV rays, and the greater disinfection effectivity [8]. In this work, we focus on three different virus types, whose k vary in a relatively wide range, as follows

- The *Corona-SARS* ($k = 0.1106\,\mathrm{m^2/J}$) which was responsible for the SARS outbreak in 2003,
- The *Herpes* (type 2) ($k = 0.06569\,\mathrm{m^2/J}$) which causes itching or blisters on human skin , and
- The *HIV* ($k = 0.00822\,\mathrm{m^2/J}$) which severely damages the immune system of a human body.

More values of k can be referred in [8].

Mesh	**Number of elements**	$\mathbf{I_A}$ **[W/m²]**	$\mathbf{I_B}$ **[W/m²]**	**Running Time [h]**
M1	714,150	9.21	2.42	3
M2	1,039,332	9.38	2.33	4.2
M3	1,504,393	9.84	2.28	5
M4	2,196,471	9.86	2.28	8.5

TABLE 1. Results for the UV intensity at points A and B with various mesh resolutions.

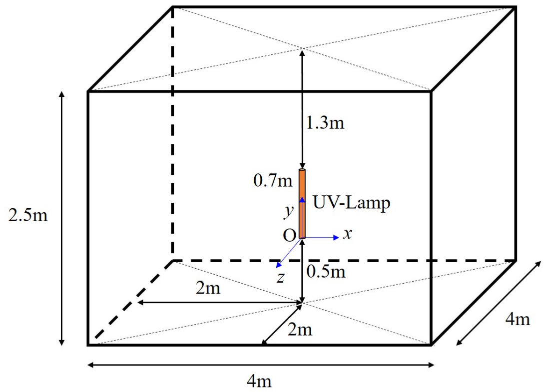

FIGURE 2. Computational geometry.

2.3. SIMULATION STRATEGY

2.3.1. COMPUTATIONAL GEOMETRY AND MESH

A three-dimensional (3D) computational domain mimicking an operating room is built as in Figure 2. The room is 4 m in length, 4 m in width, and 2.5 m in height; the UV lamp is positioned centered and 0.5 m away from the floor. The lamp is of a cylindrical shape; its diameter and length are 0.05 m and 0.7 m, as introduced in [24]. For boundary conditions, we apply a semi-transparent condition for the lamp's surface and an opaque condition for all the surrounding walls. A detailed explanation for these setups can be found in Ho [15].

To handle the calculations, an unstructured tetrahedral mesh with a high resolution near the lamp is generated. Moreover, at least five prisms are created around the lamp's surface to improve the accuracy and stability of the problem (see Figure 3). It is worth noticing that a mesh convergence study has been carried out. A comparison in the boundary of $I = 100\,\mathrm{W/m^2}$ produced by a 100 W-lamp among four mesh resolutions, i.e., M1 (∼714 K elements), M2 (∼1.039 M elements), M3 (∼1.504 M elements), and M4 (∼2.196M elements), is illustrated in Figure 4. It is evident that the deviation becomes negligibly insignificant with the refinement greater than 1.504M elements. In addition, Table 1 reveals the results for the UV intensity at points A and B, which are defined in Figure 5. Mesh M3 is found to be the most optimal since it provides nearly the same values as M4, but is much more computationally efficient. It is, therefore, reasonable to adopt M3 for all simulations. Numerical calculations are conducted with the Finite Volume Method (FVM) in Ansys Fluent v14.5.

Pixelation	$\mathbf{I_A}$ **[W/m²]**	$\mathbf{I_B}$ **[W/m²]**
1 × 1	9.83	2.28
3 × 3	9.84	2.28
5 × 5	9.84	2.28

TABLE 2. Variation in results for intensity at points A and B produced by a 100 W-lamp with different pixel resolutions.

2.3.2. MODELLING PARAMETERS

The parameters characterising angular discretization in the DO model are determined in this part. They include the pixelations (i.e., theta and phi pixels) and the divisions (i.e., theta and phi divisions). The former defines pixel refinements for an overhanging control volume; and the latter controls the angle quantity employed to discrete each octant [22].

Figure 6 compares the irradiation field obtained by different values of pixels. As can be seen, a non-smooth contour on the lamp is found with the pixelations of 1 × 1; however, the smoothness is improved with a resolution larger than 3 × 3. Moreover, the irradiation distribution is seen to be identical both qualitatively (see Figure 6) and quantitively (see Table 2) for all the values tested. The pixelation set of 3 × 3 is, hence, selected.

The effects of the divisions are observed to be considerably more pronounced (see Figure 7). As can be seen, there exists an obvious shift in the irradiation contour when the divisions are varied. The irradiance can be unphysically developed with limited emission directions as the divisions are smaller than 8 × 8. The larger the number of divisions, the smoother the intensity distribution can be observed. It is noteworthy that the divisions of 3 × 3 and 10 × 10 were proposed by Ho [15] and Atci et al. [18], respectively; however, these sets seem to be insufficient to ensure the accuracy in our case. We then adopt the division set of 15 × 15 as it not only provides an irradiation field very similar to that from the 20 × 20 one but saves a large computational cost, i.e., 5 hours for the former as compared to 12.5 hours for the latter.

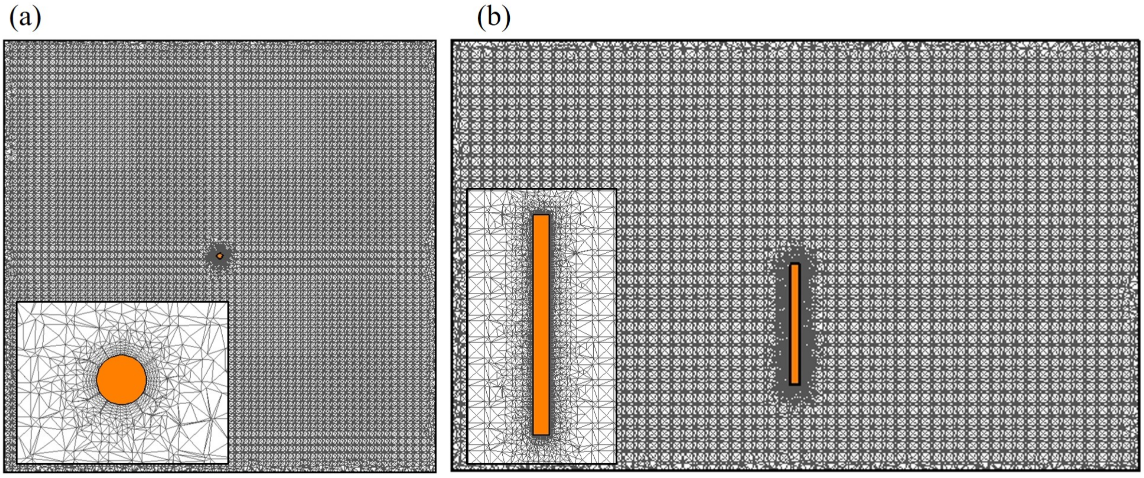

Figure 3. Example of mesh employed in (a) the xz-centerplane and (b) the xy-centerplane.

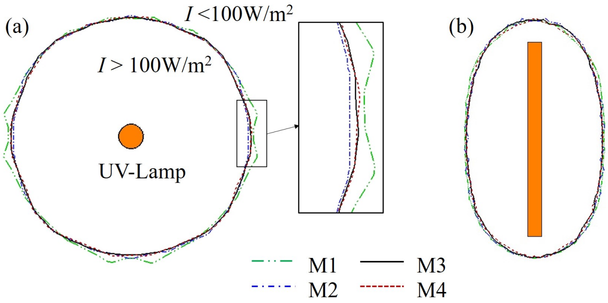

Figure 4. Variation in the boundary of $I = 100\,\mathrm{W/m^2}$ produced by a 100 W-lamp in (a) xz-centerplane and (b) the xy-centerplane with various mesh resolutions.

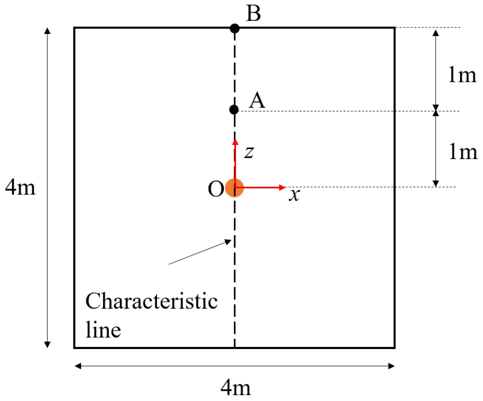

Figure 5. Definitions of the characteristic line, point A, and point B.

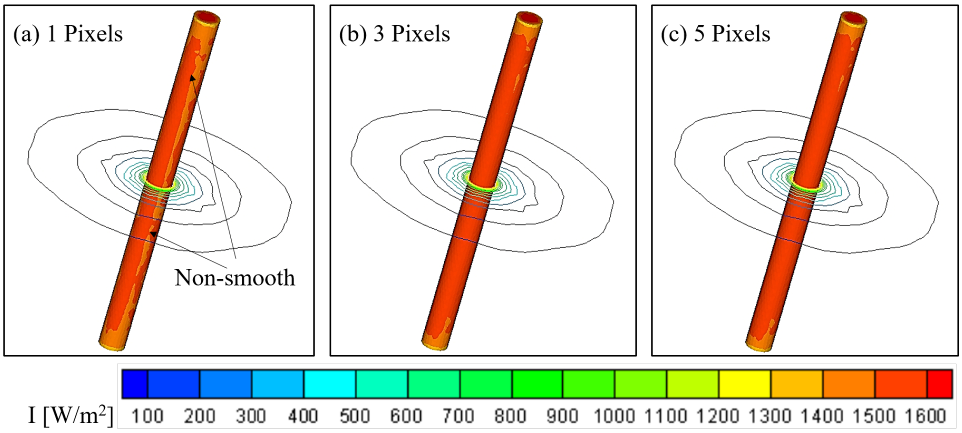

Figure 6. Variations in the intensity distribution on the 100 W-lamp and around it in the xz-centerplane with different pixelation sets.

3. Results and Discussion

3.1. UV Irradiance

In this part, the influences of the lamp wattage/power on the UV intensity distribution are presented and discussed. The wattage is varied in the range of $P =$ 30–100 W. The surrounding air absorption is assumed to be neglected in our present work.

Figure 8 shows the UV intensity along the characteristic line produced by various lamp powers. For all cases, the intensity is seen to be extremely high near the lamp's surface but tends to reduce with the

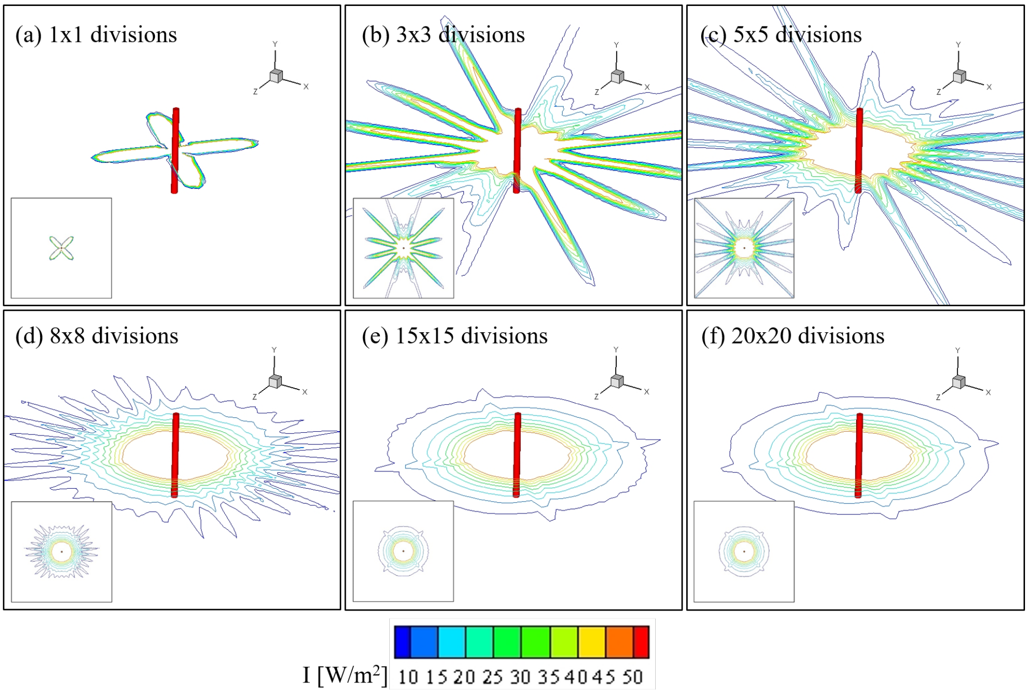

Figure 7. Variations in the irradiation field on the 100 W-lamp and in the xz-centerplane with different division sets.

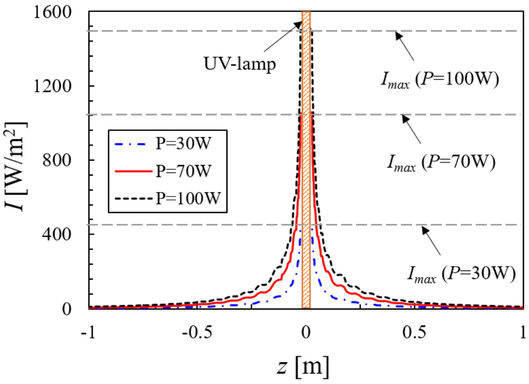

Figure 8. UV intensity distribution along the characteristic line.

increasing distance. The maximum intensity value, I_{max}, is found on the lamp; it is important to note that I_{max} is not always equivalent to the initial intensity I_0. For instance, with a 100 W-lamp, the largest value on the characteristic line is of $I_{max} = 1508.6\,\mathrm{W/m^2}$ being ~1.65 times greater than that of I_0. This phenomenon is probably due to the radiative emission mechanism and was also observed in [18]. Additionally, the maximum intensity gets drastically smaller as the lower wattage is employed; indeed, I_{max} on the characteristic line reduces by up to ~3.3 times when P decreases from 100 W to 30 W.

The results for the UV irradiation distribution in the central xz and xy planes are presented in Figure 9. It occurs that the UV intensity variation is significantly more obvious in the horizontal plane. As can be observed, the UV rays are distributed nearly symmetrically in the xy-centerplane. Moreover, the formation of high-intensity regions is noted around the lamp; these zones drastically enlarge with the increasing lamp power. For example, the coverage radius of the UV intensity larger than $50\,\mathrm{W/m^2}$ from a 100 W-lamp is estimated to be 2.6 times greater than that from a 30 W-one; in detail, it is 0.392 m and 0.175 m for the former and the latter, respectively.

3.2. Bactericidal effects

The UV disinfection effectiveness associated with the bactericidal effects of various lamp wattages is reported and analysed in this part. As introduced before, we investigate three different virus types, i.e., the *Corona-SARS*, the *Herpes*, and the *HIV* viruses. The exposure duration is assumed to be fixed at $t = 5\,\mathrm{s}$. In addition, the effective bactericidal rate is chosen to be $b_e = 85\,\%$. Furthermore, the area within which more than 85 % of the total active viruses are eliminated, i.e., $b \geq b_e$, is defined as the effective sterilization zone (see Figure 10).

Figure 11 illustrates the bactericidal effect on the *Corona-SARS* virus. As expected, the higher the lamp wattage employed, the greater the bactericidal effect can be observed in both the central xz and xy planes. As can be observed, the 30 W-lamp generates a relatively small effective sterilization zone; however, this zone is seen to be significantly extended with $P \geq 70\,\mathrm{W}$. Indeed, r_e is increased by ~1.46 and ~1.76 times for $P = 70\,\mathrm{W}$ and 100 W, respectively, as compared to that of $P = 30\,\mathrm{W}$ (see Table 3). The effective disinfection is, however, seen to not cover the whole room for all the lamp powers studied in

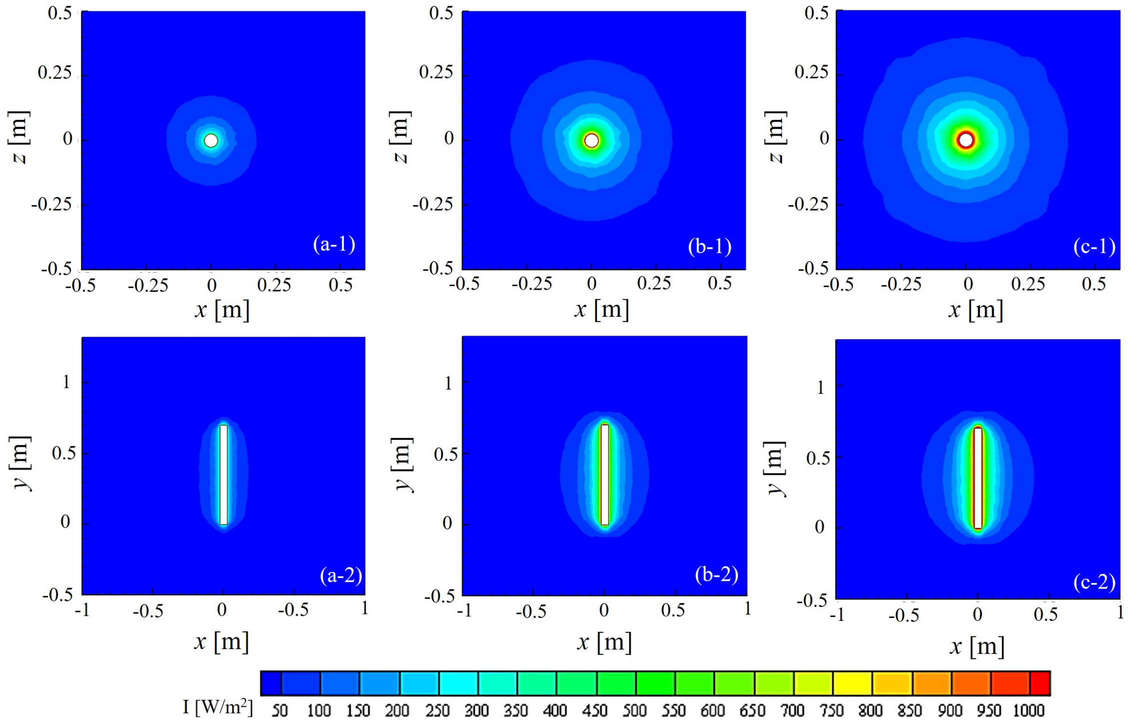

Figure 9. Simulated UV irradiation field in (1) the xz-centerplane and (2) the xy-centerplane produced by a UV-lamp of (a) 30 W, (b) 70 W and (c) 100 W.

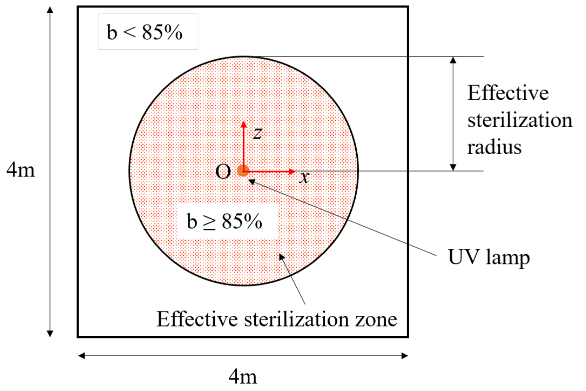

Figure 10. Definitions of the effective sterilization zone and its radius, r_e, in the xz-centerplane.

P	***Corona-SARS***	***Herpes***	***HIV***
30 W	0.925 m	0.71 m	0.175 m
70 W	1.365 m	1.075 m	0.325 m
100 W	1.625 m	1.285 m	0.405 m

Table 3. Results for r_e of various lamp wattages.

our study. For instance, despite the fact that the bactericidal rate is greatly improved with $P = 100$ W, there still exists a large ineffective sterilization zone above the lamp (see Figure 11c-2), resulting in the high possibility of a large number of viruses still surviving near the ceiling and floor. A higher lamp wattage is, hence, suggested in case absolute disinfection is required.

Figure 12 shows the UV bactericidal performance of a 70 W-lamp against various types of viruses. The bactericidal effect is determined to strongly depend on the targeted virus types. It is evident that the disinfection becomes more ineffective with viruses less sensitive to the UV rays, i.e., smaller microorganism susceptibility. As can be observed, the effective sterilisation zone against *HIV* type is very small and formed very close to the lamp (see Figure 12c and Table 3); indeed, its radius is only of $r_e = 0.405$ m when the highest wattage, i.e., $P = 100$ W, is utilised, leading to a substandard disinfection in almost the whole room.

Furthermore, the larger the UV sensitivity, the further distance that the absolute disinfection ($b = 100\,\%$) against the virus takes place (see Figure 13). The bactericidal rate is extremely low at the most further location, i.e., at the surrounding walls; it is only 8.98 % against the *HIV* virus even when the disinfection is performed with a 100 W-lamp. It is good to point out that our simulation results are well in line with those obtained from an analytical approach in [24].

4. Conclusions

An investigation of the bactericidal effectiveness of a single UV lamp was conducted using a numerical approach. In this work, we targeted three different types of viruses: *Corona-SARS*, *Herpes* (type 2), and *HIV*. The lamp, whose wattage varied in the interval of $P = 30$–100 W, had a cylindrical shape and was

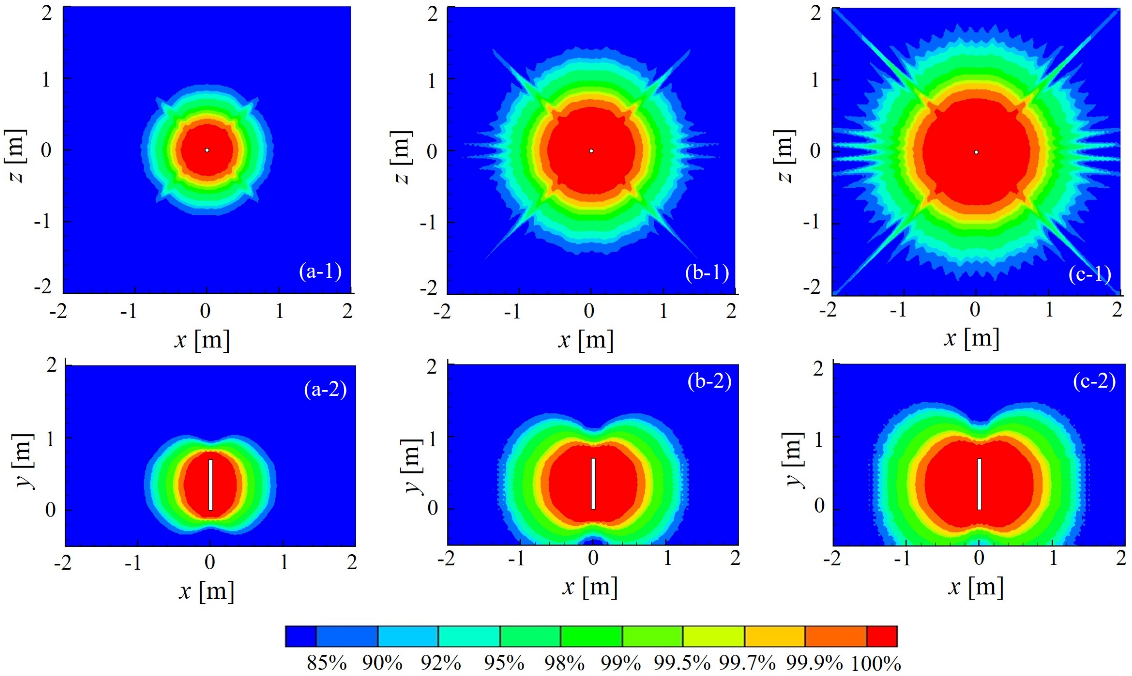

FIGURE 11. Bactericidal effect in (1) the xz-centerplane and (2) the xy-centerplane produced by a UV lamp of (a) 30 W, (b) 70 W, and (c) 100 W; the virus considered is of *Corona-SARS* type.

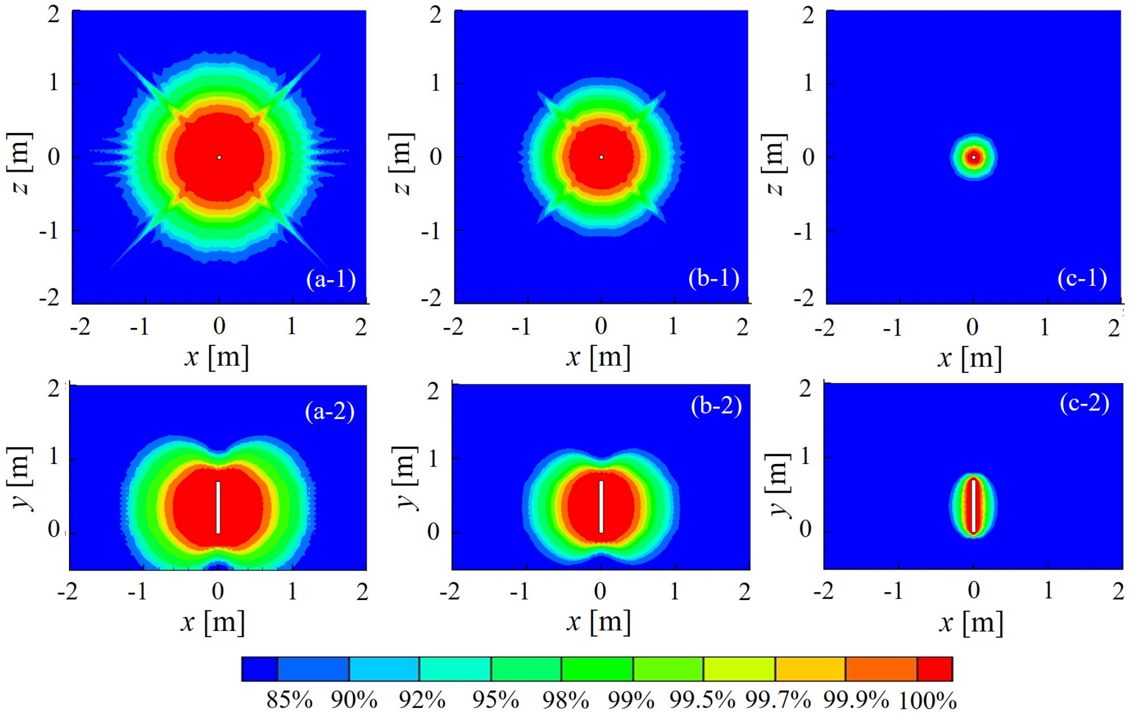

FIGURE 12. Bactericidal effect in (1) the xz-centerplane and (2) the xy-centerplane produced by a UV lamp of 70 W; the virus considered is of (a) *Corona-SARS*, (b) *Herpes*, and (c) *HIV* types.

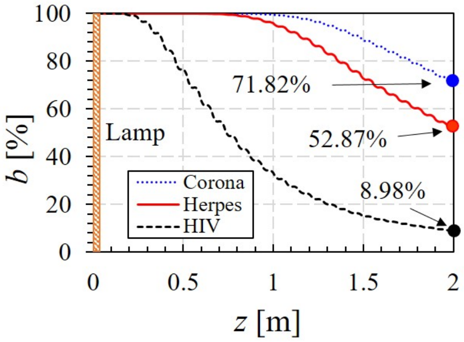

Figure 13. Bactericidal rate against various virus types as a function of the distance with the lamp power of 100 W.

placed in a vertical position. The UV irradiance was computed by the Finite Volume Method coupled with the Discrete Ordinates model; its modelling parameters were determined to be 3×3 and 15×15 for the pixelation and division sets, respectively.

For the radiation distribution, the UV intensity was observed to be reduced with an increase in distance to the lamp. Additionally, the lamp power was noted to have a strong effect on the UV distribution. Specifically, the higher the power, the larger the maximum intensity and significantly greater high-intensity zones around the lamp. With a 100 W-lamp, the zone within which $I \geq 50\,\mathrm{W/m^2}$ had a ~2.6 times larger radius as compared to that created by a 30 W-one.

In addition, it was observed that the larger lamp wattage led to a greater bactericidal effect expressing the more efficient disinfection in the room. In detail, when compared to a 30 W-lamp, the radius of the effective sterilisation zone r_e was extended by ~1.46 times and ~1.76 times for the 70 W- and 100 W-ones, respectively. However, it is worth noting that the disinfection effectiveness was not as high in the whole room even when the highest wattage, i.e., 100 W, was used; this could result in the virus possibly surviving in the areas far away from the lamp. Moreover, the bactericidal performance could vary considerably according to the virus type. The lower the microorganism susceptibility, the smaller the bactericidal effects against the virus, and the smaller the effective sterilization zone. Furthermore, the bactericidal rate could be as low as approximately 8.98 %, at the surrounding walls for viruses less sensitive to UV rays such as the *HIV*.

Regarding future works, we plan to build experimental models and carry out a validation for our numerical approach. In addition, the effects of the airflow and temperature on the UV disinfection performance are also of interest.

List of symbols

P	UV lamp wattage [W]
I	UV intensity [W/m^2]
I_0	Initial UV intensity [W/m^2]
I_{max}	Maximum UV intensity [W/m^2]
r_e	Effective sterilisation radius [m]
t	Exposure duration [s]
b	Bactericidal rate [%]
k	Microorganism susceptibility [m^2/J]

Acknowledgements

This research was funded by the People's Committee of Da Nang city, under a contract number 22/HĐ-SKHCN (2021).

References

[1] S. Ilyas, R. R. Srivastava, H. Kim. Disinfection technology and strategies for COVID-19 hospital and bio-medical waste management. *Science of the Total Environment* **749**:141652, 2020. `https://doi.org/10.1016/j.scitotenv.2020.141652`.

[2] Y. Ren, L. Li, Y.-m. Jia. New method to reduce COVID-19 transmission-the need for medical air disinfection is now. *Journal of Medical Systems* **44**(7):1–2, 2020. `https://doi.org/10.1007/s10916-020-01585-8`.

[3] S. M. Sharafi, K. Ebrahimpour, A. Nafez. Environmental disinfection against COVID-19 in different areas of health care facilities: a review. *Reviews on Environmental Health* **36**(2):193–198, 2020. `https://doi.org/10.1515/reveh-2020-0075`.

[4] J.-S. Chen. Enhancing air quality for embedded hospital germicidal lamps. *Sustainability* **13**(4):2389, 2021. `https://doi.org/10.3390/su13042389`.

[5] Z. Han, E. Pappas, A. Simmons, et al. Environmental cleaning and disinfection of hospital rooms: A nationwide survey. *American Journal of Infection Control* **49**(1):34–39, 2021. `https://doi.org/10.1016/j.ajic.2020.08.008`.

[6] M. Raeiszadeh, B. Adeli. A critical review on ultraviolet disinfection systems against COVID-19 outbreak: Applicability, validation, and safety considerations. *Acs Photonics* **7**(11):2941–2951, 2020. `https://doi.org/10.1021/acsphotonics.0c01245`.

[7] World Health Organisation, World Meteorological organisation, United Nations Environment Program, International Commission on Non-Ionising Radiation Protection. Global solar UV index : a practical guide, 2002.

[8] W. J. Kowalski, W. Bahnfleth, M. T. Hernandez. A genomic model for predicting the ultraviolet susceptibility of viruses. *IUVA news* **11**(2):15–28, 2009.

[9] B. Andersen, H. Bånrud, E. Bøe, et al. Comparison of UV C light and chemicals for disinfection of surfaces in hospital isolation units. *Infection Control & Hospital Epidemiology* **27**(7):729–734, 2006. `https://doi.org/10.1086/503643`.

[10] M. Bentancor, S. Vidal. Programmable and low-cost ultraviolet room disinfection device. *HardwareX* **4**:e00046, 2018. `https://doi.org/10.1016/j.ohx.2018.e00046`.

[11] P. Chanprakon, T. Sae-Oung, T. Treebupachatsakul, et al. An ultra-violet sterilization robot for disinfection. In *2019 5th International Conference on Engineering, Applied Sciences and Technology (ICEAST)*, pp. 1–4. IEEE, 2019. `https://doi.org/10.1109/iceast.2019.8802528`.

[12] M. Guettari, I. Gharbi, S. Hamza. UVC disinfection robot. *Environmental Science and Pollution Research* **28**:40394–40399, 2021. `https://doi.org/10.1007/s11356-020-11184-2`.

[13] A. Vyshnavi, A. Manasa, C. Hamsika, et al. UV disinfection robot with automatic switching on human detection. *EAI Endorsed Transactions on Internet of Things* **6**(23), 2020. `https://doi.org/10.4108/eai.25-9-2020.166364`.

[14] H. Pan, M. Orava. Performance evaluation of the UV disinfection reactors by CFD and fluence simulations using a concept of disinfection efficiency. *Journal of Water Supply: Research and Technology—AQUA* **56**(3):181–189, 2007. `https://doi.org/10.2166/aqua.2007.101`.

[15] C. Ho. Evaluation of reflection and refraction in simulations of ultraviolet disinfection using the discrete ordinates radiation model. *Water Science and Technology* **59**(12):2421–2428, 2009. `https://doi.org/10.2166/wst.2009.260`.

[16] H. Sobhani, H. Shokouhmand. Effects of number of low-pressure ultraviolet lamps on disinfection performance of a water reactor. *Journal of Water Process Engineering* **20**:97–105, 2017. `https://doi.org/10.1016/j.jwpe.2017.08.021`.

[17] A. Capetillo, C. J. Noakes, P. A. Sleigh. Computational fluid dynamics analysis to assess performance variability of in-duct UV-C systems. *Science and Technology for the Built Environment* **21**(1):45–53, 2015. `https://doi.org/10.1080/10789669.2014.968512`.

[18] F. Atci, Y. E. Cetin, M. Avci, O. Aydin. Evaluation of in-duct UV-C lamp array on air disinfection: a numerical analysis. *Science and Technology for the Built Environment* **27**(1):98–108, 2020. `https://doi.org/10.1080/23744731.2020.1776549`.

[19] Y. Yang, H. Zhang, A. C. Lai. Lagrangian modeling of inactivation of airborne microorganisms by in-duct ultraviolet lamps. *Building and Environment* **188**:107465, 2021. `https://doi.org/10.1016/j.buildenv.2020.107465`.

[20] A. G. Buchan, L. Yang, K. D. Atkinson. Predicting airborne coronavirus inactivation by far-UVC in populated rooms using a high-fidelity coupled radiation-CFD model. *Scientific reports* **10**(1):1–7, 2020. `https://doi.org/10.1038/s41598-020-76597-y`.

[21] N. Ropathy, H. L. Choo, C. H. Yeong, Y. H. Wong. UVC light simulation for room disinfection system. In *MATEC Web of Conferences*, vol. 335, p. 03012. EDP Sciences, 2021. `https://doi.org/10.1051/matecconf/202133503012`.

[22] Ansys, Inc. ANSYS FLUENT theory guide. *Canonsburg, Pa* **794**, 2011.

[23] E. Mitscherlich, E. H. Marth. *Microbial survival in the environment: bacteria and rickettsiae important in human and animal health.* Springer Science & Business Media, 2012. `https://doi.org/10.1007/978-3-642-69974-0`.

[24] N. D. M. Phan, N. Q. H. Tran, D. C. Tran, et al. An ultraviolet C light-emitting robot design for disinfection in the operating room. In *Recent Trends in Mechatronics Towards Industry 4.0*, pp. 185–196. Springer, 2022. `https://doi.org/10.1007/978-981-33-4597-3_18`.

Acta Polytechnica **62**(4):427–437, 2022
`https://doi.org/10.14311/AP.2022.62.0427`

Published by the `Czech Technical University in Prague`

A MODEL OF ISOTOPE TRANSPORT IN THE UNSATURATED ZONE, CASE STUDY

Josef Chudoba*, Jiřina Královcová, Jiří Landa, Jiří Maryška,
Jakub Říha

Technical University of Liberec, Faculty of Mechatronics, Informatics and Interdisciplinary Studies, Studentská 2, Liberec, Czech Republic

* corresponding author: `josef.chudoba@tul.cz`

Abstract.

This work deals with a groundwater flow and solute transport model in the near-surface (predominantly unsaturated) zone. The model is implemented so that it allows simulations of contamination transport from a source located in a geological environment of a rock massif. The groundwater flow model is based on Richards' equation. Evaporation is computed using the Hamon model. The transport model is able to simulate advection, diffusion, sorption and radioactive decay. Besides the basic model concept, the article also discusses potential cases that could lead to non-physical solutions. On three selected examples, which include, for example, rapidly changing boundary conditions, the article shows the solvability of such cases with the proposed model without unwanted effects, such as negative concentrations or oscillations of solution, that do not correspond to inputs.

Keywords: Richards' equation, unsaturated zone, groundwater flow in unsaturated zone, solute transport.

1. Introduction

In the Czech Republic, it is planned to dispose of the spent nuclear fuel within the deep repository in hard crystalline rock. It is a similar concept to those adopted in Sweden (www.skb.se) and Finland (www.possiva.fi) [1–3] with one of the main differences being the near zero terrain gradient over their coastal deep repository sites. In the Czech Republic, the repository candidate sites have an average altitude of about 500 m with locally steep gradients, which means that it is necessary to focus closely on both saturated and unsaturated flow and solute transport.

The biosphere model is a part of the safety analyses for ensuring the safety of a planned deep repository of spent nuclear fuel and highly active wastes. For a purpose of computation of a possible radionuclide impact on biosphere it is necessary to know their distribution (concentration or activity) in its vicinity, i.e. in a groundwater (near its level) where there is a possibility of direct extraction via pumping and also in the unsaturated zone above the groundwater level. A prediction of radionuclide concentration distribution in groundwater is done by transport simulations along with groundwater flow simulations (both mainly in saturated zone). Such a model usually doesn't provide us with enough detailed concentrations in a zone near the surface where the solute transport has an entirely different character (due to the low saturation).

This problem is not new. It is being studied both in the context of deep repositories and potential environmental contamination. Existing SW tools (Pandora [4], ResRad [5], Hydrus [6] used in this field do allow for transport simulation in the unsaturated zone, but they show numerical instabilities in the case of dynamically changing flow boundary condition. This article uses case studies to show how to deal with such instabilities.

With a biosphere module in mind, it is necessary to evaluate the near-surface radionuclide distribution using a more detailed model of the unsaturated zone (based on a known concentration distribution in a saturated zone and expected precipitation amounts). For such simulations, there is a variety of existing tools. An overview of their selection along with their characteristic features may be found in Steefel, Appelo and Arora [7]. The alternative is to implement one of the well-known concepts for transport in unsaturated and partially saturated environments, which is the case in a work presented in this article. The aim was to create a software tool for biosphere simulations, which uses Flow123d [8] and [9], verified against other codes in [10] for transport simulations in the saturated zone (geosphere). Flow123d provides us with pressure distribution, velocity vectors and radionuclide concentrations in both mobile and immobile phases of a rock massif saturated environment. For the calculation of a radionuclide concentration time-space distribution in an unsaturated zone of defined model subdomain, we use the precipitation amount data. So far, in the phase of model implementation and testing, we used data from meteorological station Praha Klementinum, which are (for daily precipitation amounts) available for past ca 200 years. The implementation includes the Hamon evapotranspiration model [11]. The unsaturated zone flow simulation is based on Richards' equation and transport simulation is based on the advection-diffusion equation. For the approximation of both flow and transport, the numerical scheme shown in [6] and [12] is used (as is the case of, for example, Hydrus [6]).

This article deals with some of the aspects of the unsaturated flow and transport model implemented as an extension of a 3D hydrogeological and transport model of a site with a deep repository as a source of radionuclides that have the potential to migrate from the repository to a biosphere. The unsaturated zone model outputs serve as an input for radionuclide transport computations in a biosphere. The much needed mutual interconnection of all the modules along with the necessary customization of unsaturated zone model input and output form is the main reason for our own implementation, instead of using existing SW such as Hydrus. This also means that there is no need for installation or execution of any third party SW tools. We managed to ensure 1) same data structure for transport simulations in both saturated and unsaturated zones, which allows us to avoid difficult interconnection of inputs and outputs of various simulation SWs and 2) a support for sensitivity analysis of the whole path from a source to a biosphere. The downside is that we had to deal with problems linked to numerics, such as solution oscillations or negative concentrations. Besides the model itself, the article also shows three case studies to present the model's usability, including the sensitivity analysis performed in accordance with [13].

2. MODEL CONCEPT

The unsaturated zone model was implemented with the aim to simulate the radionuclide transport from a geosphere to a biosphere. It assumes a known time-space distribution of radionuclide concentration in a part of geosphere that is close to groundwater level. This concentration distribution is acquired from the transport model of a site with a deep repository, which has concentration values in given times and discrete points of a simulation domain as an output. In the case of Flow123d simulation tool, the time-dependent elementwise constant values of concentration are available. It is possible to identify the near-surface zones of the model domain for which the more detailed unsaturated zone simulations will be performed with the aim of acquiring a higher resolution of the concentration distribution near a surface.

While in the saturated part of the geosphere, the flow has predominantly horizontal character, in the unsaturated zone, the flow of water and dissolved contaminants is mainly vertical. This is why the unsaturated zone model was limited to one dimension in the direction of z axis (with the direction of rising altitude). For each selected near-surface element, the separate unsaturated zone simulation is performed with the following basic inputs:

- Time evolution of contamination concentration in water – acquired from an output of the 3D transport model; values are used as a transport boundary condition for the 1D model,
- Vertical profile of soil composition in the unsaturated zone (alternatively of the van Genuchten parameters),
- Depth where the saturation is equal to one, i.e. depth of the groundwater level,
- Time evolution of precipitation amounts; used as a flow boundary condition,
- Time evolution of evaporation values (implemented via Hamon model [11]),
- Time evolution and location of sources in a model domain.

The definition of initial conditions requires the lower part of the model domain to be saturated and, in sake of numerical stability, requires the saturated part to be at least few meters thick. The initial flow conditions in the model domain as a whole are usually derived from the groundwater level (hydraulic/piezometric head) which could be determined by a direct measurement or an expert estimation. The flow boundary condition on the top of the model domain is given by the volume of the water entering the profile (could be time dependent) and on the bottom, by hydraulic head (could also be time dependent). Sources could be defined to cover the root withdrawal.

For the transport simulation, the top boundary condition is usually zero concentration (when we assume the source of contamination to be located deep in the geosphere). The bottom boundary condition is defined based on the concentration values acquired from a simulation of the saturated zone. This boundary condition interconnects the saturated and the unsaturated model. The transport model includes sorption, diffusion and radioactive decay.

The 1D model domain is discretized with a given step. The values of pressure head, water content and flux in each discretization node are the outputs of the flow simulation. The values of concentrations in each discretization node are the outputs of the transport simulation.

3. MATHEMATICAL AND PHYSICAL MODEL

3.1. MODEL OF FLOW

In the saturated zone, all pores are filled with water and the pressure head $h \geq 0$. The groundwater flow could be both horizontal and vertical. And in the unsaturated zone, the pores could be filled with water or with air. The pressure head $h < 0$. The flow is predominately vertical. That is why we limited the model to one dimension.

The flow in the unsaturated zone is described by Richards' equation [14]:

$$\frac{\partial \theta(h)}{\partial t} = \frac{\partial}{\partial z}\left(K(\theta, h)\left(\frac{\partial h}{\partial z} + 1\right)\right) - S, \qquad (1)$$

where h [m] is the pressure head, θ [1] is the water content, t [s] is the time, z [m] is the vertical axis, S [s^{-1}] are the sources and K [$\mathrm{m\,s}^{-1}$] is the unsaturated hydraulic conductivity.

In equation (1), the principal variable is h. Variable $\theta(h)$ and parameter $K(h)$ are linearly dependent on the current value of pressure head h. According to van Genuchten [15], this dependence could be described by following equations:

$$\theta(h) = \begin{cases} \theta_r + \dfrac{\theta_s - \theta_r}{\left[1 + |\alpha h|^n\right]^m}, & h < 0 \\ \theta_s, & h \geq 0 \end{cases}, \qquad (2)$$

$$K(h) = K_S \cdot S_e^{0.5} \cdot \left[1 - \left(1 - S_e^{1/m}\right)^m\right]^2, \qquad (3)$$

$$S_e = \frac{\theta(h) - \theta_r}{\theta_s - \theta_r},$$

$$m = 1 - \frac{1}{n},$$

where θ_r [1] is the residual water content, θ_s [1] is the saturated water content, α [m^{-1}] is the inverse of the air-entry value, n [1] is the empirical shape-defining parameters and K_s [$\mathrm{m\,s}^{-1}$] is the saturated hydraulic conductivity.

Van Genuchten parameters α and n depend on the soil composition: fraction of clay, silt and sand and bulk density of soil. There is no analytical formula linking the soil composition to van Genuchten parameters. Their values could be estimated, for example, by using the Rosetta SW [16] which is based on a quasi-empirical model.

For a particular simulation, it is necessary to also input (aside from soil parameters) the boundary and initial conditions. On each model boundary (there are only two since the model domain is 1D) it is possible to input either flux or pressure head. The boundary conditions could be changed in the course of simulation, both their type and their value. In each time step, it is necessary for the pressure head to be specified on at least one boundary. The initial conditions (in the form of pressure head values) are derived from the groundwater level in the model domain. It is possible to define sources S [s^{-1}] which represent water withdraval through roots or a well.

The model domain is divided into a mesh of $n - 1$ line elements with n nodes. Richards' equation (1) has no analytical solution; in a model, it is solved using the Piccard numerical scheme [17]. The solution is in a form of pressure head in each computational node and each simulation time step.

3.2. Model of transport

In the unsaturated zone, the contamination may generally exist dissolved in three phases – liquid, solid and gaseous. In our concept, we do not account for a contamination transfer to gaseous phase. The reasoning behind this is the long simulation time in comparison to rock residence time of isotopes in the gaseous form.

The concentration of dissolved contaminants/isotopes is very low, which is why the model uses only the linear sorption isotherm. The transport model also includes diffusion and radioactive decay. In each simulation time, we also assume an equilibrium between concentrations in solid and liquid phases given by the distribution coefficient. Based on these assumptions, the dependence of concentration on time and space could be described by the advection-diffusion equation (4) [6].

$$\frac{\partial \theta c_k}{\partial t} + \frac{\partial \rho s_k}{\partial t} = \frac{\partial}{\partial z}\left(\theta D_k^w \frac{\partial c_k}{\partial z}\right) - \frac{\partial q c_k}{\partial z} - \mu_{w,k}\theta c_k - \mu_{s,k}\rho s_k + \sum_{\substack{m=1 \\ m \neq k}}^{n} \mu_{w,m}\theta c_m + \sum_{\substack{m=1 \\ m \neq k}}^{n} \mu_{s,m}\rho s_m + \gamma_{w,k}\theta + \gamma_{s,k}\rho - r_k, \qquad (4)$$

where θ [1] is the water content, ρ [$\mathrm{kg\,m}^{-3}$] is the rock density, z [m] is the vertical axis, c_k [$\mathrm{kg\,m}^{-3}$] is the concentration of isotope k in a liquid phase, s_k [1] is the concentration of isotope k in a solid phase, D_k^w [$\mathrm{m}^2\,\mathrm{s}^{-1}$] is the diffusion coefficient of isotope k, q [$\mathrm{m\,s}^{-1}$] is the flux, $\mu_{w,k}$ and $\mu_{s,k}$ [s^{-1}] is the radioactive decay of isotope k in liquid and solid phases, $\gamma_{w,k}$ [$\mathrm{kg\,m}^{-3}\,\mathrm{s}^{-1}$] is the zero order reaction in a liquid phase, $\gamma_{s,k}$[s^{-1}] is the zero order reaction in a solid phase, r_k [$\mathrm{kg\,m}^{-3}\,\mathrm{s}^{-1}$] are sources. The relationship between concentrations in solid phase s_k and in liquid phase c_k is given by equation (5).

$$s_k = k_{D,k} \cdot c_k, \qquad (5)$$

where $k_{D,k}$ [$\mathrm{m}^3\,\mathrm{kg}^{-1}$] is the distribution coefficient of linear sorption for isotope k. Boundary conditions on both ends of the model domain are given in a form of concentrations in the liquid phase. The model allows for the boundary conditions to change over time. The initial conditions are given as concentrations in the liquid phase in individual computational nodes; the initial concentrations in the solid phase are then computed using equation (5).

The differential equation (4) is numerically solved using the finite elements method. The computation uses the same discretisation as the model of flow. The solution is in the form of concentration of each contaminant in each node and at each simulation time.

4. Model instabilities

While simulating the flow and transport using the model described above, some instable states may arise. They needed to be dealt with during the implementation. Potential instabilities must be eliminated by an appropriate choice of parameter values. This section provides an overview of known potential unstable states along with a method that was used to deal with them in the model implementation.

The evaporation from the model surface may be defined by **outflux boundary condition**. This may cause a non-physical state where the withdrawn water doesn't exist in the model domain. This would lead to results limitedly approaching $h \to -\infty$ and $\theta \to \theta_r$, which would require the simulation time step to be $\Delta_t \to 0$. A possible solution is to define the evaporation as a source (water is withdrawn from the defined depth). This approach allows for the simulation of 1) water withdrawal through roots, 2) evaporation and 3) near-surface water circulation. Another possible solution is to define the model domain extent so that its bottom part remains saturated throughout the simulation. If the defined **initial conditions imply non-zero flux in the model domain**, it results in a rapid stabilization in the first few simulation time steps, which may lead to significant computed groundwater fluxes. This may lead to a non-physical solution and a necessity to shorten the simulation time step. To control the time step, the Courant number defined as $Cr = \frac{|q \cdot \Delta t|}{\theta \cdot \Delta z}$ [1] may be used. The solution is stable when $Cr \leq 1$. Based on the knowledge of $\max_i Cr_i$ (here, the lower index i stands for the element of discretisation) the time step may be adjusted accordingly. When **changing the flow boundary conditions during the course of simulation**, similar problems as in the previous case may arise. Those problems may be generally solved by lowering the simulation time step and making the changes in boundary conditions gradual, if possible. Because the flux may be discontinuous in time, it is necessary to estimate the Courant number and adjust the time step accordingly.

Unstable and non-physical solutions may be generally caused by **long flow-simulation time step**. The problem may be fixed by an estimation of the time step using the Courant number.

When simulating the **transport**, there may be oscillations in the solution and negative concentrations in cases where the **advective flux dominates over the diffusion** (along with suboptimal time and space discretisation). Maximum transport-simulation time step may be set based on Péclet number $Pe = \frac{q \Delta x}{\theta D}$ [1], where $q\,[\mathrm{m\,s^{-1}}]$ is the flux, Δx is the element size [m], θ is the water content [1] and D is the diffusion coefficient $[\mathrm{m^2\,s^{-1}}]$. Numerical oscilations are negligible if $Pe < 5$. The denominator in the equation for Péclet number computation includes the diffusion coefficient, which consists of hydrodynamical dispersion and molecular diffusion. In the case of 1D simulation, it means $D^W = \frac{D_L|q|}{\theta} + D_w \tau_w$, where D_L is the longitudal dispersivity [m], D_w is the coefficient of molecular diffusion $[\mathrm{m^2\,s^{-1}}]$ and $\tau_w = \frac{\theta^{7/3}}{\theta_s^2}$ is tortuosity. Péclet number may be lowered by including both dispersion and molecular diffusions in the simulation.

Oscillations of the solution and/or negative concentrations may also be caused by **changing concentration in transport boundary conditions**. Such problems may be solved by lowering the transport simulation time step.

An unstable solution may occur in the case of a **too small model domain with respect to the pressure head value given as the flow boundary condition**. If the bottom boundary condition is a pressure head, which is not $h \gg 0$, then, if the precipitation amounts are high, the saturated/unsaturated zone interface moves up but the boundary condition remains the same. This results in a significant pressure head gradient in nodes close to the bottom boundary and consequently, unrealistically high fluxes. Such problems may be solved by extending the model domain so that it captures a greater part of the saturated zone.

5. CASE STUDIES

This part of the article shows three case studies. The first one is a synthetic task that includes a simulation of flow and transport with regularly changing boundary conditions. The second one examines the sensitivity of the output on the precipitation amount. And finally, the third one shows the expected radionuclide migration in the case of a realistic precipitation boundary condition (data from Praha Klementinum; available since 1804). This case also includes the evaporation computed using the Hamon model, which is based on temperature measurements, latitude, and date (last two quantities are used for the computation of daylight length). Bottom boundary conditions as well as initial conditions were, in all three cases, derived from the saturated transport simulation with contamination source located 500 m below surface. This regional saturated model is not discussed here; parameters derived from it are shown where relevant. Case studies are evaluated based on the concentration evolution (depth dependent).

5.1. CASE 1 – PERIODIC PRECIPITATION EVOLUTION

The first case simulates a flow and solute transport from a 10 m depth towards a surface. The model domain is divided into 100 computational elements (101 nodes). The z axis is in the direction of rising altitude (the surface is at $z = 10\,\mathrm{m}$). The simulation period is 5000 days with a simulation time step of 1 day.

The soil properties are constant throughout the model domain. The soil is 40 % silt, 15 % clay and 45 % sand. Its dry density is $1500\,\mathrm{kg\,m^{-3}}$. This composition corresponds to the following parameters: $K_S = 1.912 \cdot 10^{-6}\,\mathrm{m\,s^{-1}}$, $n = 1.469$, $\theta_r = 0.0492$, $\theta_s = 0.3687$, $a = 1.355\,\mathrm{m^{-1}}$.

The flux, representing precipitation (after subtraction of evaporation), is used as a flow boundary condition on the top boundary. The time evolution of

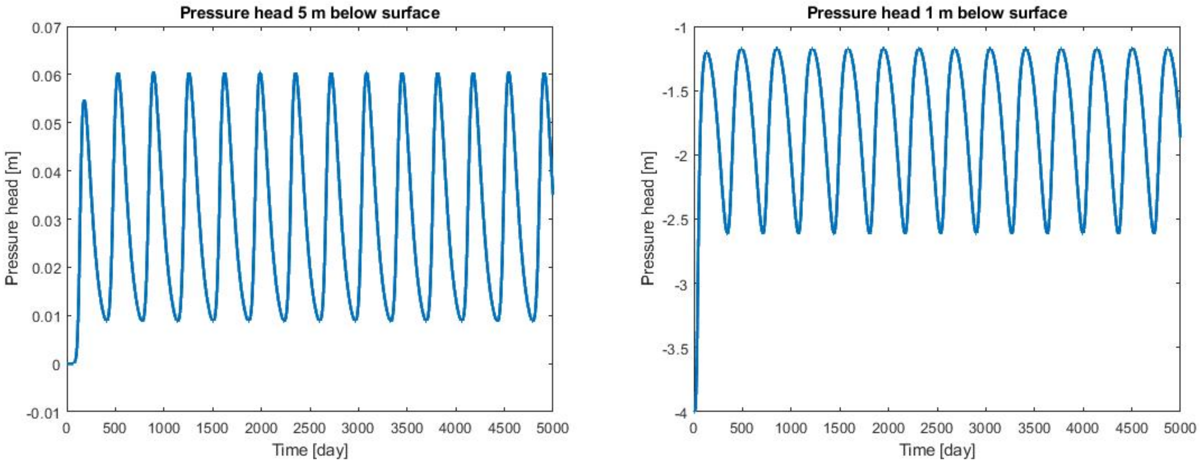

Figure 1. Pressure head time evolution at 5 m depth (left) and 1 m depth (right).

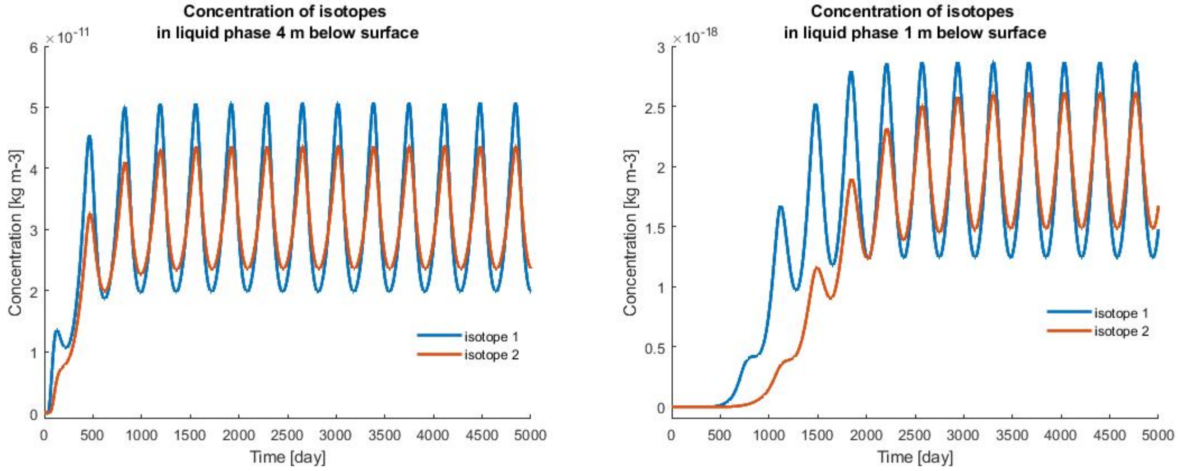

Figure 2. Concentration time evolution at 4 m depth (left) and 1 m depth (right).

the boundary condition has a sinus shape with a 365-day periodicity. Its values for individual simulation times were (for the expected influx of 365 mm y^{-1}) calculated as $okp_{p_{Flux}} = 365 - 438 \cdot \sin\left(\frac{2\pi t}{365}\right)$ [mm y^{-1}]. A constant pressure head of 5 m is specified on the bottom boundary throughout the simulation. This corresponds to a groundwater level 5 m below surface, which is also how the initial conditions were defined.

The flow simulation result is the time-space distribution of the pressure head and saturation. For example, at 5 m depth (where the groundwater level was situated at the simulation start), the pressure head oscillates between 0.009 and 0.061 m (see Figure 1, left). At one meter below the surface (see Figure 1, right), we can see an initial rise, followed by periodic oscillations between −2.61 and−1.17 m (difference of ca 1.44 m).

Based on the flow simulation results, the transport of two isotopes (noted isotope 1 and isotope 2) was simulated. Isotope 1 has a half-life of 10 000 days, its product is the stable isotope 2. The following parameters were used for the simulation: coefficient of molecular diffusion $1 \cdot 10^{-3}$ m^2 day^{-1} (i.e. $1.15 \cdot 10^{-8}$ m^2 s^{-1}), longitudal dispersivity 0.1 m, distribution coefficient 0 m^3 kg^{-1} for isotope 1 and 0.0001 m^3 kg^{-1} [18] for isotope 2.

The initial concentration for both isotopes is $1 \cdot 10^{-9}$ kg m^{-3} below the groundwater level (depths of 5–10 m) and zero above it. The bottom transport boundary condition is a constant concentration of $1 \cdot 10^{-9}$ kg m^{-3}. The model also assumes a horizontal flow in its saturated part, which means that the concentration there is kept at a constant value of $1 \cdot 10^{-9}$ kg m^{-3} (via prescription of nonzero sources in computational nodes) throughout the simulation.

Figure 2 shows examples of results at two depths: 4 m and 1 m. It is clear that after 2 000 days, the concentration evolutions adopt the periodicity of the precipitation evolution. Near the surface, the concentration is significantly lowered by an infiltration of clean water. In a realistic environment, the measure of dilution would be predetermined by many factors, such as soil type, unsaturated zone thickness, precipitation and evaporation amounts, roots, and wells.

Isotope	Half-life [y]	Diffusion coefficient $[\mathrm{m^2\,s{-}1}]$	Distribution coefficient $[\mathrm{m^3\,kg^{-1}}]$
^{14}C	5 700	1e-9	0.0005
^{36}Cl	301 000	1e-9	0.0
^{41}Ca	102 000	1e-9	0.0001
^{59}Ni	76 000	1e-9	0.01
^{79}Se	356 000	1e-9	0.0005
^{107}Pd	6 500 000	1e-9	0.0001
^{126}Sn	230 000	1e-9	0.0
^{129}I	16 100 000	1e-9	0.0
^{135}Cs	2 300 000	1e-9	0.01
^{238}U	4 468 000 000	1e-9	0.1

Table 1. Values of half-life, molecular diffusion coefficient and linear sorption distribution coefficient of selected isotopes used in the simulation.

5.2. Case 2 – radionuclide transport with realistic transport boundary condition, sensitivity on infiltration amount

This case deals with the transport of 10 real isotopes (^{14}C, ^{36}Cl, ^{41}Ca, ^{59}Ni, ^{79}Se, ^{107}Pd, ^{126}Sn, ^{129}I, ^{135}Cs and ^{238}U) which are expected to migrate from a deep repository. The isotope parameters used in the simulation are shown in Table 1. The regional saturated model transport simulation period was 500 000 years. As a consequence of a given radionuclide release scenario and transport parameters, the following isotopes had a high-enough concentration near the surface at the end of the simulation: ^{36}Cl, ^{41}Ca, ^{79}Se, ^{129}I. Concentrations of other isotopes were less than 1E-15 $\mathrm{g\,m^{-3}}$. For the four isotopes mentioned above, the unsaturated transport simulation was performed with an aim to determine the sensitivity of the concentration distribution on the infiltration amount.

The model domain is 10 m thick and discretized with a 0.1 m step. The simulation period was 500 000 y with a 0.1 y time step. The soil is sandy loam with the following parameters: $\theta_r = 0.065$, $\theta_s = 0.41$, $\alpha = 7.5\,\mathrm{m^{-1}}$, $n = 1.89$, $K_s = 1.228 \cdot 10^{-5}\,\mathrm{ms^{-1}}$. The saturated part of the model domain is 8 m thick (groundwater level 2 m below surface). This corresponds to bottom flow boundary condition of a constant 8 m pressure head. The simulations were carried out with various top flow boundary conditions that correspond to annual infiltrations of 0, 10, 20, 30, 40, 50, 60 and 80 $\mathrm{mm\,y^{-1}}$.

The transport initial condition was zero concentration throughout the domain. The bottom transport boundary condition had a form of concentration time evolution based on regional saturated model results (see Figure 3). These concentrations are also kept in the saturated part of the model domain throughout the simulation.

Table 2 shows the calculated values of ^{36}Cl, ^{41}Ca, ^{126}Sn and ^{129}I concentrations at simulation times of 50 000, 100 000 and 200 000 y and in depths of 0.3, 0.5 and 1.0 m as well as in the saturated zone. The results shown are for the infiltration amounts of 0, 20 and 50 $\mathrm{mm\,y^{-1}}$. There is a clear significant influence of the infiltration amount. For each isotope, simulation time, and given infiltration amount, the ratio between the unsaturated zone (at selected level) and the saturated zone concentration is about the same. The measure of dilution in the unsaturated zone is influenced mainly by the infiltration amount; the influence of the simulation time and isotope is negligible. Figure 4 shows the dependence of ^{129}I concentration on the depth and infiltration amount at a simulation time of 50 000 y. Figure 5 shows the evolution of ^{129}I concentration at selected depths.

5.3. Case 3 – precipitation and evaporation based on meteorological data

The model domain is 10 m thick and discretized with a 0.1 m step. The soil is sandy loam with the following parameters: $\theta_r = 0.065$, $\theta_s = 0.41$, $\alpha = 7.5\,\mathrm{m^{-1}}$, $n = 1.89$, $K_s = 1.228 \cdot 10^{-5}\,\mathrm{m\,s^{-1}}$.

The saturated part of the model domain is 7 m thick (groundwater level 3 m below surface). This corresponds to a bottom flow boundary condition of a constant 7 m pressure head. Flow boundary conditions on the top of the model domain are derived from meteorological measurements from the past 200 years [19]. The influx to the model domain is based on daily precipitation data. The evaporation is estimated based on mean temperatures using the Hamon model [11] and included in the simulation as a negative source uniformly distributed in the top 1 m of the model domain.

The transport simulation assumes that contamination with a concentration of 1 $\mathrm{\mu g\,m^{-3}}$ appears (as a

Cl36	50 000 y				100 000 y				200 000 y			
precipitation [mm y^{-1}]	0.3 m	0.5 m	1.0 m	saturated zone	0.3 m	0.5 m	1.0 m	saturated zone	0.3 m	0.5 m	1.0 m	saturated zone
0	1.5E-06	1.6E-06	1.6E-06	1.6E-06	8.3E-07	8.4E-07	8.6E-07	8.8E-07	1.6E-07	1.6E-07	1.6E-07	1.7E-07
20	1.1E-12	8.2E-12	1.1E-09	1.6E-06	6.1E-13	4.5E-12	6.1E-10	8.8E-07	1.2E-13	8.4E-13	1.2E-10	1.7E-07
50	2.0E-13	1.6E-12	2.8E-10	1.6E-06	1.1E-13	8.4E-13	1.5E-10	8.8E-07	2.0E-14	1.6E-13	2.8E-11	1.7E-07
Ca41	50 000 y				100 000 y				200 000 y			
precipitation [mm y^{-1}]	0.3 m	0.5 m	1.0 m	saturated zone	0.3 m	0.5 m	1.0 m	saturated zone	0.3 m	0.5 m	1.0 m	saturated zone
0	8.5E-19	8.6E-19	9.3E-19	1.0E-18	8.5E-19	8.6E-19	9.3E-19	1.0E-18	8.5E-19	8.6E-19	9.3E-19	1.0E-18
20	7.0E-25	5.1E-24	7.0E-22	1.0E-18	7.0E-25	5.1E-24	7.0E-22	1.0E-18	7.0E-25	5.1E-24	7.0E-22	1.0E-18
50	1.2E-25	9.5E-25	1.7E-22	1.0E-18	1.2E-25	9.5E-25	1.7E-22	1.0E-18	1.2E-25	9.5E-25	1.7E-22	1.0E-18
Sn126	50 000 y				100 000 y				200 000 y			
precipitation [mm y^{-1}]	0.3 m	0.5 m	1.0 m	saturated zone	0.3 m	0.5 m	1.0 m	saturated zone	0.3 m	0.5 m	1.0 m	saturated zone
0	9.3E-19	9.3E-19	9.7E-19	1.0E-18	6.9E-18	7.1E-18	7.5E-18	7.9E-18	1.4E-14	1.4E-14	1.4E-14	1.5E-14
20	7.0E-25	5.1E-24	7.0E-22	1.0E-18	5.5E-24	4.0E-23	5.5E-21	7.9E-18	1.0E-20	7.5E-20	1.0E-14	1.5E-14
50	1.2E-25	9.5E-25	1.7E-22	1.0E-18	9.5E-25	7.5E-24	1.3E-21	7.9E-18	1.8E-21	1.4E-20	2.5E-18	1.5E-14
I129	50 000 y				100 000 y				200 000 y			
precipitation [mm y^{-1}]	0.3 m	0.5 m	1.0 m	saturated zone	0.3 m	0.5 m	1.0 m	saturated zone	0.3 m	0.5 m	1.0 m	saturated zone
0	1.6E-05	1.6E-05	1.6E-05	1.5E-05	8.1E-06	8.1E-06	8.1E-06	8.1E-06	1.3E-06	1.3E-06	1.3E-06	1.3E-06
20	1.1E-11	7.8E-11	1.1E-08	1.5E-05	5.6E-12	4.1E-11	5.6E-09	8.1E-06	9.1E-13	6.6E-12	9.1E-10	1.3E-06
50	1.9E-12	1.5E-11	2.6E-09	1.5E-05	9.7E-13	7.7E-12	1.4E-09	8.1E-06	1.6e-13	1.2E-12	2.2E-10	1.3E-06

TABLE 2. Concentrations of ^{36}Cl, ^{41}Ca, ^{126}Sn, ^{129}I in selected simulation times, for various precipitation infiltration amounts in selected depths.

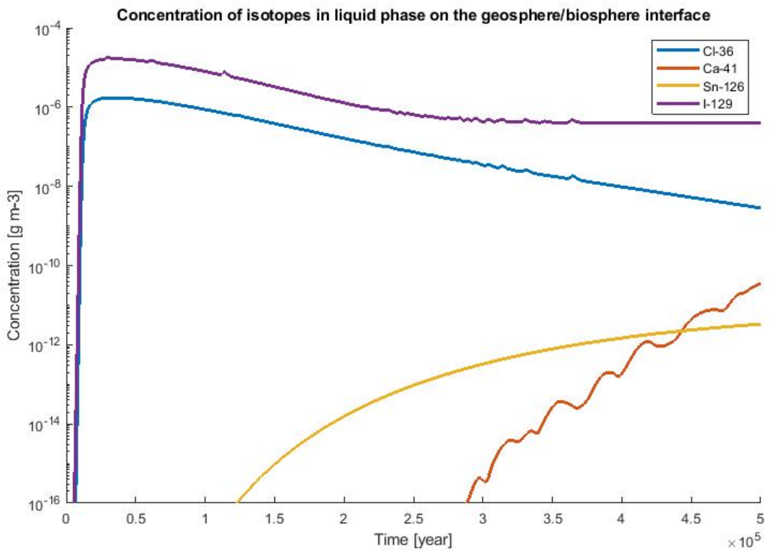

FIGURE 3. Concentration evolutions at the geosphere/biosphere interface used as a boundary condition in the unsaturated zone transport simulations.

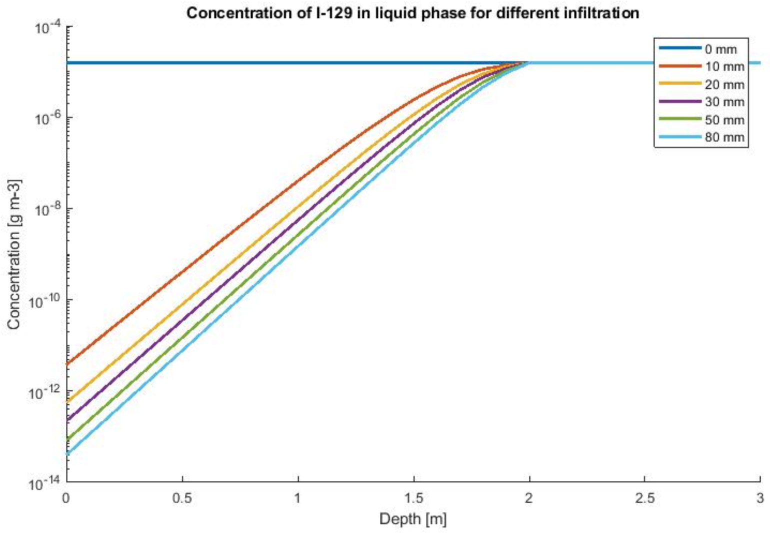

FIGURE 4. Dependence of ^{129}I concentration on depth and infiltration amount at simulation time 50 000 y.

consequence of the flow) in the previously clean saturated portion of the model domain during the first simulation time step. This concentration remains constant throughout the simulation. The simulated tracer is ^{129}I; it is non-sorbing and its decay is negligible (its half-life is much higher than the simulation period).

The simulation period is dictated by the length of the available meteorological data, i.e. 78 965 days (May 1st 1804 to December 31st 2018). The simulation time step was 0.01 days. Figure 6 shows the time evolutions of selected quantities. They capture the first five years of the simulation (the time axis has a MM.YY format). From the results, we can see the initial rapid change to an equilibrium state followed by seasonal oscillations around a mean value. For example, in the case of the concentrations in the 2 m depth (Figure 6c), the oscillation magnitude is about 10 % of the mean, in the 0.5 m depth, it is 18 % and at surface level, (Figure 6d) it is up to 200 %. This significant near-surface concentration uptick happens during summer months when the evaporation rate is higher, which, combined with lower precipitation amounts, leads to higher fluxes from the groundwater level towards the surface. The significantly low values in the summer season are caused by rainstorms. Colder seasons with higher precipitation amounts (usually from October to March) are linked with lower concentrations and oscillations. The concentrations drop by 14-15 orders in the 3 m thick unsaturated zone; from $1 \cdot 10^{-9}$ in the saturated zone to around (depending on time) $6 \cdot 10^{-24}\,\mathrm{kg\,m^{-3}}$ near the surface.

During the simulation of this case study, there were rapid changes of the flow boundary condition (precipitation). This has led to instabilities and non-

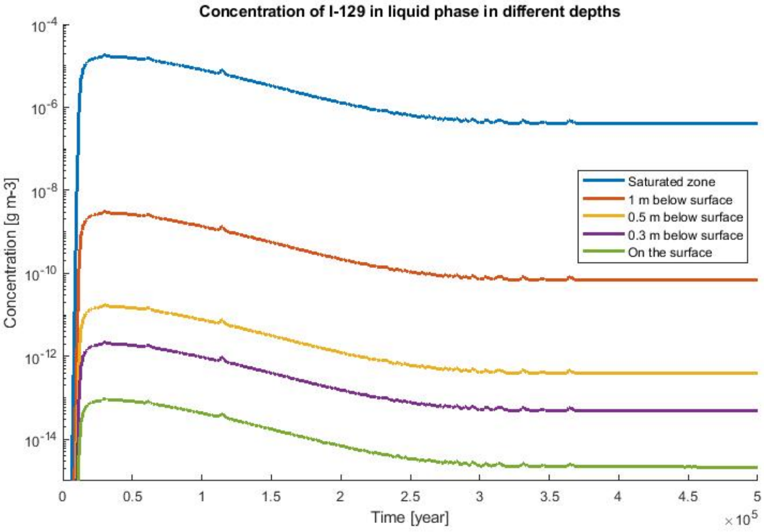

Figure 5. Evolution of ^{129}I concentration at selected depths.

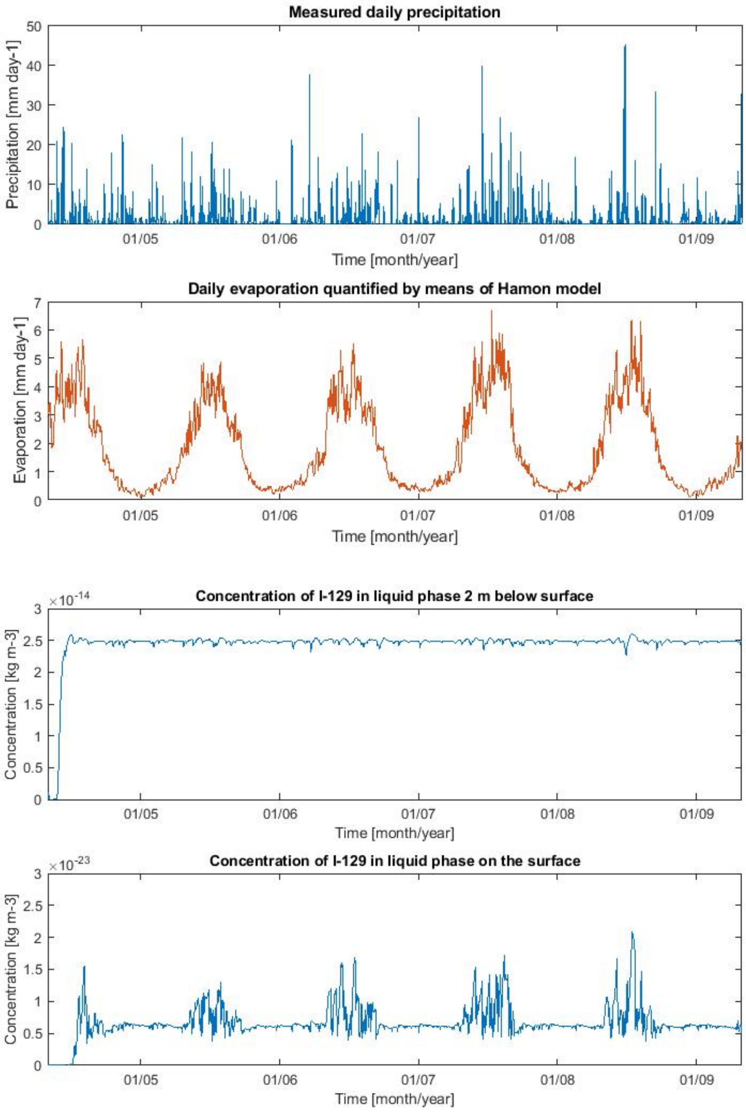

Figure 6. Time evolution of (from top to bottom) a) daily precipitation, b) evaporation, c) concentration 2 m below terrain and d) concentration at terrain level.

physical solutions. The stability was increased by shortening the simulation time step to the final value of 0.01 days. Another way to increase the stability would be to increase the portion of simulation domain in which the evaporation and root withdrawal takes place. The 1 m thickness was used. The third way (not used in this study) would be to average the precipitation/evaporation amounts over a longer time period.

6. CONCLUSION

For a simulation of flow and transport in an unsaturated zone, several concepts and their implementations (both commercial and non-commercial) exist. Despite that (for reasons stated in the introduction), we have decided to implement our own tool simulating the flow using the Richards' equation and transport (advection, diffusion, sorption and radioactive decay) using the advection-diffusion equation. The result is a SW that allows for a simulation of these processes in the unsaturated zone or, to be exact, in the simulation domain that consists of both the saturated and unsaturated zones. This SW was designed and implemented as a part of a more complex system that tracks the radionuclides released from a deep repository through the saturated zone, the unsaturated zone and the biosphere all the way to an individual (in the form of calculated effective dose). We have created a tool for a safety assessment of contamination sources, such as deep repositories of spent nuclear fuel and highly active wastes in a geosphere. Our implementation allowed us to have a precise control over the data exchange between individual models covering portions of the transport path. However, it forced us to deal with potentially unstable states and to verify the model so that we rule out any significant conceptual or implementation errors.

Three case studies were described in this article. They were designed to show the behaviour and results of the model in cases with varying boundary conditions and sources. Such cases are very challenging for existing SW tools used in the field and our ability to solve them is one of the main achievements of the SW concept (and implementation) shown in this article. Simulations with daily changes in precipitation and evaporation proved challenging because they can cause instabilities manifesting as negative concentrations or oscillations (not corresponding to periodicity in inputs). The presented cases prove the solvability of such situations by the presented model implementation as well as its usability within the system for a safety assessment of risks linked to biosphere contamination by radionuclides released from a deep repository. The system could also be used for cases when the contamination source is in the atmosphere and contaminates the environment through fallout and rain water.

ACKNOWLEDGEMENTS

This article was prepared with a support from the Technology Agency of the Czech Republic within the EPSILON program. www.tacr.cz.

REFERENCES

[1] P. O. Johansson. Description of surface hydrology and near-surface hydrogeology at Forsmark. Site descriptive modelling, SDM-Site Forsmark. Tech. Rep. SKB R-08-08, Swedish Nuclear Fuel and Waste Management Co, Stockholm, Sweden, 2008. `https://www.skb.com/publication/1853247/R-08-08.pdf`.

[2] K. Werner, M. Sassner, E. Johansson. Hydrology and near-surfacehydrogeology at Forsmark – synthesis for the SR-PSU project. SR-PSU Biosphere. Tech. Rep. SKB R-13-19, Swedish Nuclear Fuel and Waste Management Co, Stockholm, Sweden, 2013. `https://www.skb.com/publication/2477948/R-13-19.pdf`.

[3] E. Jutebring Sterte, E. Johansson, Y. Sjöberg, et al. Groundwater-surface water interactions across scales in a boreal landscape investigated using a numerical modelling approach. *Journal of Hydrology* **560**:184–201, 2018. `https://doi.org/10.1016/j.jhydrol.2018.03.011`.

[4] P. A. Ekström. Pandora – a simulation tool for safety assessments. Technical description and user's guide. Tech. Rep. SKB R-11-01, Swedish Nuclear Fuel and Waste Management Co, Stockholm, Sweden, 2010. `https://www.skb.com/publication/2188873/R-11-01.pdf`.

[5] C. Yu, E. Gnanapragasam, J.-J. Cheng, et al. User's Manual for RESRAD-OFFSITE Code Version 4. United States Nuclear Regulatory Commission, Argonne National Laboratory, USA, 2020, `https://resrad.evs.anl.gov/docs/RESRAD-OFFSITE_UsersManual.pdf`.

[6] J. Šimůnek, M. Šejna, H. Saito, et al. The Hydrus-1D Software Package for Simulating the Movement of Water, Heat, and Multiple Solutes in Variably Saturated Media, Version 4.17, HYDRUS Software Series 3. Department of Environmental Sciences, University of California Riverside, Riverside, California, USA, 2013, `https://www.pc-progress.com/Downloads/Pgm_hydrus1D/HYDRUS1D-4.17.pdf`.

[7] C. I. Steefel, C. A. J. Appelo, B. Arora, et al. Reactive transport codes for subsurface environmental simulation. *Computational Geosciences* **19**(3):445–478, 2015. `https://doi.org/10.1007/s10596-014-9443-x`.

[8] J. Březina, M. Hokr. Mixed-hybrid formulation of multidimensional fracture flow. In I. Dimov, S. Dimova, N. Kolkovska (eds.), *Numerical Methods and Applications. NMA 2010. Lecture Notes in Computer Science*, vol. 6046. Springer, Berlin, Heidelberg, 2011. `https://doi.org/10.1007/978-3-642-18466-6_14`.

[9] J. Březina, J. Stebel, D. Flanderka, et al. Flow123d, version 2.2.1. User Guide and Input Reference. Technical university of Liberec, Faculty of mechatronics, informatics and interdisciplinary studies, Liberec, 2018, `https://flow.nti.tul.cz/packages/2.2.1_release/flow123d_2.2.1_doc.pdf`.

[10] M. Hokr, H. Shao, W. P. Gardner, et al. Real-case benchmark for flow and tracer transport in the fractured rock. *Environmental Earth Sciences* **75**(18):1273, 2016. `https://doi.org/10.1007/s12665-016-6061-z`.

[11] W. R. Hamon. Estimating potential evapotranspiration. *Journal of the Hydraulics Division* **87**(3):107–120, 1961. `https://doi.org/10.1061/JYCEAJ.0000599`.

[12] T. Vogel, K. Huang, R. Zhang, M. T. van Genuchten. The HYDRUS code for simulating one-dimensional water flow, solute transport, and heat movement in variably-saturated media, Version 5.0. Research Report No 140. U.S. Salinity Laboratory, USDA, ARS, Riverside, CA, 1996.

[13] K. Zhang, Y.-S. Wu, J. E. Houseworth. Sensitivity analysis of hydrological parameters in modeling flow and transport in the unsaturated zone of Yucca Mountain, Nevada, USA. *Hydrogeology Journal* **14**(8):1599–1619, 2006. `https://doi.org/10.1007/s10040-006-0055-y`.

[14] L. A. Richards. Cappillary conduction of liquids through porous mediums. *Physics* **1**(5):318–333, 1931. `https://doi.org/10.1063/1.1745010`.

[15] M. T. van Genuchten. A closed-form equation for predicting the hydraulic conductivity of unsaturated soils. *Soil Science Society of America Journal* **44**(5):892–898, 1980. `https://doi.org/10.2136/sssaj1980.03615995004400050002x`.

[16] M. G. Schaap, F. J. Leij, M. T. van Genuchten. ROSETTA: a computer program for estimating soil hydraulic parameters with hierarchical pedotransfer functions. *Journal of Hydrology* **251**(3-4):163–176, 2001. `https://doi.org/10.1016/S0022-1694(01)00466-8`.

[17] M. A. Celia, E. T. Bouloutas, R. L. Zarba. A general mass-conservative numerical solution for the unsaturated flow equation. *Water Resources Research* **26**(7):1483–1496, 1990. `https://doi.org/10.1029/wr026i007p01483`.

[18] E. Juranová, E. Hanslík, S. Dulanská, et al. Sorption of anthropogenic radionuclides onto river sediments and suspended solids: dependence on sediment composition. *Journal of Radioanalytical and Nuclear Chemistry* **324**(3):983–991, 2020. `https://doi.org/10.1007/s10967-020-07174-w`.

[19] Historical data: Weather: Prague Clementinum. CHMI portal. [2020-11-02], `http://portal.chmi.cz/historicka-data/pocasi/praha-klementinum?l=en#`.

Acta Polytechnica **62**(4):438–444, 2022
`https://doi.org/10.14311/AP.2022.62.0438`

Published by the `Czech Technical University in Prague`

CFD SIMULATION OF PARTIAL CHANNEL BLOCKAGE ON PLATE-TYPE FUEL OF TRIGA-2000 CONVERSION REACTOR CORE

Sukmanto Dibyo[a,*], Wahid Lufthi[a], Surian Pinem[a], Ign Djoko Irianto[a],
Veronica Indriati Sriwardhani[b]

[a] *Center for Nuclear Reactor Technology and Safety – BATAN, Puspiptek, Building No. 80, Tangerang Selatan, Indonesia*

[b] *Center for Applied Nuclear Science and Technology – BATAN, Jln.Tamansari, Bandung, Indonesia*

[*] corresponding author: `sukdibyo@batan.go.id`

Abstract.

A nuclear reactor cooling system that has been operating for a long time can carry some debris into a fuel coolant channel, which can result in a blockage. An in-depth two-dimensional simulation of partial channel blockage can be carried out using FLUENT Code. In this study, a channel blockage simulation is employed to perform a safety analysis for the TRIGA-2000 reactor, which is converted using plate-type fuel. Heat generation on the fuel plate takes place along its axial axis. The modelling of the fuel-plate is in the form of a rectangular sub-channel with an inlet coolant temperature of 308 K with a low coolant velocity of 0.69 m/s. It is assumed that blockage is in a form of a thin plate, with the blockage area being assumed to be 60 %, 70 %, and 80 % at the sub-channel inlet flow. An unblocking condition is also compared with a steady-state calculation that has been done by COOLOD-N2 Code. The results show that a partial blockage has a significant impact on the coolant velocity. When the blockage of 80 % occurs, a maximum coolant temperature locally reaches 413 K. While the saturation temperature is 386 K. From the point of view of the safety aspect, the blockage simulation result for the TRIGA-2000 thermal-hydraulic core design using plate-type fuel shows that a nucleate boiling occurs, which from the safety aspect, could cause damage to the fuel plate.

Keywords: Blockage, FLUENT, plate-type fuel, TRIGA-2000, reactor safety, low coolant velocity.

1. Introduction

TRIGA-2000 is an Indonesian pool-type nuclear research reactor that has been operating for a long time. This reactor uses rod-type fuel produced by General Atomic USA and nowadays, this rod-type fuel is no longer being produced. To maintain the reactor operation, modification of the TRIGA-2000 reactor core using plate-type fuel will be carried out [1–3]. The U_3Si_2Al is used as a fuel material, which is produced domestically, except uranium. This fuel has also been used in the Indonesian RSG-GAS reactor. For this reason, it is presumed that there will not be many changes in core parameters as compared to rod-type fuel. Based on the neutronic calculation, the conversion from rod-type to plate-type shows good results from the safety aspect of a reactor operation. Furthermore, several calculations related to reactor core thermal-hydraulic design have been carried out previously [4–6]. Calculations related to reactor safety analysis, simulations of Loss of Flow Accident (LOFA) and Reactivity Insertion Accident (RIA) have also been carried out [7, 8].

The plate-type fuel element is an arrangement of several fuel plates, which then become a bundle of fuel elements. The fuel plates are arranged in such a way that the gap between each plate can be used as a coolant channel. This plate-type fuel has several advantages over the rod-type fuel, namely its compact structure and high power density [9]. However, the coolant channel between these plates may experience blockage (become clogged) because the coolant channel is quite narrow. Channel blockage causes the heat transfer process to be disrupted so that it has an impact on fuel integrity and reactor safety. Channel blockage conditions can occur due to bending or swelling of fuel plates, caused by other material falling into the reactor pool, or debris carried by the coolant flow [10, 11]. Thus, an analysis of flow channel blockage becomes important for the conversion from rod-type fuel elements to a plate-type fuel assembly. Although the assumed blockage scenario occurs seldomly during the reactor operation.

Simulated blockage scenarios on plate-type fuel by a previous work have been carried out with the IAEA generic 10 MW pool-type benchmark of Material Test Reactor (MTR) [12]. The IAEA Research Reactor is a pool-type MTR, 10 MW. The core is cooled by light water in a forced circulation mode with an average coolant inlet velocity of 3.55 m/s, the operating pressure of 1.7 bar, inlet coolant temperature of 311 K and the core coolant flow direction is downwards [13]. Simulated flow blockage observations using the reactor data have been carried out for one sub-channel with an 80 % blockage ratio and several blockage positions including the inlet, middle, and outlet, in which no boiling occurs in all blockage cases [9].

The main objective of the following study is to perform a safety analysis of a coolant channel partially blocked by debris under steady-state operation, which can cause local heat peaks and ultimately, a loss of fuel integrity. The channel blockage simulation is carried out using FLUENT Code. This analysis is necessary because the thermal-hydraulic design for a fuel-plate type of TRIGA-2000 reactor has a low coolant velocity of 0.69 m/s for cooling the reactor core. The simulation is carried out with the blockage area assumed to be 60 %, 70 %, and 80 % at the inlet of the coolant sub-channel.

The channel blockage analysis using Computational Fluid Dynamics (CFD) simulations has been widely used to investigate fluid dynamics and heat transfer [14, 15]. Meanwhile, one of the main issues in the context of safety assessment of a research reactor plate-type fuel is flow blockages. In a reactor cooling system analysis, the flow phenomena in coolant channels are mostly modelled in Two-Dimensional space (2D), including the possibility of local eddies, which are impossible to observe using one-dimensional simulations. So, CFD modelling is useful to predict the coolant flow temperature and velocity profiles inside a fuel assembly for a blockage state. It can be used to determine the steady-state behaviour on most critical coolant channels. Meanwhile, there are no published experimental data on coolant channel blockage accidents considering heat transfer from the fuel plate to coolant, which is the subject of this simulation.

2. Description of reactor core

TRIGA-2000 is a pool-type research reactor, with a conversion core design consisting of 16 standard fuel elements and 4 control fuel elements as shown in Figure 1.

The reactor core is cooled by light water, forced circulation mode, and downward flow. There are 21 fuel plates in each standard fuel assembly. Coolant sub-channel dimensions of a standard fuel assembly are 67.10 mm in length, 2.557 mm in width, and 625 mm in height. Other parameters related to the fuel elements are given in Table 1. Meanwhile, Table 2 summarizes basic thermal-hydraulic design information of the reactor, in which the reactor power is 1 MW thermal. The power distribution of fuel elements in axial direction was obtained from Batan-Fuel and Batan-3Diff Neutronic Codes that were previously published [3]. A visual representation of the fuel element and its fuel plates arrangements are depicted in Figure 2. Horizontal and cross-section views of the fuel elements are shown in Figure 3. In the fuel element, each plate contains $U_3Si_2{-}Al$ with 19.7 % enriched uranium. Currently, these fuel elements are used in the RSG-GAS reactor at Serpong, Indonesia.

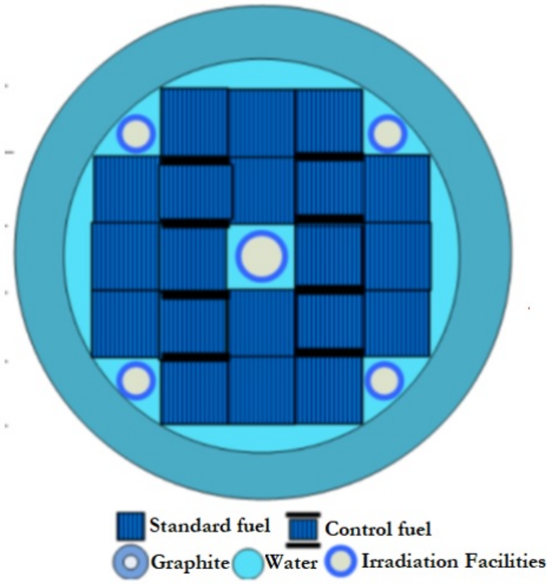

Figure 1. Core configuration [2].

Fuel element parameter	Design values
Number plate in standard fuel element	21
Fuel plate active length, mm	600
Type of fuel element	$U_3Si_2{-}Al$
Width of cooling channel, mm	67.10
Sub-channel gap, mm	2.557
Thickness of cladding, mm (average)	0.38
Cladding material design	$AlMg_2$
Plate thickness fuel, mm	1.30
Width of fuel plates, mm	70.75
Length of fuel plates, mm	625.00

Table 1. Fuel element specification.

Operating Parameters	Value
Fluid material	light water
Coolant mass flow rate to the core, kg/s	50.0
Mass flow rate/fuel element, kg/s	2.10
Average coolant velocity in core, m/s	0.69
Inlet coolant temperature to core, K	308.0
Inlet pressure to core, bar	1.583

Table 2. Input data of coolant operating parameters.

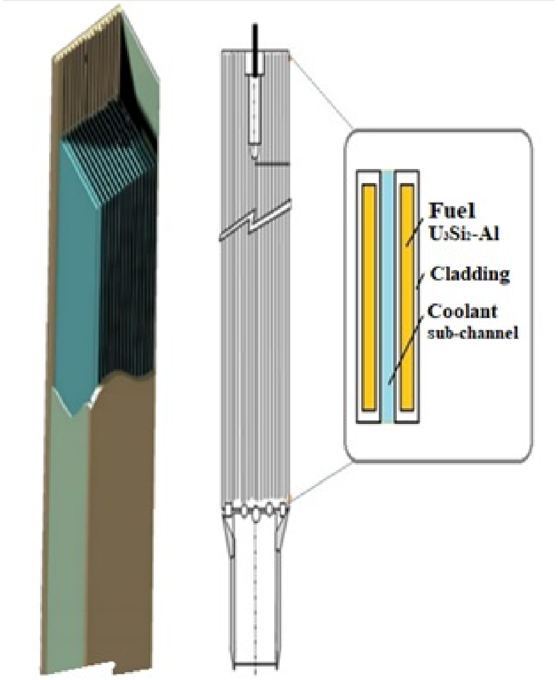

Figure 2. Visual representation of fuel element.

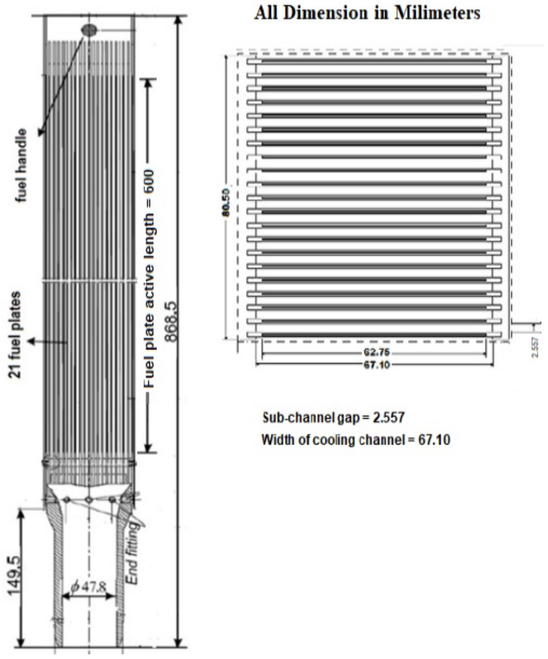

Figure 3. Vertical and horizontal cross-sections of the fuel assembly [16, 17].

3. Methodology

Simplification of the flow blockage case is done by assuming that the flow distribution can affect surrounding channels only by simulating a few sub-channels. This is because parameters from the blocked channel and the adjacent channel will interact and influence each other, especially because the geometry of each fuel plate and coolant channel is similar [9, 10].

Debris can take many forms, either due to material damage or other elements that can be carried away by the coolant flow. Using the CFD method of FLUENT code, any blockage shape can be modelled. In this study, there was no buckling on the fuel plate and the blockage was only caused by the debris. Another assumption is that the blockage only occurs at the inlet channel.

During the blockage scenario, heat generation on the fuel plate takes place along its axial axis with an effective length of 600 mm and a total channel length of 625 mm. The heat transfer received by coolant flow follows equation (1) below:

$$T_{cool}(n+1) = T_{cool}(n) + \frac{Q(n+1)}{m_{cool} \cdot Cp_{cool}} \qquad (1)$$

With $T_{cool}(n)$ being the coolant temperature on n^{th} segment, $Q(n+1)$ being the heat generated by fuel element on $n+1^{th}$ segment, m_{cool} and Cp_{cool} are coolant mass flow rate and specific heat, respectively.

In this simulation, the solution to turbulence flow problem are the assumptions and simplifications that the flow is steady-state, adiabatic, and turbulence *k-epsilon* (k-ε) standard model is set as a boundary condition.

4. Blockage scenarios

In this study, the modelling of the fuel-plate is in the form of a rectangular sub-channel. Due to the presence of blockage, the coolant flow in the blocked sub-channel will be decreased because of the obstruction.

Figure 4 shows a cross-section image of the simulated coolant sub-channel. It is assumed that one of the coolant sub-channels will be blocked by debris. The blockage was simulated as a very thin thickness plate instead of the actual debris. This blockage will cause a reduction in the cross-sectional area of the coolant flow at the inlet of the coolant sub-channel. The sub-channel no. 2 is a sub-channel that will be partially blocked at the top side or inlet stream. In this case, scenarios for the size of the blocked channel area of 60 %, 70 %, and 80 % are determined. These values are based on the study in which it has been investigated by Guo. et al., Salama et al. and Fan et al. [10, 11, 18].

The simulation was performed at a low coolant flow velocity of 0.69 m/s as shown in Table 2. The coolant velocity is an important variable that affects the fuel plate surface temperature. In addition, calculations for sub-channels in normal conditions or 0 % blocked channels were also carried out.

Figure 5 shows schematic steps of activities that include:

(a) data preparation: the design data of TRIGA-2000 conversion using plate-type fuel is used,

(b) steady state calculation without blockage: COOLOD-N2 code is used to validate the steady-state calculation,

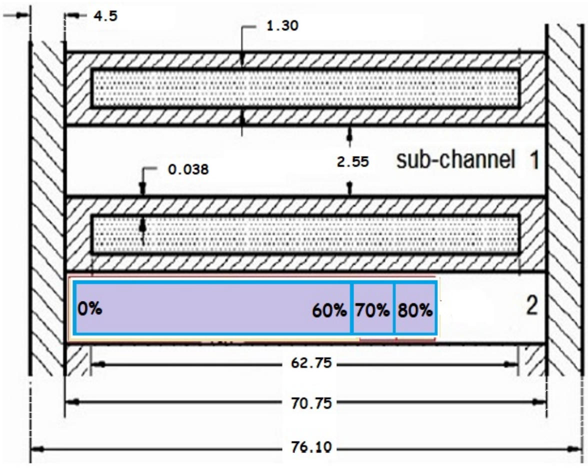

Figure 4. Cross-section view of sub-channel blockage simulation.

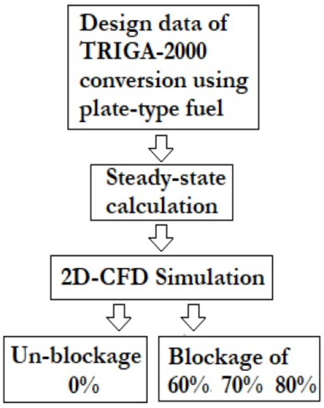

Figure 5. Schematic diagram of simulation.

(c) the partial blockage simulation: 60 %, 70 %, and 80 % flow area.

In this analysis, a CFD method is used, this program helps to solve mathematical equations that formulate the process of fluid dynamics in describing the phenomenon of fluid flow that occurs by making a modelling geometry that matches the actual state of both the shape and dimensions for the simulation. The results obtained in this simulation are in the form of data, images, and curves that show predictions of the system reliability.

5. Results and discussions

Gambit program is used to create geometry, grid, and mesh based on the modelled parts, namely inlet, outlet, and wall as part of the fuel plate. Figure 6 shows a visualization of the mesh from Gambit that will be executed with FLUENT code. One fuel plate with 2 sub-channels is divided into 21 faces in the axial direction, which is the hot surface with axial heat generation flux distribution available from the previous study.

There are no experimental data for the TRIGA conversion core with a plate-type fuel that could be used to validate the results of the steady-state calculation. Therefore, one dimension of the COOLOD-N2 code is used to calculate the steady-state at unblocked conditions. The COOLOD-N2 is a computer code for the analyses of steady-state thermal-hydraulics of both the rod-type and plate-type fuels [19, 20]. In this study, it is assumed that the blocked sub-channel was the hottest channel in the core. As part of a conservative approach, if the hottest channel remains safe, then other channels will also likely be safe.

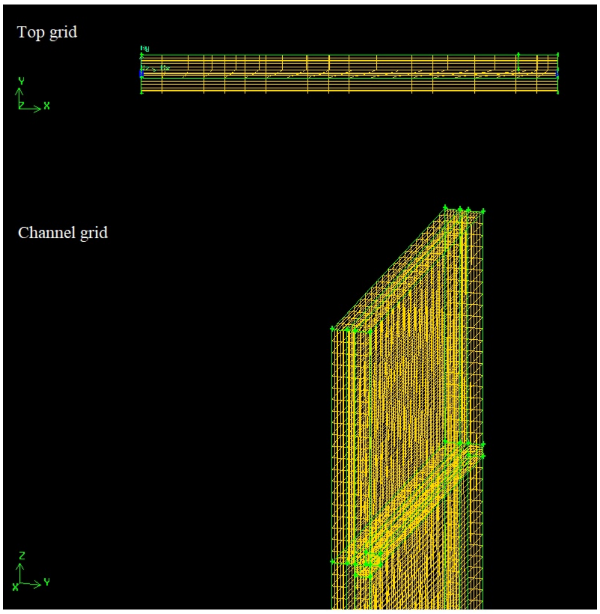

Figure 6. Meshing of channel blockage model.

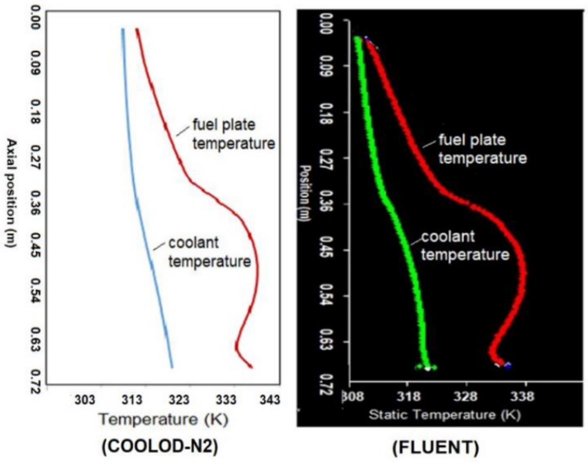

Figure 7. One Dimension fuel plate temperature and coolant temperature for steady state without blockage.

Figure 7 shows the calculated result of the fuel plate surface temperature and coolant temperature by COOLOD-N2 and FLUENT code under normal conditions before the blockage occurs, and there are no significant differences, which gives confidence in the CFD simulation. In this steady-state calculation, a cosine-shape power distribution is utilized in an axial direction. The fuel maximum temperature is around 337 K for these two codes. Meanwhile, the maximum coolant temperature at the outlet channel is around 320 K. The maximum bulk temperature (T_{cool}) occurs at the outlet channel as written in equation (1). Furthermore, the FLUENT model used above can be used for the blocked case to find the temperature profile.

Figure 8 shows calculated results for the profile of the coolant velocity in the blockage area of 0 %, and 60 %. As shown in Figure 8(a), in the case of no blocked channel area, a coolant velocity is 0.69 m/s and the mass flow rate is 0.118 kg/s, which is the uniform velocity distribution at normal conditions. Then, Figure 8(b) shows the profile of flow velocity in the case of blockage of 60 %. When the blockage occurs, a partial blockage in this channel has a significant impact on the flow velocity. Because the inlet are of the coolant sub-channel is reduced to 40 %, the coolant velocity in this inlet sub-channel increases. It can be seen that there is a jet flow with a velocity of up to 1.60 m/s and a mass flow rate of 0.109 kg/s. It has an impact on the coolant velocity along the vertical direction (axial), and there is a localized eddy beneath the blockage plate. Furthermore, the coolant flows vertically, downstream to the outlet channel.

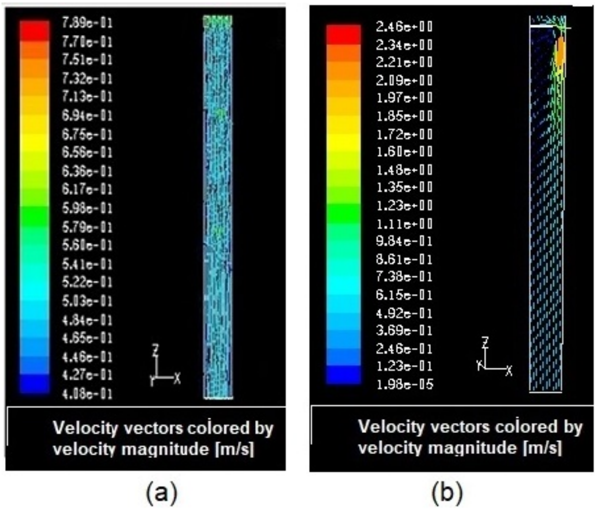

(a) (b)

FIGURE 8. Profile of flow velocity for blockage areas within the range of 0 % and 60 %.

Figure 9(a) and Figure 9(b) show the simulation results for the coolant velocity profile for the blockage areas of 70 % and 80 %. As shown in Figure 8(b), the coolant velocity profile in the coolant channel follows a similar trend. However, the average flow velocity through the narrow channel for 70 %, and 80 % cases is 1.92 m/s and 2.34 m/s, respectively. This flow velocity gradually decreases along the channel's edge. Furthermore, the flow in the middle region appears to be non-homogeneous, and the flow velocity profile is quite complex. The coolant velocity on a fuel plate surface is higher than the velocity on the surface in front of it. The coolant velocity is a variable that significantly influences the fuel plate surface temperature.

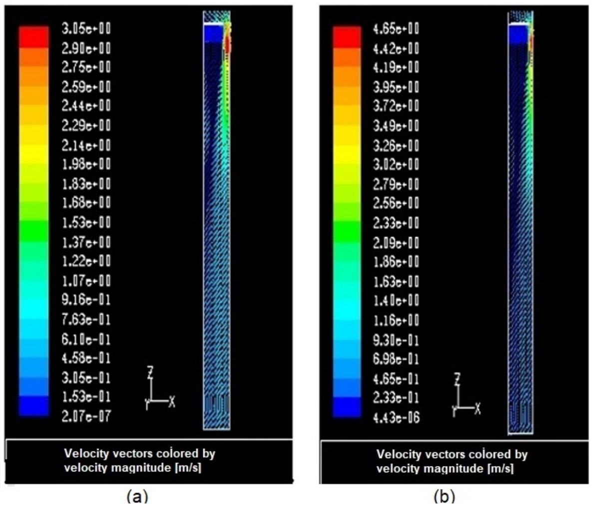

(a) (b)

FIGURE 9. Profile of flow velocity for blockage areas within the range of 70 % and 80 %.

Figure 10(a) and Figure 10(b) depict the static coolant temperature profile of the un-blocked area (0 %) and the blockage of 60 %. A blockage here means a reduction in flow area in the obstructed channel, which could result in a reduction of flow rate. A non-homogeneous flow causes the heat transfer process to not occur properly. The coolant temperature becomes higher than in an unblocked channel. This hot spot temperature also affects the temperature on the opposite plate surface. This effect occurs by the conduction of heat through the thin plate. As depicted in Figure 10(b), it shows that when a channel is obstructed, the coolant temperature profile changes significantly. This simulation indicates that the maximum coolant temperature for the 60 % blockage is 377 K. This temperature is located at 0.52 m from the inlet flow direction. However, it is still below the limit of the coolant saturation temperature, 386 K.

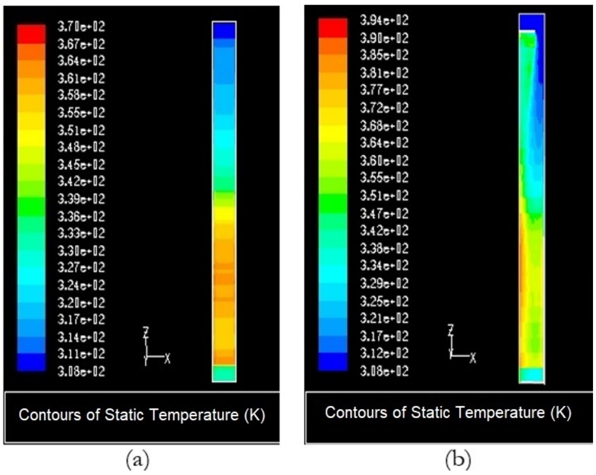

(a) (b)

FIGURE 10. Profile of static temperature for blockage areas within the range of 0 % and 60 %.

Figure 11(a) and Figure 11(b) show that the coolant temperature profile for the 70 % blockage case was similar to the 80 % case. The maximum temperature for the 70 % blockage reached 380 K, which is slightly lower than the saturation temperature of 386 K. While in the case of 80 % blockage, as shown in Figure 11(b), the maximum temperature locally achieves 413 K. It means a nucleate boiling within a liquid may occur in a sub-channel coolant while the bulk fluid flow is sub-cooled, this could cause damage to the fuel plates. Furthermore, the damage to the plate ($AlMg_2$ cladding material) causes a release of fission products from the fuel element into the coolant through the damaged cladding.

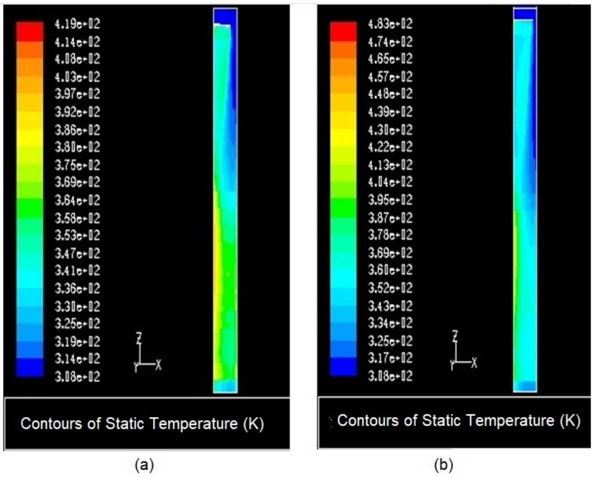

Figure 11. Profile of static temperature for blockage areas within the range of 70 % and 80 %

To ensure reactor safety, nucleate boiling should be avoided in the core, and the coolant should always remain in the super-cooled state, otherwise, it can cause damage to the fuel plate. From the point of view of the safety aspect, the blockage simulation result for TRIGA-2000 thermal-hydraulic core design using plate-type fuel shows a nucleate boiling occurring. It is different with the channel blockage for the reactor of IAEA generic MTR-10MW, in which the IAEA generic reactor has a high coolant flow velocity. There is no boiling occurrence for all blockage cases as can be found in an article published by Q. Lu et al. [12] S. Xia et al. [9].

6. Conclusions

A channel blockage simulation has been carried out using the thermal-hydraulic design for a fuel-plate type of TRIGA-2000 reactor with a low coolant velocity. Under the condition of a 70 % channel blockage, the cooling temperature is still below the nucleate boiling temperature. In the case of the 80 % blockage, a nucleate boiling may occur due to the maximum local temperature reaching 413 K with the saturation temperature being 386 K. This is insufficient for a safety margin and could cause damage to the fuel plate.

Acknowledgements

We would like to acknowledge the INSINAS program of Research and Technology - BRIN 2021 for funding this research, member of "TRIGA plate type fuel design team" and also to all staff of Center for Applied Nuclear Science and Technology – BATAN for supporting the activities.

References

[1] R. Nazar, J. S. Pane, K. Kamajaya. Heat transfer analysis of plate type fuel element of reactor core. *AIP Conference Proceedings* **1984**:020031, 2018. `https://doi.org/10.1063/1.5046615`.

[2] P. Basuki, P. I. Yazid, Z. Suud. Neutronic design of plate type fuel conversion for bandung TRIGA-2000 reactor. *Indonesian Journal of Nuclear Science and Technology* **15**(2):69–80, 2014.

[3] S. Pinem, T. M. Sembiring, T. Surbakti. Core conversion design study of TRIGA Mark 2000 Bandung using MTR plate type fuel element. *International Journal of Nuclear Energy Science and Technology* **12**(3):222–238, 2018. `https://doi.org/10.1504/IJNEST.2018.095689`.

[4] K. A. Sudjatmi, E. P. Hastuti, S. Widodo, N. Reinaldy. Analysis of natural convection in TRIGA reactor core plate types fueled using COOLOD-N2. *Journal of Nuclear Reactor Technology Tri Dasa Mega* **17**(2):67–68, 2015. `https://doi.org/10.17146/tdm.2015.17.2.2317`.

[5] A. I. Ramadhan, A. Suwono, E. Umar, N. P. Tandian. Preliminary study for design core of nuclear research reactor of TRIGA Bandung using fuel element plate MTR. *Engineering Journal* **21**(3):173–181, 2017. `https://doi.org/10.4186/ej.2017.21.3.173`.

[6] V. I. S. Wardhani, J. S. Pane, S. Dibyo. Analysis of coolant flow distribution to the reactor core of modified TRIGA Bandung with plate-type fuel. *Journal of Physics: Conference Series* **1436**:012098, 2020. `https://doi.org/10.1088/1742-6596/1436/1/012098`.

[7] S. Dibyo, K. S. Sudjatmi, S. Sihana, I. D. Irianto. Simulation of modified TRIGA-2000 with plate-type fuel under LOFA using EUREKA2/RR-code. *Atom Indonesia* **44**(1):31–6, 2018. `https://doi.org/10.17146/aij.2018.541`.

[8] S. Pinem, T. Surbakti, I. Kuntoro. Analysis of uncontrolled reactivity insertion transient of TRIGA Mark 2000 Bandung using MTR plate type fuel element. *Ganendra Majalah IPTEK Nuklir* **23**(2), 2020. `https://doi.org/10.17146/gnd.2020.23.2.5876`.

[9] S. Xia, X. Zhou, G. Hu, et al. CFD analysis of the flow blockage in a rectangular fuel assembly of the IAEA 10 MW MTR research reactor. *Nuclear Engineering and Technology* **53**(9):2847–2858, 2021. `https://doi.org/10.1016/j.net.2021.03.028`.

[10] Y. Guo, G. Wang, D. Qian, et al. Accident safety analysis of flow blockage in an assembly in the JRR-3M research reactor using system code RELAP5 and CFD code FLUENT. *Annals of Nuclear Energy* **122**:125–136, 2018. `https://doi.org/10.1016/j.anucene.2018.08.031`.

[11] A. Salama, S. E.-D. El-Morshedy. CFD simulation of flow blockage through a coolant channel of a typical material testing reactor core. *Annals of Nuclear Energy* **41**:26–39, 2012. `https://doi.org/10.1016/j.anucene.2011.09.005`.

[12] Q. Lu, S. Qiu, G. Su. Development of a thermal–hydraulic analysis code for research reactors with plate fuels. *Annals of Nuclear Energy* **36**(4):433–447, 2009. `https://doi.org/10.1016/j.anucene.2008.11.038`.

[13] O. S. AL-Yahia, M. A. Albati, J. Park, et al. Transient thermal hydraulic analysis of the IAEA 10 MW MTR reactor during Loss of Flow Accident to investigate the flow inversion. *Annals of Nuclear Energy* **62**:144–152, 2013. `https://doi.org/10.1016/j.anucene.2013.06.010`.

[14] M. Adorni, A. Bousbia-Salah, T. Hamidouche, et al. Analysis of partial and total flow blockage of a single fuel assembly of an MTR research reactor core. *Annals of Nuclear Energy* **32**(15):1679–1692, 2005. `https://doi.org/10.1016/j.anucene.2005.06.001`.

[15] D. Gong, S. Huang, G. Wang, et al. Heat transfer calculation on plate-type fuel assembly of high flux research reactor. *Science and Technology of Nuclear Installations* **2015**, 2015. `https://doi.org/10.1155/2015/198654`.

[16] PRSG. Reactor. Safety Analysis Report (SAR) of RSG-GAS. Batan-Indonesia. Rev. 9. Chapter 5. 2002.

[17] M. Subekti, D. Isnaini, E. P. Hastuti. The analysis of coolant-velocity distribution in plate-type fuel element using CFD method for RSG-GAS research reactor. *Journal of Nuclear Reactor Technology Tri Dasa Mega* **15**(2):67–76, 2013.

[18] W. Fan, C. Peng, Y. Chen, Y. Guo. A new CFD modeling method for flow blockage accident investigations. *Nuclear Engineering and Design* **303**:31–41, 2016. `https://doi.org/10.1016/j.nucengdes.2016.04.006`.

[19] K. Tiyapun, S. Wetchagarun. Neutronics and thermal hydraulic analysis of TRIGA Mark II reactor using MCNPX and COOLOD-N2 computer code. *Journal of Physics: Conference Series* **860**:012035, 2016. `https://doi.org/10.1088/1742-6596/860/1/012035`.

[20] S. Widodo, E. P. Hastuti, K. A. Sudjatmi, R. Nazar. Steady-state thermal-hydraulic analysis of the TRIGA plate core design by using COOLOD-N2 and RELAP5 codes. *AIP Conference Proceedings* **2180**:020017, 2019. `https://doi.org/10.1063/1.5135526`.

Acta Polytechnica **62**(4):445–450, 2022
`https://doi.org/10.14311/AP.2022.62.0445`

Published by the `Czech Technical University in Prague`

MEASUREMENT OF A QUANTUM PARTICLE POSITION AT TWO DISTANT LOCATIONS: A MODEL

Jaroslav Dittrich

Czech Academy of Sciences, Nuclear Physics Institute, 250 68 Řež, Czech Republic
correspondence: `dittrich@ujf.cas.cz`

Abstract.

A simplified one-dimensional model of measurement of the position of a quantum particle by two distant detectors is considered. Detectors are modelled by quantum particles bounded in potential wells with just two bound states, prepared in the excited states. Their de-excitation due to the short range interaction with the measured particle is the signal for the detection. In the approximations of short time or small coupling between the particle and the measuring apparatuses, the simultaneous detection of the particle by both detectors is suppressed. The results extend to other models with two-level detectors.

Keywords: Position measurement, EPR paradox, quantum measurement.

1. Introduction

The theory of measurement is one of the topics in quantum mechanics from its early days [1]. The development can be found, for example, in reviews [2], [3], [4], [5], [6]. Recently, a comparison of an experimental measurement on a trapped 3-level ion by an interaction with a photon environment with the ideal quantum theoretical measurement was done in [7]. Measurements in quantum field theory with non-relativistic quantum-mechanical detectors coupled to the quantum field were studied in [8].

The famous Einstein-Podolsky-Rosen (EPR) [9] paradox concerns the relation of the measurement results performed on distant parts of a quantum system. Later, the subject evolved to a whole branch of the quantum physics, studies of the quantum entanglements and their applications in quantum informatics (see, e.g., Chapter 16 in [10] for the overview, also extracted in [11], review [12] with an extensive list of references, Chapters 4 and 6 in [13], Chapter 9 in [14], or [15]). For a brief review of the physical background up to 2005 see [16]. Consequences for the black-hole physics are discussed in [17]. Effects in several microscopic and statistical systems were recently studied in [18], [19], [20], [21], [22]. Further possible applications in quantum information are proposed in [23], [24]. The collapse of quantum state due to the measurement was, again, considered in [25], the entanglement in a system chaotic in the classical limit was studied in [26].

Although mostly entanglement of spin states of the two particles is considered, the general idea concerns any simultaneous measurements at distant locations with correlated results. The EPR paradox in the case of a particle position measurement means a simultaneous measurement of the particle presence at two distant places. As the particle can be detected at one place only, a sort of superluminal interaction between the two places seems to be necessary. Another possible interpretation could be that the simultaneous detection at the two places is excluded (or perhaps only strongly suppressed) by the quantum evolution of the *complete* system, consisting of the measured particle and both detectors (and perhaps even their environment), starting from a given initial state. We try to support such an idea by a simple, perhaps not very realistic, model. We obtain suppression of the simultaneous detection at the two places in an approximation but not exactly.

The description of the quantum measurement as the unitary evolution of the complete system was considered already by von Neumann in his classical book [1] (called as process 2 in Section V.1). There exist a number of attempts to model macroscopic measuring apparatuses as quantum objects, let us mention only a sample here. In [1] (Sect. VI.3), [27] (Sect. 139 and Appendix XIV), [28, 29] and essentially also in [30] (Chapter 22), the apparatus is modelled by one very massive body. More close to the quantum description of a macroscopic system are the models of the measuring apparatus as a many-body system, composed of infinite or very large finite number of particles, typically a spin chain - see [31], [32], [33] (Chapter 7).

We consider a rather simple model described in the next section. It consists of a particle interacting with two mutually distant detectors. However, we do not attempt to describe the detector as a macroscopic apparatus. We model it by a single quantum particle bounded in a potential well only.

2. The model

We consider one light particle and two detectors on a line. Each detector consists of a very massive particle bounded in the square potential well of a width $2a$ and depth V_0 tuned to the existence of just two bound states of energies $E_1 > E_0$. The detector is prepared for the measurement in the excited state E_1. The detection of the light particle at the detector is modelled by the passing of the detector to the ground state E_0 due to the interaction with the light particle. This is the determination of the particle position before the measurement as it gains energy $E_1 - E_0$ and is kicked away. The two detectors are located with centres of their potential wells at points $-R$, R with $R \gg a$ (see Figure 1).

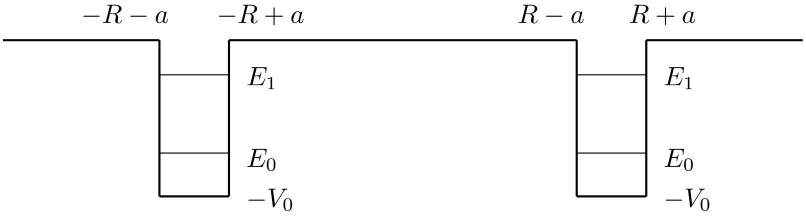

Figure 1. Potential wells of the two detectors. Remember that they bind two different massive particles (it is not a double-well potential but two different one-well potentials).

Let us write the Hamiltonian of the whole three-particle system. Let us denote the potential well

$$V(x) = -V_0\chi_{(-a,a)}(x) = \begin{cases} -V_0 & \text{for} \quad -\mathrm{a} < \mathrm{x} < \mathrm{a} \\ 0 & \text{for} \quad \mathrm{x} \leq -\mathrm{a} \quad \text{or} \quad \mathrm{x} \geq \mathrm{a} \end{cases} , \tag{1}$$

where $\chi_{(-a,a)}$ is the characteristic function of the interval $(-a, a)$ for definiteness although the detailed shape of the potential V is not really used. Denoting $r \in \mathbb{R}$ the coordinate of the measured light particle (mass m), $x \in \mathbb{R}$ the coordinate of the heavy particle in the left detector (mass M) and $y \in \mathbb{R}$ that in the right detector (mass M), the free Hamiltonian (without an interaction of the measured particle and detectors) reads

$$H_0 = -\frac{\hbar^2}{2m}\partial_r^2 - \frac{\hbar^2}{2M}\partial_x^2 + V(x+R) - \frac{\hbar^2}{2M}\partial_y^2 + V(y-R) , \tag{2}$$

understood as a self-adjoint operator in the state space $L^2(\mathbb{R}^3)$ with the domain $H^2(\mathbb{R}^3)$. Let us assume that the measured particle and the particle of the detector interact when their distance is shorter than a with the model interaction Hamiltonian (g is an interaction constant)

$$H_I = g\chi_{(-a,a)}(r-x) + g\chi_{(-a,a)}(r-y) . \tag{3}$$

For simplicity, the interaction potential between the measured particle and the heavy particle in each detector is chosen, again, in the form of a square well (or barrier). Its width $2a$ is chosen the same as for the potentials binding heavy particles in the detectors, which can be interpreted as the detector size (in the order of magnitude, at the least). The complete Hamiltonian

$$H = H_0 + H_I . \tag{4}$$

We assume that the detector with Hamiltonian

$$-\frac{\hbar^2}{2M}\partial_x^2 + V(x) \tag{5}$$

has just two bound states ψ_0, ψ_1 with energies $E_0 < E_1$. The detectors are prepared for measurement in the excited states ψ_1, and the measured particle in a state φ_0 so the initial wave function of the complete system is

$$\Psi(0, r, x, y) = \varphi_0(r)\psi_1(x+R)\psi_1(y-R) . \tag{6}$$

Let us assume that the energy of the light particle is insufficient to release the detector particles from their potential wells and that their states from the continuous spectrum can be neglected in the time evolution. In other words, we assume the wave function of the complete system in the form

$$\begin{aligned}\Psi(t, r, x, y) = {} & c_{00}(t, r)\psi_0(x+R)\psi_0(y-R) + c_{01}(t, r)\psi_0(x+R)\psi_1(y-R) \\ & + c_{10}(t, r)\psi_1(x+R)\psi_0(y-R) + c_{11}(t, r)\psi_1(x+R)\psi_1(y-R) .\end{aligned} \tag{7}$$

Inserting into the Schrödinger equation,

$$i\hbar\partial_t\Psi = H\Psi \ , \tag{8}$$

and projecting onto $\psi_j(x+R)\psi_k(y-R)$ $(j,k = 0,1)$, we obtain

$$\begin{aligned} i\hbar\partial_t c_{jk}(t,r) &= -\frac{\hbar^2}{2m}\partial_r^2 c_{jk}(t,r) + (E_j+E_k)c_{jk}(t,r) \\ &+g\sum_{l=0}^{1}\left(f_{jl}(r+R)c_{lk}(t,r) + f_{kl}(r-R)c_{jl}(t,r)\right) \quad , \end{aligned} \tag{9}$$

where

$$f_{jk}(z) = \int_{z-a}^{z+a} \overline{\psi_j}(x)\psi_k(x)\,dx \tag{10}$$

come from the matrix elements of interaction term H_I (3) and the finite integration range here is a consequence of the finite range of interaction. As eigenfunctions ψ_j are exponentially decaying for $|x| > a$, the same is true for f_{jk} at $|z| > 2a$.

In the matrix notation

$$C(t,r) = \begin{pmatrix} c_{00}(t,r) & c_{01}(t,r) \\ c_{10}(t,r) & c_{11}(t,r) \end{pmatrix} \quad , \quad E = \begin{pmatrix} E_0 & 0 \\ 0 & E_1 \end{pmatrix} \quad , \tag{11}$$

$$F(r) = \begin{pmatrix} f_{00}(r+R) & f_{01}(r+R) \\ f_{10}(r+R) & f_{11}(r+R) \end{pmatrix} \quad , \tag{12}$$

$$G(r) = \begin{pmatrix} f_{00}(r-R) & f_{10}(r-R) \\ f_{01}(r-R) & f_{11}(r-R) \end{pmatrix} \quad , \tag{13}$$

the equations (9) read

$$i\hbar\partial_t C(t,r) = -\frac{\hbar^2}{2m}\partial_r^2 C(t,r) + (E+gF(r))C(t,r) + C(t,r)(E+gG(r)) \ . \tag{14}$$

The initial condition (6) gives

$$C(0,r) = \begin{pmatrix} 0 & 0 \\ 0 & \varphi_0(r) \end{pmatrix} \ . \tag{15}$$

Matrices $F(r)$ and $G(r)$ are Hermitian and bounded in $r \in \mathbb{R}$ according to their construction. So it is easily seen that the operator on the right-hand side of (14) is self-adjoint in $L^2(\mathbb{R},\mathbb{C}^4)$ with the domain $H^2(\mathbb{R},\mathbb{C}^4)$ and the solution $C(t,r)$ exists there for every $C(0,\cdot) \in H^2(\mathbb{R},\mathbb{C}^4)$.

The probability of finding the left detector in the state ψ_j and the right detector in the state ψ_k at the time t is calculated by (7)

$$P_{jk}(t) = \int_{\mathbb{R}} |c_{jk}(t,r)|^2\,dr \quad , \tag{16}$$

i.e., P_{11} is the probability that no detector reacts ($P_{11}(0) = 1$ as detectors are initially prepared in the excited state ψ_1), P_{01} the probability of detection by the left detector only, P_{10} the probability of detection be the right detector only, and P_{00} the probability of simultaneous detection by both detectors.

3. SHORT-TIME EVOLUTION

In the approximation

$$C(t,r) = C(0,r) + t\partial_t C(0,r) + O(t^2) \ , \tag{17}$$

$$\begin{aligned} &C(t,r) = \\ &\begin{pmatrix} 0 & -i\frac{gt}{\hbar}F_{01}(r)\varphi_0(r) \\ -i\frac{gt}{\hbar}G_{10}(r)\varphi_0(r) & i\frac{\hbar t}{2m}\partial_r^2\varphi_0(r) + (1 - i\frac{t}{\hbar}(2E_1 + gF_{11}(r) + gG_{11}(r)))\varphi_0(r) \end{pmatrix}, \end{aligned} \tag{18}$$

assuming at the least that φ_0 belongs to the domain of ∂_r^2. Therefore, the probability $P_{00}(t)$ of the simultaneous detection by the both detectors, indicated by their de-excitations to the ground states, remains zero in the first nontrivial approximation as $t \to 0$,

$$P_{00}(t) = \int_{\mathbb{R}} |c_{00}(t,r)|^2 \, dr = O(t^4) \ , \tag{19}$$

in comparison with the probabilities of detection by just one detector $P_{01}(t)$, $P_{10}(t)$, which are of the order of $O(t^2)$. This is seen from (18), looking by which powers of t the expansions of $c_{jk}(t,r)$ start.

This result is an indication that quantum mechanics inherently prefers the detection of a particle at one place only. However, one should not take it more seriously than the model can approximate macroscopic measuring apparatuses. For the larger times, $P_{00}(t)$ surely is not zero, which also corresponds to the physical picture that the particle interacts with one detector and is bounced to the other.

4. Weak coupling approximation

In this section, we derive a result similar to the one of the previous section but in the first perturbation approximation according to the coupling constant g between the light particle and the measuring instruments. The procedure follows the standard approach of passing to the interaction picture and then iteration of the integral equivalent of the Schrödinger equation.

Let us start from equation (14) and denote as H_m the free Hamiltonian of the light particle, i.e.,

$$H_m = -\frac{\hbar^2}{2m} \partial_r^2 \quad , \tag{20}$$

where the right hand side is understood as the corresponding self-adjoint operator in $L^2(\mathbb{R})$. We transform

$$C(t,r) = \left(e^{-\frac{i}{\hbar}Et} e^{-\frac{i}{\hbar}H_m t} C_1(t,\cdot) e^{-\frac{i}{\hbar}Et} \right)(r) \quad . \tag{21}$$

Here $C_1(t,\cdot)$ denotes the matrix function of r with the value $C_1(t,r)$ at the point r (t is just a parameter). The operator $e^{-\frac{i}{\hbar}H_m t}$ transforms it to another function $C_2(t,\cdot)$, which is then multiplied by two exponentials depending on E and t only. Finally, the value of the resulting function at the point r, i.e., $e^{-\frac{i}{\hbar}Et} C_2(t,r) e^{-\frac{i}{\hbar}Et}$, is taken. A similar notation is used in a few following formulas.

Inserting (21) into (14), we obtain

$$\partial_t C_1(t,r) = -\frac{ig}{\hbar} (A(t) C_1(t,\cdot))(r) \quad , \tag{22}$$

where the operator $A(t)$ acts as

$$A(t)T = e^{\frac{i}{\hbar}H_m t} \left(\tilde{F}(t)(e^{-\frac{i}{\hbar}H_m t} T) + (e^{-\frac{i}{\hbar}H_m t} T)\tilde{G}(t) \right) \tag{23}$$

on a matrix function $T \in L^2(\mathbb{R}, \mathbb{C}^4)$ and $\tilde{F}(t)$, $\tilde{G}(t)$ are multiplications by the matrix functions

$$\tilde{F}(t,r) = e^{\frac{i}{\hbar}Et} F(r) e^{-\frac{i}{\hbar}Et} \quad , \quad \tilde{G}(t,r) = e^{-\frac{i}{\hbar}Et} G(r) e^{\frac{i}{\hbar}Et} \ . \tag{24}$$

The integral form of (22) reads

$$C_1(t,r) = C_1(0,r) - \frac{ig}{\hbar} \int_0^t \left(A(\tau) C_1(\tau,\cdot) \right)(r) \, d\tau \ . \tag{25}$$

Let us iterate this equation starting with $C_1(0,r)$ as the first approximation. Since the operator $A(\tau)$ is uniformly bounded in τ, the resulting perturbation series is convergent to the unique solution.

Keeping only terms linear in g,

$$C_1(t,r) = C_1(0,r) - \frac{ig}{\hbar} \int_0^t \left(A(\tau) C_1(0,\cdot) \right)(r) \, d\tau + O(g^2) \ . \tag{26}$$

The initial value $C_1(0,r) = C(0,r)$ is given in (15) and (26) reads as

$$C_1(t,r) = \begin{pmatrix} 0 & g u_1(t,r) \\ g u_2(t,r) & \varphi_0(r) + g u_3(t,r) \end{pmatrix} + O(g^2) \ , \tag{27}$$

where

$$u_1(t,r) = -\frac{i}{\hbar}\int_0^t \left(e^{\frac{i}{\hbar}(E_0-E_1)\tau} e^{\frac{i}{\hbar}H_m\tau} f_{01}^{(+)} e^{-\frac{i}{\hbar}H_m\tau}\varphi_0\right)(r)\,d\tau \quad , \tag{28}$$

$$u_2(t,r) = -\frac{i}{\hbar}\int_0^t \left(e^{\frac{i}{\hbar}(E_0-E_1)\tau} e^{\frac{i}{\hbar}H_m\tau} f_{01}^{(-)} e^{-\frac{i}{\hbar}H_m\tau}\varphi_0\right)(r)\,d\tau \quad , \tag{29}$$

$$u_3(t,r) = -\frac{i}{\hbar}\int_0^t \left(e^{\frac{i}{\hbar}H_m\tau}(f_{11}^{(+)} + f_{11}^{(-)}) e^{-\frac{i}{\hbar}H_m\tau}\varphi_0\right)(r)\,d\tau \quad , \tag{30}$$

denoting $f_{jk}^{(\pm)}(r) = f_{jk}(r \pm R)$ for $j,k = 0,1$. The free propagator $e^{-\frac{i}{\hbar}H_m\tau}$ can be expressed by the wellknown integral formula here (e.g., Eq. (IX.31) in [34]). Passing back to $C(t,r)$,

$$C(t,r) = \begin{pmatrix} 0 & g e^{-\frac{i}{\hbar}(E_0+E_1)t} e^{-\frac{i}{\hbar}H_m t} u_1 \\ g e^{-\frac{i}{\hbar}(E_0+E_1)t} e^{-\frac{i}{\hbar}H_m t} u_2 & e^{-2\frac{i}{\hbar}E_1 t} e^{-\frac{i}{\hbar}H_m t}(\varphi_0 + g u_3) \end{pmatrix} + O(g^2), \tag{31}$$

and the probability of the simultaneous detection by both detectors remains zero in the first nontrivial approximation as $g \to 0$,

$$P_{00}(t) = O(g^4) \;, \tag{32}$$

in comparison with $P_{01}(t)$ and $P_{10}(t)$ which are of the order of $O(g^2)$.

5. Concluding remarks

The obtained results may be interpreted as a support of the idea that the detection of a particle at one place only is a consequence of the initial conditions for the complete system (particle plus detectors) without any superluminal interaction between two distant places. However, as they are obtained in the approximation of a short time or weak coupling only, it may be questioned whether they do not represent just a kind of initial state stability. A possible objection against this explanation is that C_{00} is more stable than C_{01} and C_{10}.

Another discussible point is the modelling of a macroscopic detector by a single quantum particle. We tacitly assume that the particles in detectors are heavy and thus have a large action. It was used only in heuristic justification of the assumption that their states remains in the two-dimensional subspace spanned by the vectors ψ_0 and ψ_1, in other words, the detectors are essentially two-level systems. The calculation for a more realistic models of the detectors and without approximations of small times or weak coupling would be very desirable but seems to be extremely difficult.

A very specific model was considered for the definiteness but the main results (19) and (32) hold for any detectors modelled as two-level systems and any interaction separated to the sum of two parts corresponding to the particle interaction with each detector instead of (3). The form of the initial particle state φ_0 is also not important here. The specific form of the model is not essentially used in the above calculations. However, the probability P_{00} of a simultaneous de-excitation of both detectors is already nonzero in the next iterations to (19) and (32). So the detection by both detectors is not excluded for large values of t or g in our model.

Acknowledgements

The author is indebted to P. Exner for the comments on the manuscript. The work is supported by the Czech Science Foundation project 21-07129S and NPI CAS institutional support RVO 61389005.

References

[1] J. von Neumann. *Mathematical Foundations of Quantum Mechanics.* Princeton University Press, 2018.

[2] A. A. Clerk, M. H. Devoret, S. M. Girvin, et al. Introduction to quantum noise, measurement, and amplification. *Reviews of Modern Physics* **82**(2):1155–1208, 2010. `https://doi.org/10.1103/RevModPhys.82.1155`.

[3] A. E. Allahverdyan, R. Balian, T. M. Nieuwenhuizen. Understanding quantum measurement from the solution of dynamical models. *Physics Reports* **525**(1):1–166, 2013. `https://doi.org/10.1016/j.physrep.2012.11.001`.

[4] J. Zhang, Y. xi Liu, R.-B. Wu, et al. Quantum feedback: Theory, experiments, and applications. *Physics Reports* **679**:1–60, 2017. `https://doi.org/10.1016/j.physrep.2017.02.003`.

[5] B. d'Espagnat. *Conceptual Foundations of Quantum Mechanics.* CRC Press, Boca Raton, 2nd edn., 2019.

[6] C. Beck. *Local Quantum Measurement and Relativity.* Springer, Cham, 2021. `https://doi.org/10.1007/978-3-030-67533-2`.

[7] F. Pokorny, C. Zhang, G. Higgins, et al. Tracking the dynamics of an ideal quantum measurement. *Physical Review Letters* **124**(8-28):080401, 2020. `https://doi.org/10.1103/PhysRevLett.124.080401`.

[8] J. Polo-Gómez, L. J. Garay, E. Martín-Martínez. A detector-based measurement theory for quantum field theory. *Physical Review D* **105**:065003, 2022. `https://doi.org/10.1103/PhysRevD.105.065003`.

[9] A. Einstein, B. Podolsky, N. Rosen. Can quantum-mechanical description of physical reality be considered complete? *Physical Review* **47**:777–780, 1935. `https://doi.org/10.1103/PhysRev.47.777`.

[10] I. Bengtsson, K. Życzkowski. *Geometry of Quantum States: An Introduction to Quantum Entanglement.* Cambridge University Press, 2017. `https://doi.org/10.1017/9781139207010`.

[11] K. Zyczkowski, I. Bengtsson. An introduction to quantum entanglement: A geometric approach, 2006. `https://doi.org/10.48550/ARXIV.QUANT-PH/0606228`.

[12] N. Friis, G. Vitagliano, M. Malik, M. Huber. Entanglement certification from theory to experiment. *Nature Reviews Physics* **1**:72–87, 2019. `https://doi.org/10.1038/s42254-018-0003-5`.

[13] P. Meystre. *Quantum Optics: Taming the Quantum.* Springer, Cham, 2021. `https://doi.org/10.1007/978-3-030-76183-7`.

[14] D. D'Alessandro. *Introduction to Quantum Control and Dynamics.* CRC Press, Boca Raton, 2021. `https://doi.org/10.1201/9781003051268`.

[15] M. Fadel. *Many-particle entanglement, Einstein-Podolsky-Rosen steering and Bell correlations in Bose-Einstein condensates.* Springer, Cham, 2021. `https://doi.org/10.1007/978-3-030-85472-0`.

[16] M. Kupczynski. Seventy years of the EPR paradox. *AIP Conference Proceedings* **861**:516–523, 2006. `https://doi.org/10.1063/1.2399618`.

[17] L. Susskind. ER=EPR, GHZ, and the consistency of quantum measurements. *Fortschritte der Physik* **64**:72–83, 2016. `https://doi.org/10.1002/prop.201500094`.

[18] W. Zhang, M.-X. Dong, D.-S. Ding, et al. Einstein-Podolsky-Rosen entanglement between separated atomic ensembles. *Physical Review A* **100**(1):012347, 2019. `https://doi.org/10.1103/PhysRevA.100.012347`.

[19] M. Fadel, A. Usui, M. Huber, et al. Entanglement quantification in atomic ensembles. *Physical Review Letters* **127**(1):010401, 2021. `https://doi.org/10.1103/PhysRevLett.127.010401`.

[20] P. Marian, T. A. Marian. Einstein-Podolsky-Rosen uncertainty limits for bipartite multimode states. *Physical Review A* **103**(6):062224, 2021. `https://doi.org/10.1103/PhysRevA.103.062224`.

[21] W. Zhong, D. Zhao, G. Cheng, A. Chen. One-way Einstein–Podolsky–Rosen steering of macroscopic magnons with squeezed light. *Optics Communications* **497**:127138, 2021. `https://doi.org/10.1016/j.optcom.2021.127138`.

[22] K. Berrada, H. Eleuch. Einstein-Podolsky-Rosen steering and nonlocality in quantum dot systems. *Physica E: Low-dimensional Systems and Nanostructures* **126**:114412, 2021. `https://doi.org/10.1016/j.physe.2020.114412`.

[23] Y. Xiang, X. Su, L. Mišta, et al. Multipartite Einstein-Podolsky-Rosen steering sharing with separable states. *Physical Review A* **99**(1):010104, 2019. `https://doi.org/10.1103/PhysRevA.99.010104`.

[24] N. B. An. Quantum dialogue mediated by EPR-type entangled coherent states. *Quantum Information Processing* **20**:100, 2021. `https://doi.org/10.1007/s11128-021-03007-1`.

[25] O. V. Gritsenko. Quantum collapse as reduction from a continuum of conditional amplitudes in an entangled state to a single actualized amplitude in the collapsed state. *Physical Review A* **101**(1):012106, 2020. `https://doi.org/10.1103/PhysRevA.101.012106`.

[26] K. M. Frahm, D. L. Shepelyansky. Chaotic Einstein-Podolsky-Rosen pairs, measurements and time reversal. *The European Physical Journal D* **75**:277, 2021. `https://doi.org/10.1140/epjd/s10053-021-00274-6`.

[27] D. I. Blokhintsev. *Fundamentals of Quantum Mechanics.* Nauka, Moscow, 1976. In Russian.

[28] S. Machida, M. Namiki. Theory of measurement in quantum mechanics I. *Progress of Theoretical Physics* **63**(5):1457–1473, 1980. `https://doi.org/10.1143/PTP.63.1457`.

[29] S. Machida, M. Namiki. Theory of measurement in quantum mechanics II. *Progress of Theoretical Physics* **63**(6):1833–1847, 1980. `https://doi.org/10.1143/PTP.63.1833`.

[30] D. Bohm. *Quantum Theory.* Prentice-Hall, New York, 1952.

[31] K. Hepp. Quantum theory of mesurement and macroscopic observables. *Helvetica Physica Acta* **45**:237–248, 1972. `https://doi.org/10.5169/seals-114381`.

[32] M. Cini, M. De Maria, G. Mattioli, F. Nicolò. Wave packet reduction in quantum mechanics: A model of a measuring apparatus. *Foundations of Physics* **9**:479–500, 1979. `https://doi.org/10.1007/BF00708363`.

[33] P. Bóna. *Classical Systems in Quantum Mechanics.* Springer, Cham, 2020. `https://doi.org/10.1007/978-3-030-45070-0`.

[34] M. Reed, B. Simon. *Methods of Modern Mathematical Physics. II. Fourier Analysis. Self-Adjointness.* Academic Press, San Diego, 1975.

Acta Polytechnica **62**(4):451–458, 2022
https://doi.org/10.14311/AP.2022.62.0451

DETERMINATION OF LOADS ON THE BODY OF A BOXCAR WITH ELASTIC ELEMENTS IN THE CENTER SILL

Oleksij Fomin[a], Glib Vatulia[b], Alyona Lovska[c,*]

[a] *State University of Infrastructure and Technologies, Faculty of infrastructure and rolling stock of railways, Department of Cars and Carriage Facilities, Kyrylivska str., 9, Kyiv, 04071, Ukraine*

[b] *Ukrainian State University of Railway Transport, Faculty of Construction, Department of Structural Mechanics and Hydraulics, Feuerbach sq., 7, Kharkiv, 61050, Ukraine*

[c] *Ukrainian State University of Railway Transport, Faculty of Mechanics and Energy, Department of Wagon Engineering and Product Quality, Feuerbach sq., 7, Kharkiv, 61050, Ukraine*

[*] corresponding author: alyonalovskaya.vagons@gmail.com

Abstract.

The authors suggest elastic elements in the body of a centre sill being the basic carrying element of the frame to decrease the dynamic loads. This solution can transform the dynamic loads on the body into the work of the dry friction forces between the components of the centre sill. The authors substantiated the solution by means of mathematic modelling of the dynamic loads on the body of a boxcar in the vertical plane, including the bouncing oscillations. The differential equations of the motion were solved with the Runge–Kutta method under the zero initial conditions. This solution can decrease the accelerations on the body of a boxcar by about 20 % in comparison to that of the prototype car. The study presents the strength calculations and the design service life for the body of a boxcar. It was calculated that the design service life of a boxcar was longer than that of the prototype car by about 20 %. The research may be used by those who are concerned about higher efficiency of railway transportation.

Keywords: Transport mechanics, boxcar, body, dynamic loading, strength, design service life.

---

1. Introduction

The prospects of transport infrastructure development require a higher operational efficiency of the railway transport as one of the leading industries. Special attention should be paid to the technical maintenance of the rolling stock.

Boxcars are intended for transportation of goods requiring weather protection. As it is known, the most vulnerable element of the body is the frame, due to high dynamic loads occurring during the operation. These cyclic loads decrease the strength of the body of a boxcar. Therefore, it leads to off-schedule repairs or a complete removal of boxcars from the inventory.

And it is of primary importance for the railway transport to introduce an innovative rolling stock. The design of such an innovative vehicle requires an application of new effective solutions aimed at higher fatigue strength, and, therefore, longer design service life. Thus, the appropriate research and data collection in the field should be conducted.

The special features of a static and modal numerical analysis for a boxcar are discussed in study [1]. The strength characteristics are determined by means of FEM.

The authors studied the structural peculiarities of basic boxcar models manufactured in CIS countries in a previous publication [2]. However, the issue of a boxcar with an improved body for lower dynamic loads is not studied.

Aluminium “sandwich” panels, as improvements for the body, are described in [3]. The authors search for an optimal combination of the maximum stresses and displacements. However, the study does not explain the mechanism for a decrease of the dynamic load in a car improved by these panels.

The research into the structural peculiarities of BC-NHL car is given in publication [4]. The article outlines some possible solutions to improve the technical parameters of carbodies. The structural peculiarities of cars intended for combined transportation are studied in [5]. The article gives the strength study for the body of such a car. The design model was built in accordance with the PN-EN standards.

However, these studies have nothing to do with measures to reduce the dynamic loads on the body of cars.

The usage of elastic and viscous elements in the linkage components and the body of rail cars to decrease the dynamic loads during the combined transportation is presented in studies [6, 7]. It was found that flexible links could reduce the dynamic loading of transport facilities by 30 % in comparison with the standard structures.

However, the authors do not study an impact of these elastic and viscous elements in the body of a car on the loading.

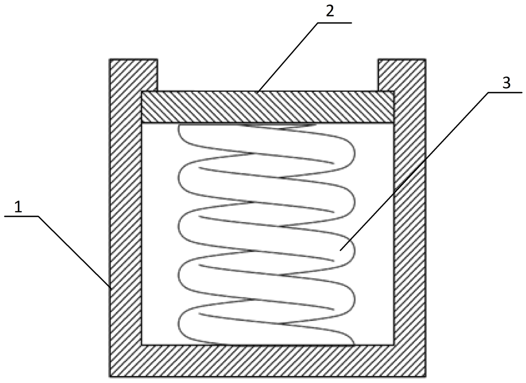

Figure 1. Section of the centre sill of a boxcar, 1 – U-like profile; 2 – horizontal plate; 3 – elastic element.

The literature review made it possible to conclude that at present, the problem of lower loads on the body of a boxcar by means of an application of elastic elements has not been studied. Therefore, there is a need to carry out the appropriate research in the field.

The objective of the research is to ground the application of elastic elements in the body of a boxcar in order to decrease the dynamic loads and prolong the design service life. Research tasks are:

(1.) to offer suggestions for decreasing the dynamic load of a boxcar;

(2.) to make the mathematic modelling of the dynamic load of a boxcar with consideration of these suggestions;

(3.) to research the strength of the body of a boxcar with these suggestions; and

(4.) to determine the design service life of a boxcar taking into account the suggestions offered.

Thus, in order to decrease the dynamic load on the body of a boxcar and increase the fatigue strength during operational modes, the authors suggest elastic elements in the centre sill along the length between the rear supports of the automatic couplers. It can be fulfilled by using the U-like profile for the centre sill, instead of the standard profile (Figure 1).

It is assumed that the decline in the load of the centre sill is achieved due to resistance from the dry friction forces between the vertical planes of the U-like profile and the vertical parts of the horizontal plate during the bouncing oscillations of a car.

This solution was suggested as a concept for substantiation of the elastic friction links in the bearing structure of a car to decrease its dynamic loading in operation. Therefore, this stage did not include the number of elements in the frame, the distance between them, and other parameters.

This solution is patented as a utility model.

The wear of the contacting surfaces can be controlled during the technical maintenance of a car. Sensors can also be used for the diagnosis of the wear of the structural elements.

The worn elastic elements can be replaced through special windows or turnable parts in the frame.

Corrosion can be prevented by means of anticorrosion coatings widely used in machine engineering, particularly, wagon construction.

When applied, the solution proposed can lead to an increase in the tare weight. However, this can be solved by means of materials with a lower weight and high strength values at operational loading for the body components, such as composites. The tare weight can also be decreased by means of optimization of structural elements with reserve strength.

It should be noted that the standard configuration of the centre sill of freight cars is open and generally consists of two Z-profiles. The authors suggest that the open configuration should be used, however it should be covered with a horizontal sheet with elastic elements beneath. Here, the main vertical loading is taken by the horizontal sheet that transfers it to the elastic elements. This loading transfer diagram is used in machine engineering and has proved effective in the spring suspension of bogies, where the bolster beam functions as the horizontal sheet.

The research was made for an 11-217 boxcar. The computer model of the body of a boxcar was designed in the SolidWorks software (Figure 2). The placement of the elastic elements in the centre sill of a car is given in Figure 3.

2. Mathematical modelling of dynamic loading on the bearing structure of a box car

The inertial load on the body of the improved boxcar was defined by means of mathematic modelling. The calculation scheme of the boxcar is given in Figure 4.

This boxcar was considered as a system of four solid bodies: body, two bogies with suspension groups of a certain rigidity and relative friction coefficient and freight. And the elastic elements are components of the bearing structure of a car because they are located in its centre sill. This assumption is reasonable as the elastic elements are used for reducing its dynamic loading; they do not link separate elements of the car body together.

When conducting the research, it was taken into account that the bouncing of bogies is determined by the bouncing of wheel pairs.

Equations (1)–(3) included that:

- $Z_1 \sim q_1$ – coordinate that describes translational displacements of a bogie relative to the vertical axis;
- $Z_2 \sim q_2$ – coordinate that describes translational displacements of the first bogie facing the engine relative to the vertical axis;
- $Z_3 \sim q_3$ – coordinate that describes translational displacements of the second bogie facing the engine relative to the vertical axis;

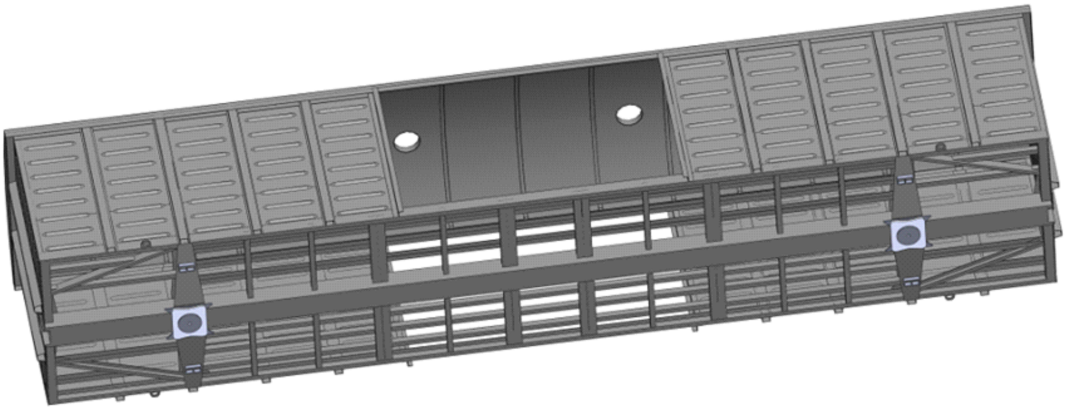

Figure 2. Computer model of the improved body of a boxcar.

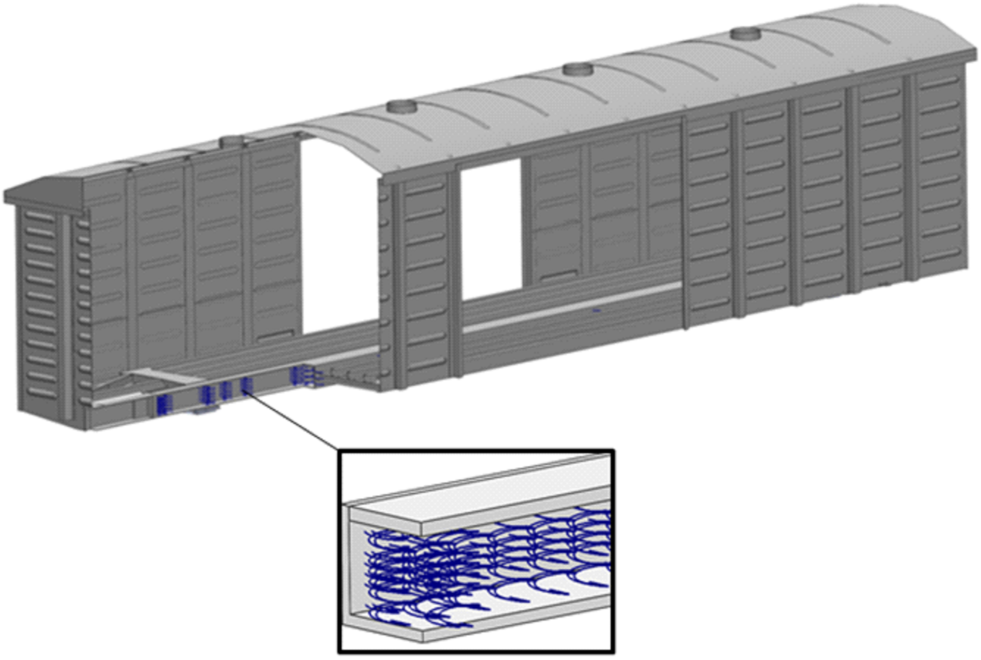

Figure 3. Body of a boxcar with elastic elements in the centre sill.

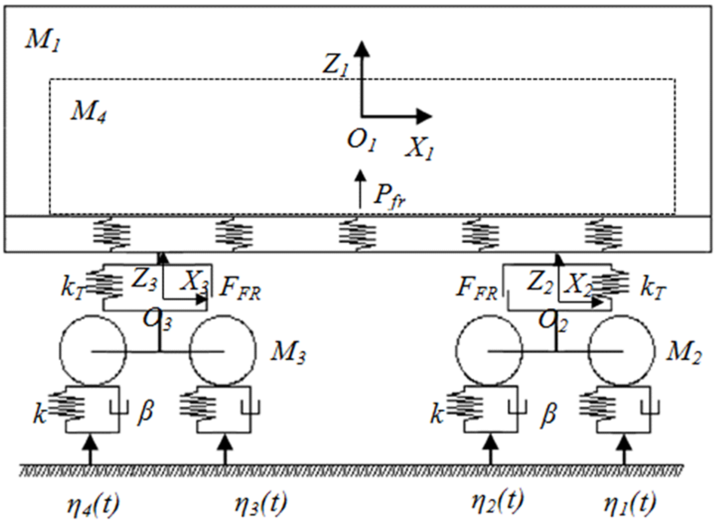

Figure 4. Calculation scheme of a boxcar.

- $Z_4 \sim q_4$ – coordinate that describes translational displacements of the freight relative to the vertical axis.

The study included that the car displacements were described by the equations:

$$M_1 \cdot \frac{\mathrm{d}^2}{\mathrm{d}t^2} q_1 + C_{1,1} \cdot q_1 + C_{1,2} \cdot q_2 + C_{1,3} \cdot q_3 = -F_{FR} \cdot \left(\operatorname{sign}\left(\frac{\mathrm{d}}{\mathrm{d}t}\delta_1\right) + \operatorname{sign}\left(\frac{\mathrm{d}}{\mathrm{d}t}\delta_2\right) \right) - F_z, \quad (1)$$

$$M_2 \cdot \frac{\mathrm{d}^2}{\mathrm{d}t^2} q_2 + C_{2,1} \cdot q_1 + C_{2,2} \cdot q_2 + C_{2,3} \cdot q_3 + B_{2,2} \cdot \frac{\mathrm{d}}{\mathrm{d}t} q_2 = F_{FR} \cdot \operatorname{sign}\left(\frac{\mathrm{d}}{\mathrm{d}t}\delta_1\right) + k(\eta_1 + \eta_2) + \beta\left(\frac{\mathrm{d}}{\mathrm{d}t}\eta_1 + \frac{\mathrm{d}}{\mathrm{d}t}\eta_2\right), \quad (2)$$

$$M_3 \cdot \frac{\mathrm{d}^2}{\mathrm{d}t^2} q_3 + C_{3,1} \cdot q_1 + C_{3,2} \cdot q_2 + C_{3,3} \cdot q_3 + B_{3,3} \cdot \frac{\mathrm{d}}{\mathrm{d}t} q_3 = F_{FR} \cdot \operatorname{sign}\left(\frac{\mathrm{d}}{\mathrm{d}t}\delta_2\right) + k(\eta_3 + \eta_4) + \beta\left(\frac{\mathrm{d}}{\mathrm{d}t}\eta_3 + \frac{\mathrm{d}}{\mathrm{d}t}\eta_4\right), \quad (3)$$

$$M_4 \cdot \ddot{q}_4 = F_z - M_4 \cdot g, \quad (4)$$

$$F_z = -P_{fr} \cdot \operatorname{sign}(\dot{q}_1 - \dot{q}_4) + k_b \cdot (q_1 - q_4), \quad (5)$$

where $M_{i,j}$ – mass and moment of inertia of the oscillation system elements; $C_{i,j}$ – elasticity of the oscillation system components; $B_{i,j}$ – damping coefficients; q_i – coordinates corresponding to translational displacement relative to the vertical axis of the car body, and first and second bogies, respectively; k_T – spring suspension rigidity; k – track rigidity; β – damping coefficient; F_{FR} – absolute friction force in a spring group; δ_i – deformations of elastic elements in a spring suspension; η – track irregularity; k_b – rigidity of the elastic elements in the centre sill; P_{fr} – friction force arising in the centre girder.

The matrix of elastic coefficients has the form:

$$C = \begin{vmatrix} 2k_r & -k_T & -k_T & k_b \\ -k_T & k_T + 2k & 0 & 0 \\ -k_T & 0 & k_T + 2k & 0 \\ k_b & 0 & 0 & 0, \end{vmatrix} \quad (6)$$

It was taken that an empty car passed over a joint irregularity described by periodic function [8]:

$$\eta(t) = \frac{h}{2}(1 - \cos\omega t), \quad (7)$$

where h – irregularity depth; ω – oscillation frequency defined by the formula $\omega = 2\pi V/L$ (V is car speed and L is irregularity length).

The differential equations (1)–(4) were solved in MathCad [9, 10]. The initial conditions are set equal to zero. The calculation results obtained are shown in Figures 5 and 6.

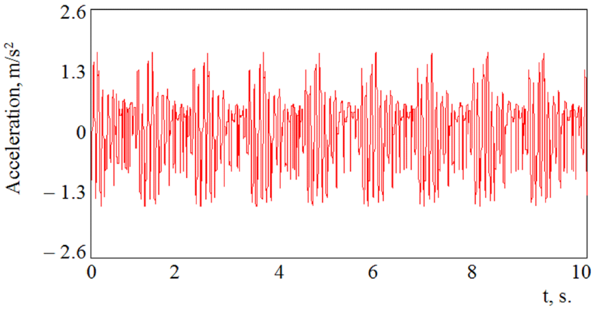

Figure 5. Accelerations on the body of a boxcar in the centre of mass.

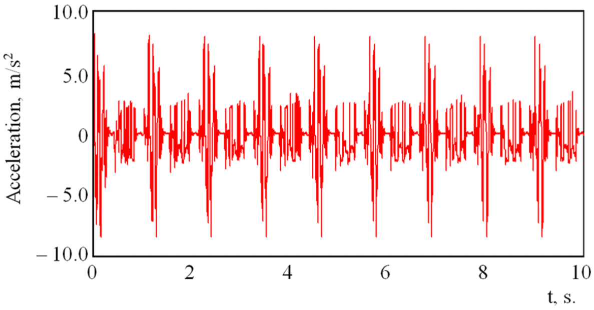

Figure 6. Accelerations of bogies.

The initial parameters presented in Table 1 were included in the calculation.

Parameter	Value
M_1, t	15.3
M_2, M_3, t	4.3
M_4, t	68
k_T, kN/m	8000
k_b, kN/m	8000
P_{fr}, kN	73.6
k, kN/m	100 000
β, kN · s/m	200
h, m	0.01
L, m	3.0
V, km/h	100

Table 1. The initial parameters for determination of the dynamic loading of a boxcar.

The maximum acceleration of the body of an empty boxcar was about 1.43 m/s² (0.15 g), and that of bogies – about 8.2 m/s² (0.8 g). The solution offered can decrease the vertical accelerations on the body of a boxcar by about 20 % in comparison with the standard structure. For a standard boxcar, the acceleration of the bearing structure in the mass centre was 1.9 m/s², and in the support areas on the bogies – 9.7 m/s².

The motion of the car can be estimated as excellent [11–13], and the normative value of the acceleration of the bearing structure in the mass centre is 4.4 m/s².

3. RESULTS OF STRENGTH CALCULATIONS OF THE BEARING STRUCTURE OF A BOX CAR

The strength of the body of a boxcar with elastic elements in the centre sill were defined with FEM in the SolidWorks Simulation software. The continual model of the body of a boxcar is given in Figure 7. Tetrahedrons were taken as the FE. The FEM was built on the basis of these elements as the bogie of the box car was taken as a solid body. We would like to note that the application of such elements gives a good convergence of the computer model and the physical experiment; it was proved by means of the research conducted by the authors regarding similar tasks. The optimal number of FEM elements was determined with the graphical-analytical method.

The number of FE was defined with the graphical-analytical method (Table 2).

Number of elements	234 833
Number of nodes	667 471
Maximal size of an element, mm	100
Minimal size of an element, mm	20
Percentage of elements with a ratio of sides less than three	6.81
Percentage of elements with a ratio of sides more than ten	51.1
Minimal number of elements in a circle	22
The ratio of an increase in the size of an element	1.8

Table 2. Characteristics of the continual model of the body of a boxcar.

Steel 09G2S was applied as the material for the body.

The calculation scheme of the body of a boxcar is given in Figure 8. The calculation scheme included that the body was under vertical load P_v and it was fully loaded with a conditional freight. The vertical loading includes two components: static – 667.08 kN and dynamic – 97.24 kN, which includes the acceleration obtained through the mathematical modelling. The vertical loading was applied to the horizontal surface of the centre sill. The model also included friction forces P_{fr}. The friction force was calculated by means of mathematical modelling in model (1) – (4) and amounted to 73.6 kN. The calculation of the friction force included the condition of the maximum efficiency for the solution proposed regarding the issue of lower dynamic loading.

The model was secured in the areas of support on the running gear parts.

The maximum stresses were found in the contact area between the transverse beam and the centre sill; they accounted for 175.1 MPa (Figure 9), whereas the admissible stress is 295 MPa. The maximum displacements occurred in the middle part of the centre sill; the value measured was 3.3 mm (Figure 10). Thus, the strength of the body of a boxcar was provided [11, 12].

The calculation scheme built (Figure 8) was used for the fatigue research of the body of a boxcar. The authors also found the most loaded zones in the body of a boxcar (Figure 11). These zones included the contact areas between the transverse beam and the center sills. The stress concentration areas for the most loaded zones of the open car frame were determined by means of the maximum equivalent stresses obtained through the Mises criterion with consideration of their cyclic occurrence. The limit stress value is equal to the yield strength of the material – 345 MPa.

The results of the research were used for determination of the biaxiality ratio of the body of a boxcar (Figure 12). This ratio characterizes a relationship between the minimum and maximum stresses occurring in the body of a boxcar. The design service life of a boxcar was defined according to the method presented in [14]:

$$T_p = \frac{(\sigma_{-1L}/[n])^m \cdot N_0}{B \cdot f_e \cdot \sigma_{ad}^m}, \tag{8}$$

where σ_{-1L} – endurance limit; n – allowable strength factor; m – fatigue curve exponent; N_0 – test base; B – coefficient that determines permanent work in seconds; f_e – efficient frequency of dynamic stresses; σ_{ad} – amplitude of dynamic stresses.

The amplitude of dynamic stresses is

$$\sigma_{ad} = \sigma_{sw}(k_{vd} + \psi_\sigma/K_\sigma), \tag{9}$$

where σ_{sw} – stresses caused by the static weight load; k_{vd} – vertical dynamics coefficient; ψ_σ – sensitivity coefficient; K_σ – overall fatigue strength reduction coefficient.

The calculation included the following input parameters: $\sigma_{-1L} = 245$ MPa; $n = 2$; $m = 8$; $N_0 = 10^7$; $B = 3.07 \times 10^6$ s; $f_e = 2.7$ Hz; $\sigma_{sw} = 142.4$ MPa; $k_v d = 0.35$; $\psi_\sigma/K_\sigma = 0.2$.

The calculation demonstrates that the design service life of the proposed body is about 40 years. Therefore, the value of the design service life obtained is about 20 % higher than the service life of a standard boxcar frame with a centre sill consisting of two Z-profiles. It should be noted that the service life obtained should be adjusted through both further research into the longitudinal loading on the body of a boxcar and experiments.

It should be noted that the fatigue of elastic elements was not included in the calculation of the service life of a boxcar, as this element can be replaced by a new one, if needed.

4. CONCLUSIONS

(1.) The authors suggested elastic elements in the centre sill being the basic carrying element of the

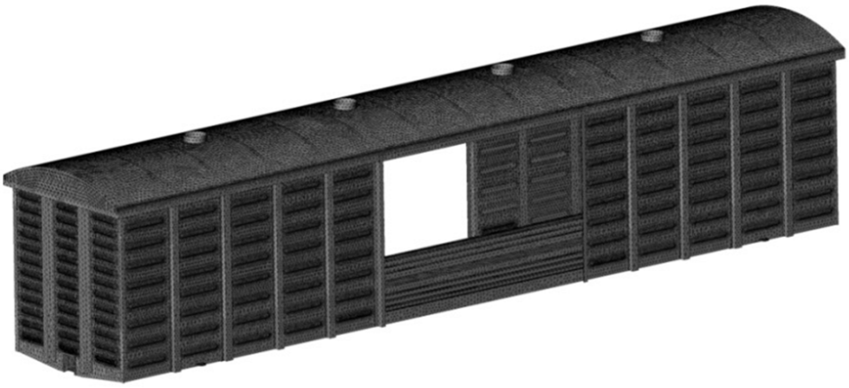

Figure 7. Continual model of the body of a boxcar.

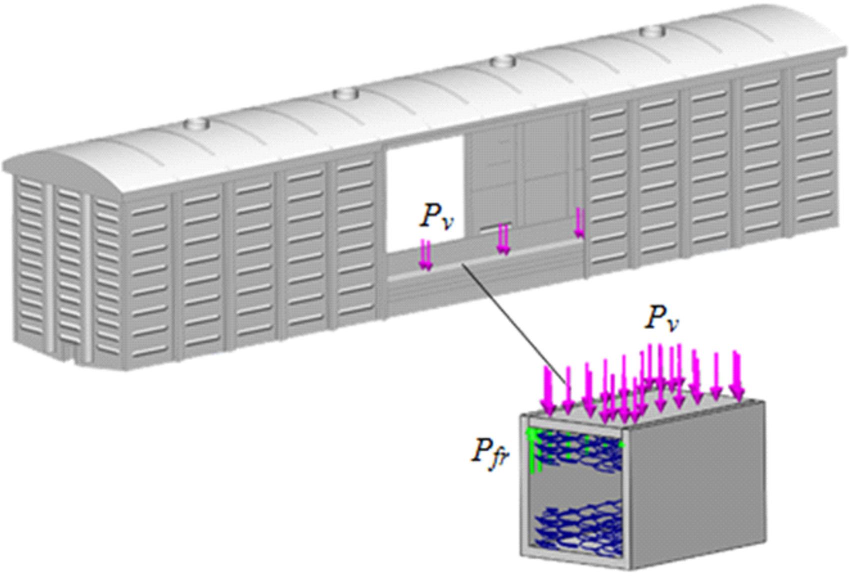

Figure 8. Calculation scheme of the body of a boxcar.

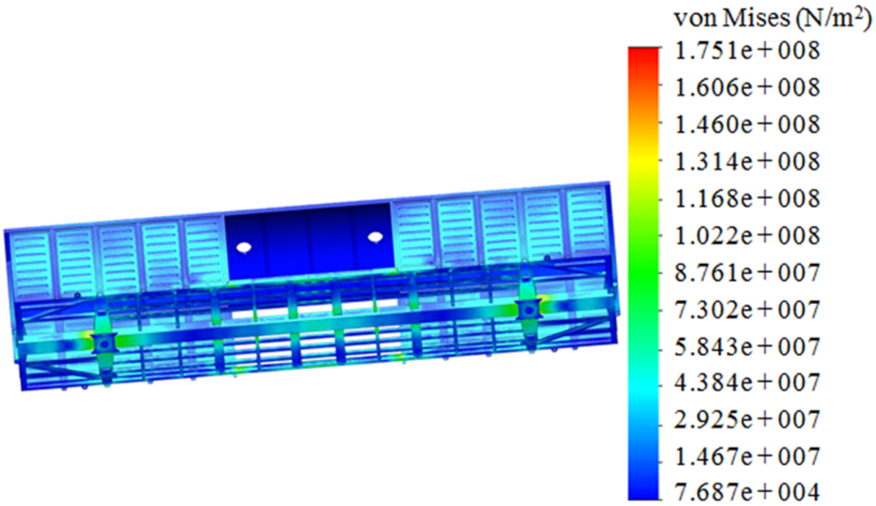

Figure 9. Stress of the body of a boxcar.

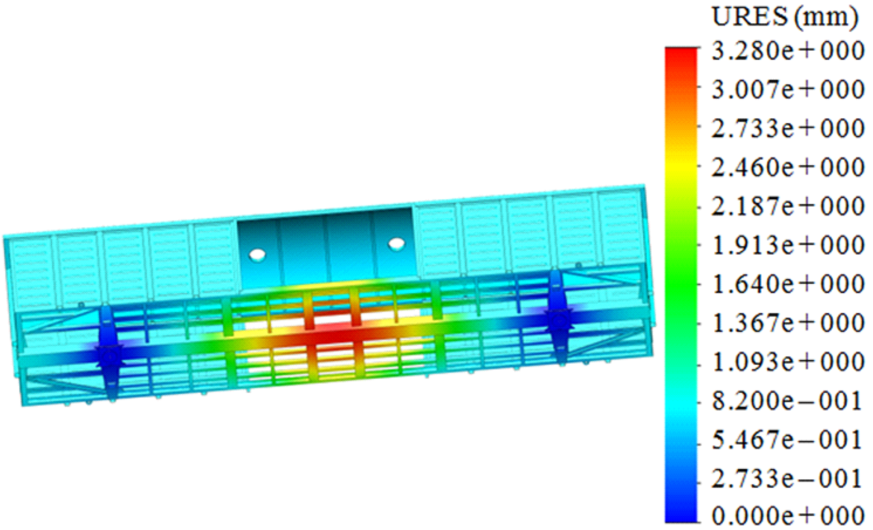

Figure 10. Displacements in the body of a boxcar.

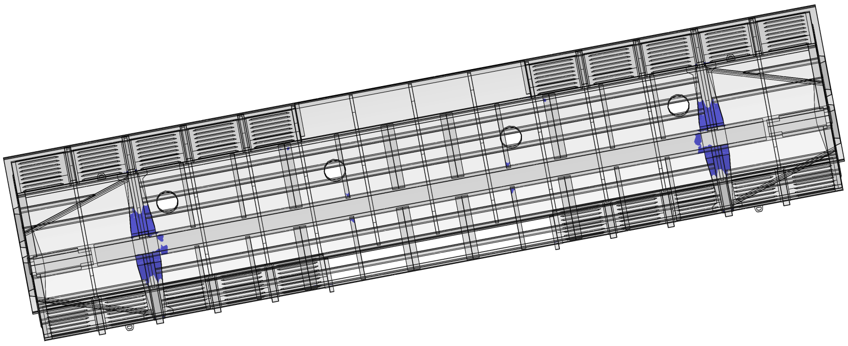

Figure 11. Most loaded zones in the body of a boxcar.

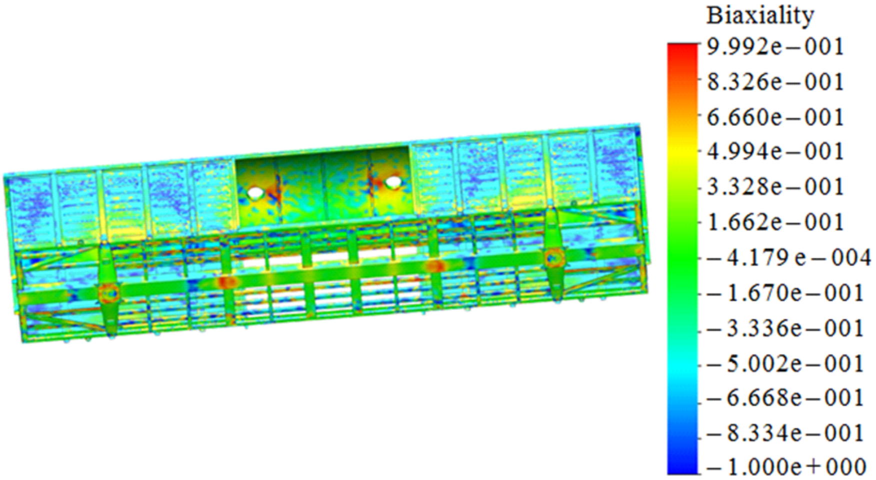

Figure 12. Biaxiality ratio in the body of a boxcar

frame. This solution can transform the loads on the body into the work of the dry friction forces between the components of the centre sill.

(2.) The research deals with the modelling of loads on the improved boxcar. The maximum acceleration of the body of an empty boxcar was $1.43\,\mathrm{m/s^2}$ ($0.15\,\mathrm{g}$), and that of bogies was $8.3\,\mathrm{m/s^2}$ ($0.8\,\mathrm{g}$). This solution can decrease the accelerations on the body of a boxcar by about 20 % in comparison to those of the prototype car. The motion of the car can be estimated as excellent.

(3.) The authors determined the basic strength characteristics of the body of a boxcar with consideration of the solution proposed. The calculation was made with FEM in the SolidWorks Simulation software. The greatest stresses occurred in the contact area between the bolster beam and the centre sill with a value of 175.1 MPa. The maximum displacements occurred in the middle of the centre sill and were equal to 3.3 mm. Thus, the strength of the body of a boxcar was provided.

(4.) The design service life of the improved boxcar was calculated as 40 years. Thus, the design service life obtained was 20 % longer than that of the prototype car. The research may be of value for those who are concerned about a more efficient operation of railway transport.

ACKNOWLEDGEMENTS

This study was conducted within the framework of the scientific theme of young scientists “Innovative approaches in designing resource-saving car structures with consideration of refined dynamic loading and functional-adaptive flash-concepts”, which is funded by the State budget of Ukraine in 2020.

REFERENCES

[1] S. Sepe, A. Pozzi. Static and modal numerical analyses for the roof structure of a railway freight refrigerated car. *Frattura ed Integrità Strutturale* **9**(33):451–462, 2015. `https://doi.org/10.3221/IGF-ESIS.33.50`.

[2] S. V. Myamlin, N. G. Murashova, I. Y. Kebal, A. Z. Kazhkenov. Sovershenstvovanie konstrukczii krytykh vagonov. *Vagonnij park* **7-8**(100-101):4–8, 2015.

[3] H.-A. Lee, S.-B. Jung, H.-H. Jang, et al. Structural-optimization-based design process for the body of a railway vehicle made from extruded aluminum panels. *Journal of Rail and Rapid Transit* **230**(4):1283–1296, 2015. `https://doi.org/10.1177/0954409715593971`.

[4] C. P. Shukla, P. K. Bharti. Study and analysis of doors of BCNHL wagons. *International Journal of Engineering Research & Technology (IJERT)* **4**(4):1195–1200, 2015. `https://doi.org/10.17577/IJERTV4IS041031`.

[5] W. Krason, T. Niezgoda. FE numerical tests of railway wagon for intermodal transport according to PN-EU standards. *Bulletin of the Polish Academy of Sciences technical sciences* **62**(4):843–851, 2014. `https://doi.org/10.2478/bpasts-2014-0093`.

[6] O. Fomin, A. Lovska, V. Radkevych, et al. The dynamic loading analysis of containers placed on a flat wagon during shunting collisions. *ARPN Journal of Engineering and Applied Sciences* **14**(21):3747–3752, 2019.

[7] A. Lovska, O. Fomin, P. Kučera, V. Píštěk. Calculation of loads on carrying structures of articulated circular-tube wagons equipped with new draft gear concepts. *Applied Sciences* **10**(21):7441, 2020. `https://doi.org/10.3390/app10217441`.

[8] Y. V. Domin, G. Y. Chernyak. *Osnovi dinamiki vagoniv.* KUETT, Kiyiv, 2003.

[9] D. V. Kir’yanov. *Mathcad 13.* BHV, Peterburg, 2006.

[10] V. D’yakonov. *Mathcad 8/2000: special’nyj spravochnik.* Piter, 2000.

[11] DSTU 7598:2014. Freight wagons. General requirements for calculations and design of new and modernized carriages of 1520 mm gauge (non-self-propelled). 2015.

[12] GOST 33211-2014. Freight wagons. Requirements for strength and dynamic properties. 2016.

[13] Norms for the calculation and designing of railway cars of the IGS track 1520 mm (non-self-propelled). GosNIIV. VNIIZhT, 319, 1996.

[14] P. A. Ustich, V. A. Karpych, M. N. Ovechnikov. *Nadezhnost relsovogo netyagovogo podvizhnogo sostava.* Transport, Moskva, 1999.

Acta Polytechnica **62**(4):459–472, 2022
`https://doi.org/10.14311/AP.2022.62.0459`

FUNCTIONAL AERODYNAMICS AND ITS INFLUENCE ON THE ENERGY AND THERMAL MODE OF A NATURALLY VENTILATED DOUBLE-SKIN TRANSPARENT FAÇADE

Michal Franek[a,*], Boris Bielek[a], Marek Macák[b], Josip Klem[a]

[a] *Slovak University of Technology in Bratislava, Faculty of Civil Engineering, Department of Building Structures, Radlinského 2766/11, 810 05 Bratislava, Slovakia*

[b] *Slovak University of Technology in Bratislava, Faculty of Civil Engineering, Department of Mathematics and Descriptive Geometry, Radlinského 2766/11, 810 05 Bratislava, Slovakia*

[*] corresponding author: `michal.franek@stuba.sk`

Abstract. This article deals with the dynamics of airflow through a cavity. In windless conditions, where a natural flow causes the flow of air in the cavity, the overall aerodynamic resistance of the cavity is the important aerodynamic parameter, which is the sum of the local resistances alongside the air movement trajectory through the cavity. The total aerodynamic resistance of the cavity must be lesses than the force of the convective buoyancy of the air in the cavity. The following conclusions were found experimentally. The convection occurs in the cavity at every time step with a velocity range from $0.05 \leq v$ [m/s] ≤ 0.2 to 0.3. The energy regime in the cavity is characterised by inhomogeneity. In the cavity, there are zones of increasing temperatures along the height of the cavity at the inlet. A large area with increased temperatures at the air outlet and a small area with particularly high temperatures in the upper part of the inlet were found.

Keywords: double-skin transparent façade, energy and thermal mode, aerodynamic resistance of the cavity, total pressure coefficient.

1. List of Acronyms

BLWT	Boundary Layer Wind Tunnel
CFD	Computational Fluid Dynamics
DNS	Direct Numerical Simulation
DSTF	Double-Skin Transparent Façade
LES	Large Eddy Simulation
N-S	Navier-Stokes
RANS	Reynolds Averaged Navier-Stokes Equations
SRS	Scale-Resolving Simulation
NBS	National Bank of Slovakia

2. Introduction

There are many factors that affect the technology of construction of façades, such as architectural trends, technology itself, and public requests. Today, the importance of environment specific contexts is as important as public requests for the quality of work. Current modern trends, such as ecology, energy-saving, automatic control systems, have not been addressed by façade technology, which also uses ecological renewable energy sources, which follow the concept of ecological improvement in the European construction industry. One of the most environmentally friendly alternative sources of solar energy is the double-skinned transparent façade (DSTF), the concept of which is not new, but the trend of constructing buildings with DSTF has only recently been growing, mostly in Europe because of high energy costs and ecological awareness.

The originality in the creation of a new façade technology is characterised by four aspects:

- theory of the creation of new façade technology is designated for intelligent buildings,
- façade elements have the character of items of circuits of automated systems of building control,
- façade elements or systems have the ability to utilise natural physical phenomena,
- façade elements or systems have the ability to dynamically reduce the required volume of the environment technology of the building [1].

Considering the technical aspect, the development of a double-skin transparent façade has its foundations in the physical theory of cavities, which allows various adjustments, e.g., in the geometry of the cavity or in the type of glazing used. The theory of natural physical cavities has its roots in the development of recent technical disciplines, which are solar heat technology and aerodynamics of buildings with their substantial activity in the field of the physics of buildings and constructions. Cavity theory quantifies their physical behaviour, called multi-skin structures, and has been a topic discussed by many authors. There are many ways to design DSTF and predict its behaviour, such as models for predicting the airflow or temperature inside a cavity. Underestimating the systems and components of the DSTF as a whole can result in major errors that significantly affect its operation. We can find proof of this in existing buildings, which have these problems [2], [3].

Todorovic et al. [2] developed a computational model usable in the climatic environment of Central Europe that approximates the temperature of the air and the heating (cooling) load in the DSTF cavity every hour. Arons [3] used a numerical model for a calculation of energy performance of a typical DSTF. In 2001, Gan [4] used a model for calculating the thermal transmittance of multiple glazing based on computational fluid dynamics (CFD), and in experimental cases, Saelens et al. [5] introduced a numerical model for calculating the thermal power of active envelopes. Later, Hensen et al. [6] used a network to calculate the characteristics of the air inside the DSTF cavity and included it in the thermal and energy model of the building. A model for single-storey buildings was presented by Saelens [7], he created a computational algorithm for two dimensional double-skin façades with both mechanical and natural ventilation. In Belgium, Gratia et al. [8] developed a model for thermal efficiency and cooling (heating) load according to the season. Grabe [9] developed a practice for modelling the temperature and air behaviour in DSTF. More modern works include computational fluid dynamics models, which can calculate airflow in DSTF cavity more accurately as compared to abovementioned models [10], [11], [12]. Manz et al. [13] used an algorithm to calculate the heat transfer from a natural convection in DSTF. The CFD method can offer much more detailed results especially for airflow through shading devices, recirculation zones or when the wind profile is irregular [13], [14], [15]. A brief document was issued in 2007 by the Commission of the European Council [16] with guiding principles for the construction of DSTF.

In the case of double-skin transparent façades using an alternative source of solar energy, the transformation of short-wave solar radiation into long-wave heat radiation is a natural physical phenomenon [17], [18]. The exploitation of this physical phenomenon with contribution of quantified dynamics of air flows is conditioned by the development of the theory of physical cavities.

The double-skin transparent façade participates in energy conservation of buildings in winter periods by its energy, which is gained from renewable energy sources – solar radiation and also by the transformation of solar radiation into heat radiation in the cavity of the façade. Well-designed aerodynamics of cavity can also meaningfully decrease the heat load of a building in summer seasons [19]. The double-skin transparent façade offers the possibility of natural ventilation, which is directly connected to the outside climate. At the same time, it delivers a new quality of psycho-physiological comfort in the working space. It is characterised by a better connection of an artificial architectural environment with nature.

The main objective of this article is the new façade technology for buildings, that is the double-skin transparent façade in Figure 1.

The methodology of the paper is a theoretical analysis based on scientific disciplines and in-situ measurement:

- building solar thermal technology in a more complex perception, including the input of solar radiance,
- aerodynamics of buildings in „a more complex perception than that represented by a rigid model“ with an external pressure coefficient c_{pe} (-), quantified by an aerodynamic coefficient of overall pressure $c_{\mathrm{p}} = c_{\mathrm{pe}} - c_{\mathrm{pi}}$ (-), in which the knowledge of the aerodynamic coefficient of internal pressure c_{pi} (-) substitutes for the imperfection of a rigid model,
- aerodynamics of a cavity, quantified by the overall aerodynamic resistance of the cavity Z, which is the sum of the friction resistances and local resistances lengthways to the flow trajectory in the cavity.

3. Theoretical background

The physical theory of cavities is the base idea of the double-skin transparent façade. The paper deals with a naturally ventilated double-skin transparent façade with a corridor-type cavity (cavity width $0.5 \leq b \leq 1.5\,\mathrm{m}$) and open circuit (the whole volume of air entering the cavity is air flowing from the outdoor climate, also, the entire volume of air through the cavity is conducted to the outdoor climate) in Figure 2.

A general correlation of the temperature in the cavity (Figure 2) is visible if the external air enters the cavity:

$$\theta_{a,OUTLET} - \theta_{a,INLET} = \theta_{a,OUTLET} - \theta_{ae} = \frac{\tau_g \cdot I_m}{mean\,U_m}\left(1 - e^{-\frac{mean\,U_m \cdot L}{q_m \cdot c}H}\right), \quad (1)$$

where $\theta_{a,OUTLET}$ is the air temperature from the outlet of the cavity [°C], $\theta_{a,INLET}$ is the air temperature from the inlet of the cavity [°C], τ_g is the the overall transmission coefficient of the glazed system of the front – outer transparent wall [-], I_m is the mean intensity of global solar irradiation on the outer vertical transparent wall [W/m^2], $mean\,U_m$ is the mean heat transfer coefficient of the bounding structures of the cavity $[\mathrm{W/(m^2 \cdot K)}]$, L is the length (horizontal) of the cavity division [m], q_m is the mass air flow rate through the cavity [kg/s], H is the height of the cavity [m], c is the mass heat capacity of the air $[\mathrm{J/(kg \cdot K)}]$. The energy regime of these cavities depends on the air flow rate q_m [kg/s], q_V [m^3/s], which is determined by the dynamics of the air flowing through the cavity

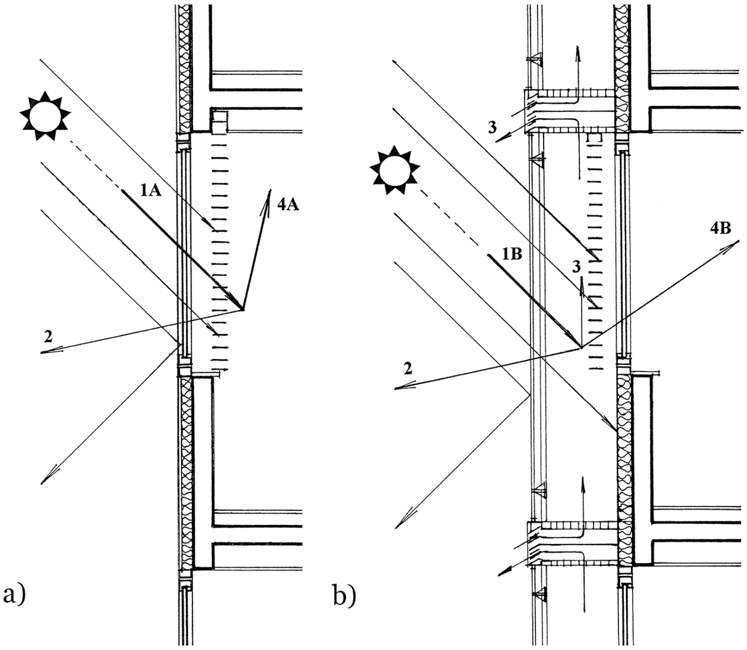

Figure 1. Illustration of classic transparent façade and double-skin transparent façade, a) classic transparent façade, b) double-skin transparent façade: 1A global solar radiation transmitted into the building, 1B – global solar radiation transmitted to the cavity, 2 – heat flux by transfer to the exterior, 3 – heat consumed to heat the air and conducted to the outside climate, 4A – heat load of the building in summer, 4B – heat flux through the transfer to the building – heat load of the building core during the summer.

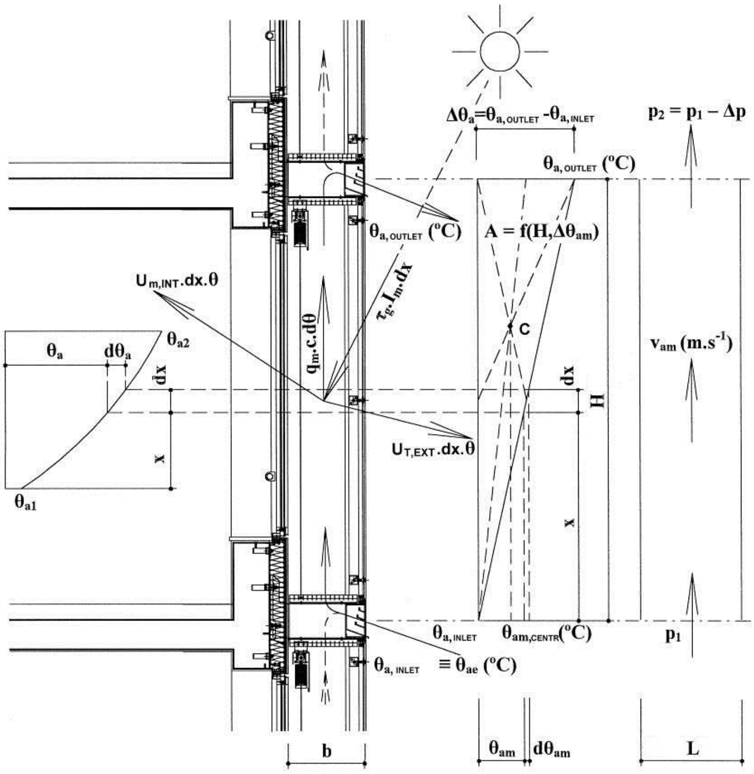

Figure 2. Quantification of aerodynamic and energy regimes of DSTF with open circuit. Width of cavity is $0.5 \le b \le 1.5\,\mathrm{m}$ (corridor type cavity). Height of the cavity H [m] is identical to floor height.

based on natural convection, wind, and their combination.

3.1. Aerodynamic quantification of the cavity

It is necessary to know the total aerodynamic resistance of the cavity for the quantification of the air flow rate q_m [kg/s] under the windless conditions:

$$Z = 1 + \sum Z_l + \sum Z_m = 1 + \sum \frac{\bar{\lambda} \cdot (H+b)}{D_h} + \sum_{x=1}^{10} \xi_x, \quad (2)$$

where $\sum Z_l$ is the sum of the frictional resistance along the entire height of the cavity [-], $\sum Z_m$ is the sum of the local aerodynamic resistance [-], H is the cavity height [m], b is the cavity width [m], $\bar{\lambda}$ is the coefficient of the friction along the entire height of the cavity [-], $\bar{\lambda} = f(Re), Re$ [-] is Reynolds number, as mentioned in Figure 3, ξ_x is the aerodynamic coefficients of local resistance along the airflow trajectory through the cavity [-] as explained in Figure 4, D_h is the aerodynamic cavity diameter [m].

The resistances are longitudinally directly proportional to the length of the trajectory of the movement of the airflow in the cavity $H + b$ (Eq. 2), as shown in Figure 2, and which is in contrast to the diameter of the cavity D_h [m]. Local resistances are connected to the exact space of the airflow movement inside the cavity and are made of parts where the speed or path of the airflow differs (Fig. 2).

It is essential that the total aerodynamic resistance Z must be lesser than the convective air buoyancy power of the air in the cavity, if we want to achieve the required airflow through the cavity in all climatic situations (including the windless situation):

$$\max Z \ = \ 1 + \sum \frac{\bar{\lambda}.(H+b)}{D_h} + \sum_{x=1}^{n} \xi_x < 18 \ , \quad (3)$$

Two local resistances are vital in order to calculate Z (Eq. 3):

(1.) the local aerodynamic resistance at the inlet of the channel ξ_1 with rain protective louvers A ξ_2, which characterizes the turbulence at the outlet of the channel B (Fig. 4),

(2.) the local aerodynamic resistance at the outlet channel from the cavity ξ_{10} with a rain louver A ξ_9, which is responsible for the turbulence of the air flow from the output channel G (Fig. 4).

The rain louvers at the inlet and outlet have a role to prevent the penetration of rainwater from wind-driven rain into the cavity. The aerodynamic coefficients of the local resistances are determined in accordance with the aerodynamic theory shown in Figures 5 and 6. The slats of louvres can be designed as classical rain screens or aerodynamic slats. Their local aerodynamic resistances at the inlet of a distribution channel are shown in Figure 7, and the outlet of the distribution channel is shown in Figure 8.

From the analysis of drag coefficients, conventional rain louvers on an inlet of DSTF are not optimal. It can be summarized as follows:

(1.) The optimal ratio to the total area with conventional rain louvers cannot be ensured (Eq. 4):

$$\frac{a}{A}.100 \cong 80\,\% \ , \quad (4)$$

where a is a net area of openings for the air flow, and A is the total inlet area of the air, including the louvers.

(2.) Typical rain louvers lead to a high local drag coefficient at the inlet (ξ_1), and especially at the outlet (ξ_{10}).

These facts affect the overall aerodynamic drag of the cavity to such a large extent, that it is not possible to ensure the requirement given by Eq. 5:

$$\text{opt.}Z \ = \ 1 + \sum \frac{\bar{\lambda}.(H+b)}{D_h} + \sum_{x=1}^{n=10} \xi_x = 18 \ , \quad (5)$$

The convective buoyancy of air is still higher than the overall aerodynamic resistance of the cavity Eq. 5. It means that the convective movement of the air flow is ensured in the cavity naturally without any wind. But the application of conventional louvers leads to the large drag coefficient, which blocks the naturally convective flow. Therefore, it is recommended to use the aerodynamic louvers with local resistances of $\xi_1 \leq 1.0$ and $\xi_{10} \leq 3.0$ at the inlet and outlet. For the calculation and verification, a numerical approach it can be used. To ensure a simulation with accurate boundary conditions, the Computational Fluid Dynamics (CFD) can be used as one possible method. Figure 9 shows the simulation performed in FLOTRAN.

The total drag of the cavity of the convective air flow is shown in Eq. 6:

$$v_{am} = \sqrt{\frac{g.H.\Delta\theta_{am}}{Z.\theta_{am,T}}}, \quad (6)$$

where $\Delta\theta_{am}$ is the increase in temperature in the cavity [K], g is the gravitational acceleration [9.81 m/s^2],

$$\Delta\theta_{am} = \theta_{a,OUTLET} - \theta_{ae}, \quad (7)$$

where $\Delta\theta_{am,T}$ is the temperature at the point in the centre of mass $A = f(H, \Delta\theta_{am})$ [°C]:

$$\theta_{am,T} = \theta_{ae} + \frac{\theta_{a,OUTLET} - \theta_{ae}}{3}. \quad (8)$$

From the velocity of the convective air flow v_{am} [m/s] and cross-section of the cavity of the double-skin façade $A = L.b$ [m^2], the flow rate in the cavity

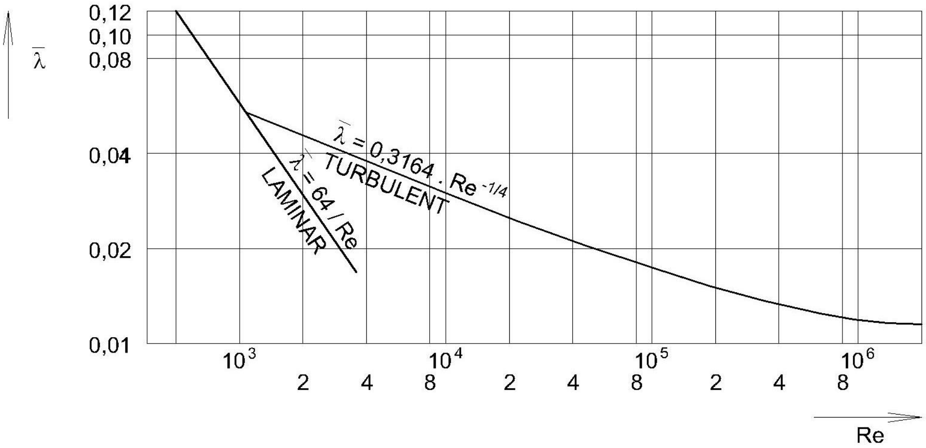

Figure 3. Coefficient of friction as a function of Re number.

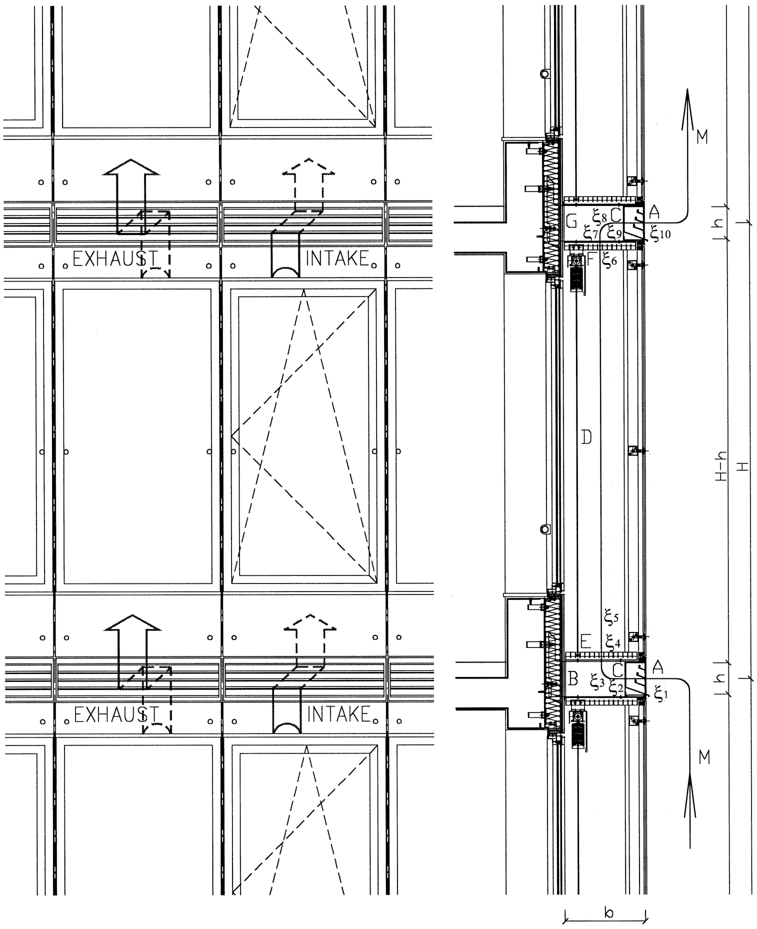

Figure 4. Description and quantification of aerodynamic resistances.

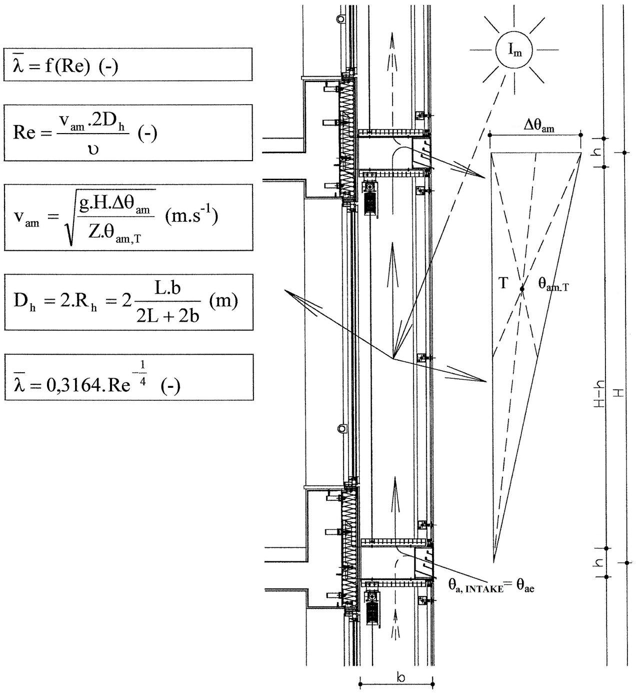

FIGURE 5. Friction resistance along the height of the convective air flow (Re – Reynolds number [-], v_{am} – air flow velocity in the cavity [m/s], ν – coefficient of kinematic viscosity of air [m^2/s], g – gravitational acceleration coefficient [9.81 m/s^2], θ_{am} – increase in tempretature in the cavity [K], $\theta_{am,T}$ – temperature in the centre of mass $A = f(H, \Delta\theta_{am})$ [°C]).

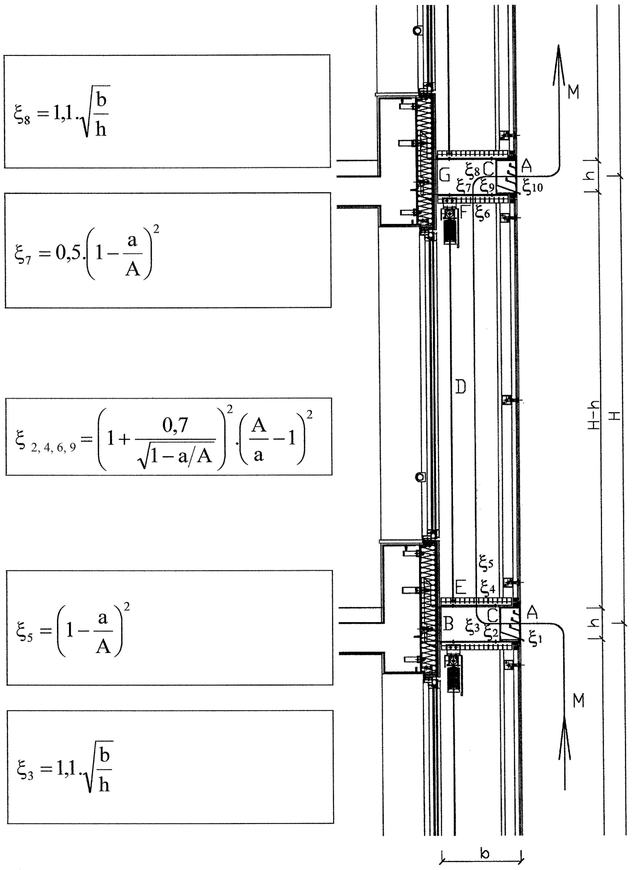

FIGURE 6. Coefficients of local resistances ξ_2, ξ_3, ξ_4, ξ_{52}, ξ_6, ξ_7, ξ_8, ξ_9 [-] in the air flow movement (a – net area opening for air movement, A – total area of the air inlet including its solid parts, b – planar width of the rectangular cross-section, h – height of rectangular cross section).

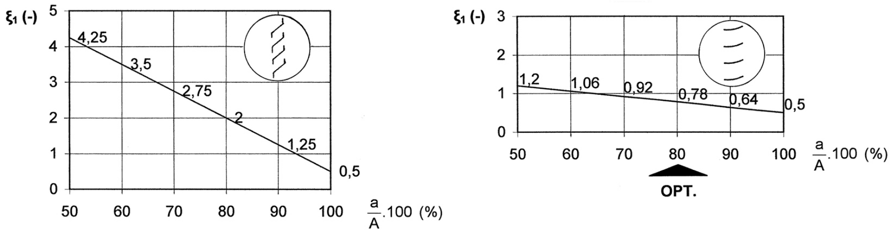

Figure 7. The local drag of the air flow at the inlet. Left picture illustrates the conventional rain louvers, Right picture shows aerodynamic louvers (A – total area of the inlet air, including the louvers, a – net opening area for air flow).

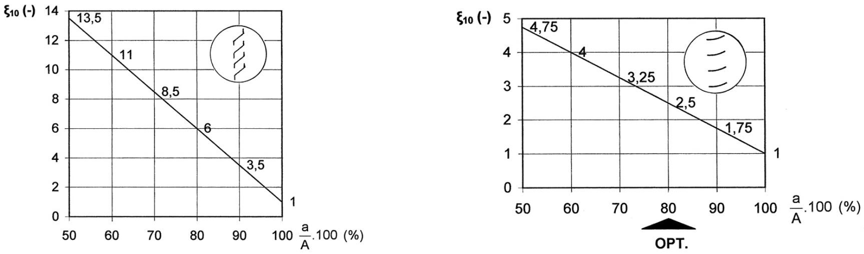

Figure 8. The local drag of the air flow at the outlet. Left picture shows conventional rain louvers, Right picture illustrates aerodynamic louvers (A – total area of the inlet air, including the louvers, a – net opening area for air flow).

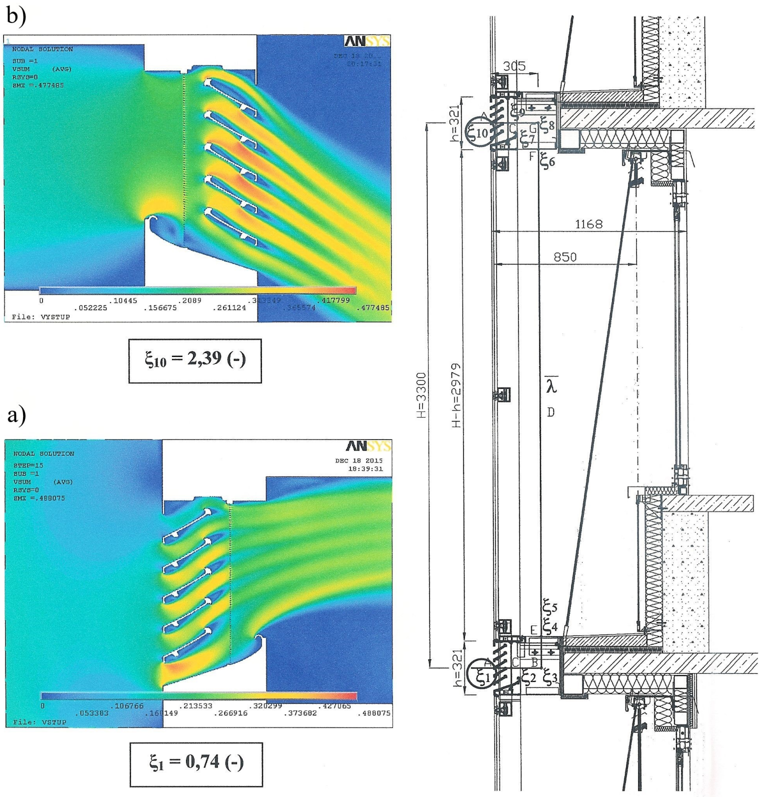

Figure 9. Simulation of the local aerodynamic drag coefficients ξ_1 and ξ_{10} in ANSYS FLOTRAN. Velocity contour plot at the inlet [20].

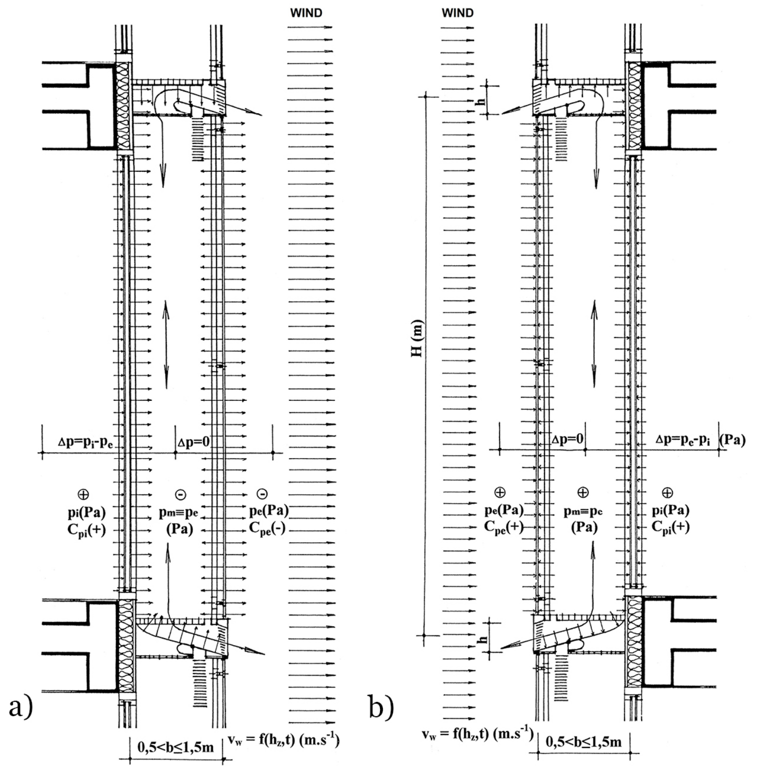

Figure 10. Aerodynamic loads on the DSTF with open circuit under wind condition a) Leeward side of the building, b) Windward side of the building.

can be quantified:

$$q_V = A.v_{am} = L.b.v_{am}, \tag{9}$$

$$q_m = q_V \cdot \rho_{am,T} = L.b.v_{am} \cdot \rho_{am,T}, \tag{10}$$

where $\rho_{am,T}$ is the air density in the centre of mass „C“ at the temperature $\theta_{am,T}$ [kg/m^3] in Figure 2.

The main requirement of the air flow in the cavity of DSTF in windless climate conditions is that Z [-] must be less than the force of the convective air buoyancy [6]. Natural convection is a phenomenon, which describes the dynamics of fluid (air) and depends on the difference of the temperature and density as a consequence of gravitational forces.

3.2. Aerodynamic quantification of the building – external pressure coefficient

The external pressure coefficient has to be known to determine the airflow rate in the cavity q_m [kg/s] for wind conditions (Fig. 10):

$$c_{\mathrm{pe}} = \frac{p - p_0}{\frac{1}{2}\rho_0 \cdot v_{w,0}^2}, \tag{11}$$

The total pressure is defined as:

$$c_{\mathrm{p}} = c_{\mathrm{p}} + c_{\mathrm{pm}}, \tag{12}$$

where c_{pm} is the cavity pressure coefficient [-].
Air flow rate is defined as:

$$q_V = 2\,(L.h)\,.\sqrt{c_{\mathrm{p}} \frac{v_{w,z}^2 \cdot \rho_{ae}}{2}}, \tag{13}$$

where $v_{w,z}$ is the gust velocity of wind [m/s], and ρ_{ae} is the density of the external air [kg/m^3].

Wind loads on buildings can be evaluated from codes [21], wind tunnel tests, CFD and in-situ measurements. The data contained in standards are issued from wind tunnel experiments, performed on an isolated building in open exposure. Measurements by several works have shown that wind loads on buildings in close vicinity are considerably different from those on an isolated building. These effects arise because of the modifications of the flow field due to the surroundings. The experimental determination of the pressure coefficients is a typical aerodynamic task. It is solved on a „rigid model“ in a wind tunnel. Boundary layer wind tunnel (BLWT) is an experimental facility used for modelling the Earth's atmosphere and it allows the experimental measurement of static and dynamic effects of wind on scale models – Figure 11. Wind tunnels with a developed atmospheric boundary layer provide a complete statistical description of the load test objects in a wind flow with a natural structure. For acquisition of external pressures from the measurement, a pressure transducer, which is conducted with plastic tubes and pressure taps with the rigid model, is used. The transducer records differential pressure. Then, according to Eq. 11, the differential pressure is divided by dynamic pressure. It is the principle of experimental measurement with a pressure transducer.

The simulated boundary layer requires similarity criteria in four basic parameters:

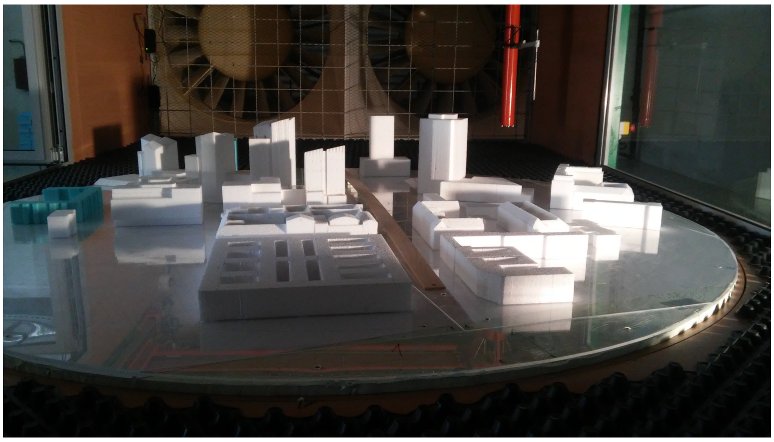

Figure 11. View of the measured buildings in the BLWT in Bratislava [22].

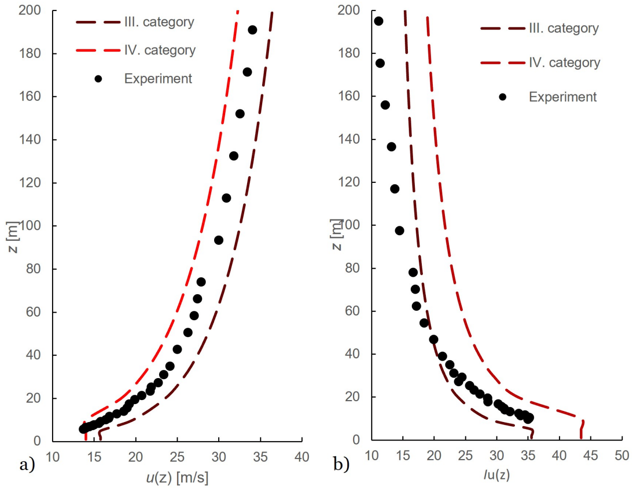

Figure 12. Properties of ABL in BLWT Bratislava: a) Mean wind velocity, b) Intensity of turbulence profile [23].

(1.) longitudinal mean velocity profile,

(2.) longitudinal turbulence intensity profile,

(3.) turbulence integral length scale,

(4.) non-dimensional power spectral density function.

Longitudinal mean wind velocity follows the logarithmic law according to Eq. 14. The longitudinal turbulence intensity is found to agree well with Eq. 15. The illustrative profile of mean wind velocity and turbulence intensity is in Figure 12.

$$U_{(z)} = \frac{u^*}{\kappa} ln \frac{z}{z_0}, \tag{14}$$

$$I_u = \frac{\sqrt{\overline{u'^2}}}{U_z}, \tag{15}$$

where $U_{(z)}$ is the mean wind velocity at the height z [m/s], u^* is the shear velocity [m/s], z_0 is the roughness length [m], I_u is the longitudinal turbulence intensity [-], $\sqrt{\overline{u'^2}}$ is RMS of the turbulent velocity fluctuations [m/s]. Non-dimensional power spectral density is illustrated in Figure 13.

The second possible way to quantify the aerodynamic coefficients of the external pressure on the surface of a building envelope is a simulation using Computational Fluid Dynamics (CFD). CFD is a fluid mechanics division that uses numerical analyses and algorithms to solve problems including fluid flow, heat and mass transfer and other related phenomena. There are some mathematical evaluations of an atmospheric flow simulation [25], [26]. For a simulation of convection, Navier-Stokes equations are used. The flow is treated as incompressible because the Mach number for our tasks is below 0.3. The Navier-Stokes equations for incompressible flow can be written as:

$$\frac{\partial p}{\partial t} + \frac{\partial}{\partial x_i}(\rho \bar{u_i}) = 0 \ , \tag{16}$$

$$\frac{\partial}{\partial t}(\rho \bar{u_i}) + \frac{\partial}{\partial x_j}(\rho \bar{u_i} \bar{u_j}) = \frac{\partial}{\partial x_j}(\sigma_{ij}) - \frac{\partial \bar{p}}{\partial x_i} - \frac{\partial \tau_{ij}}{\partial x_j}, \tag{17}$$

where p is the pressure of the flow [Pa], t is the time duration [s], x is the dimension [s], u is the velocity of flow [m/s], ρ is the density of flow [kg/m^3], σ_{ij} is the stress tensor [-], τ_{ij} is the subgrid-scale stress [-].

In general, there are four methods for solving N-S equations. First one is the Direct Numerical Simulation (DNS), when a problem in space and time is

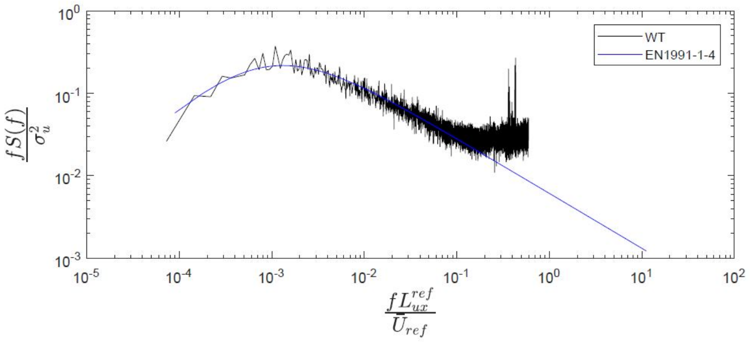

Figure 13. Power spectral density in BLWT Bratislava [23].

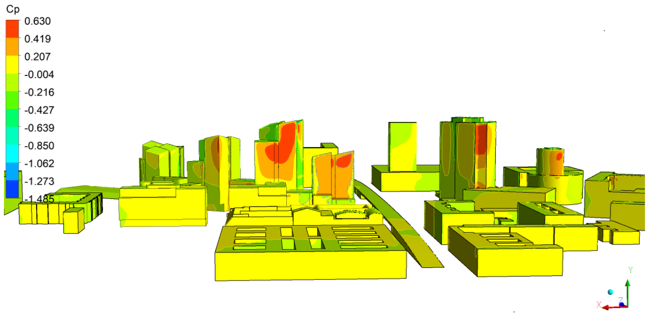

Figure 14. Distribution of external pressure coefficient on the envelopes of a group of buildings received from the ANSYS Fluent [22].

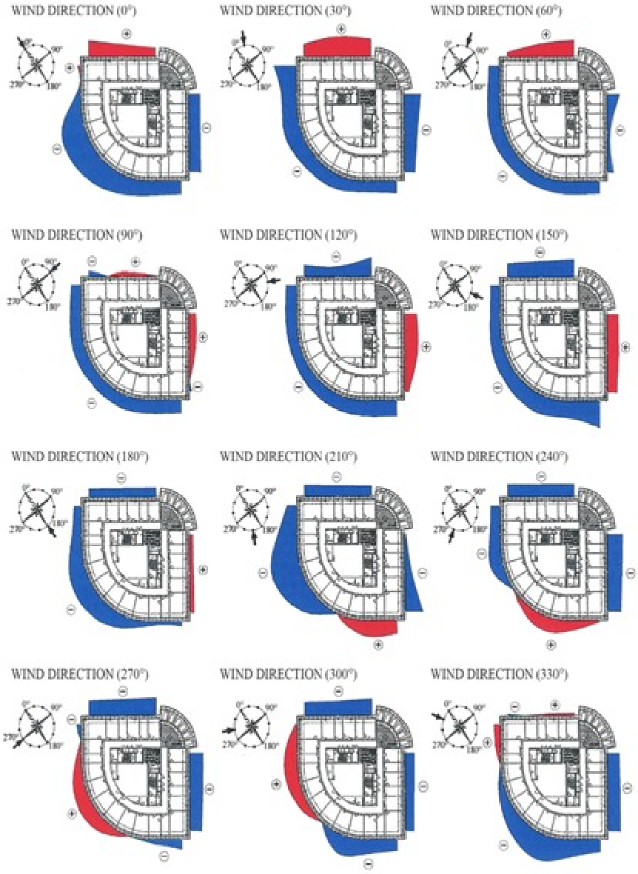

Figure 15. Distribution of external pressures of the building of the National Bank of Slovakia (NBS) in Bratislava on the 17th floor, $H = 56.3\,\mathrm{m}$ [24].

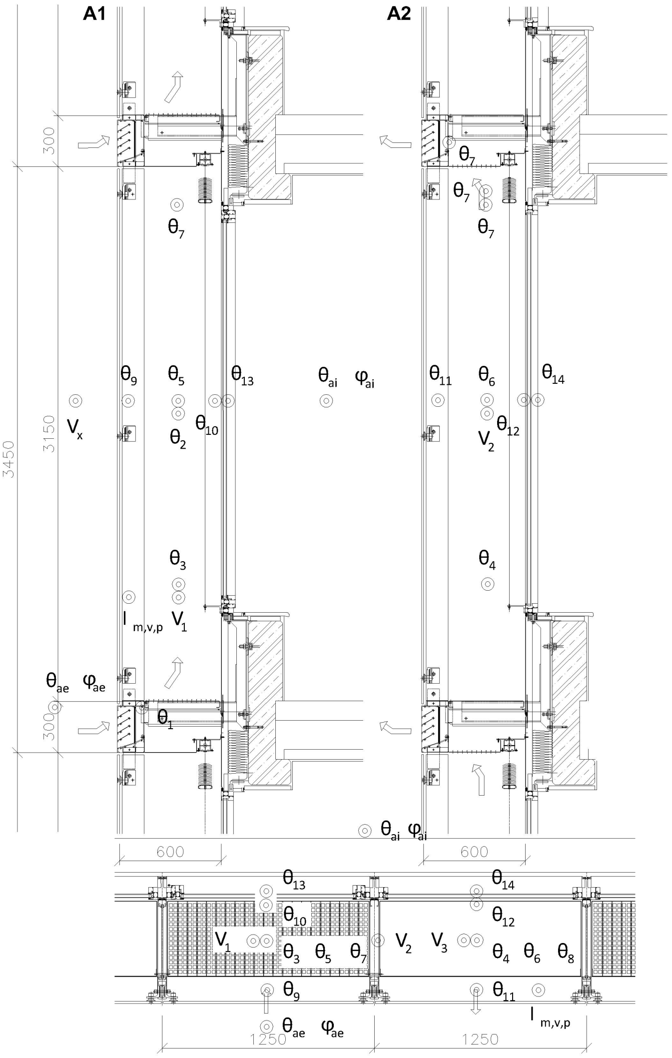

Figure 16. Geometry of DSTF and drawing of measured points.

solved, the second one are Reynolds Averaged N-S equations (RANS). The third method is a combination of both previous methods, which simulates large vortices and modells small structures with the help of Reynolds equations. It is called the Large Eddy Simulation (LES). Current methods for solving RANS are Scale-Resolving Simulation models (SRS). An example of a graphical output of a quantification of external pressures on a building façade from the CFD calculation program is documented in Figure 14.

To obtain the overall aerodynamic pressure coefficient, it is necessary to evaluate the pressure over the entire height of a building, which is documented in Figure 15. The CFD model has to be correctly validated with experimental or situ measurements to achieve correct results. The validation procedure involves an exact modelling of the boundary conditions with experimental or situ measurements. The results are then statistically evaluated to see if they correlate with the experiment. Deviations from the experiment are then assessed, and a numerical model is calibrated to achieve the most accurate results.

4. In situ measurement-preparation

An in-situ measurement experimentally confirmed the above theory on a double-skin facade with a corridor-type cavity width = 600 mm, with an effective height of the cavity identical to the height of the floor = 3450 mm, Fig. 16. The total aerodynamic resistance of the facade was evaluated according to Eq. 3

$$\max Z = 1 + 0.20 + 14.94 = 16.14 < 18,$$

which expresses the convective buoyancy of the air. It can be stated that in terms of functional aerodynamics of the cavity, the airflow through the cavity is ensured in any climatic situation. The measuring setup monitored the temperature and aerodynamic regimes of DSTF during 18 months on the 17th floor of a southwest façade, which was 56.3 m in height. The

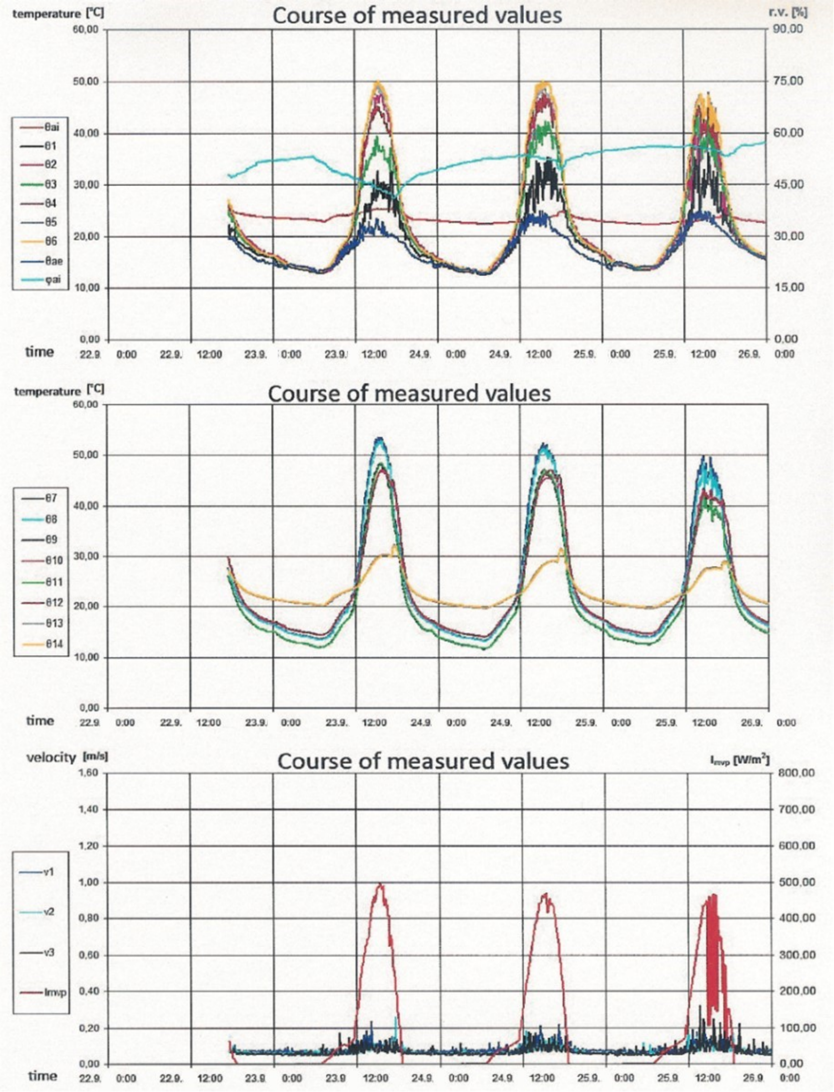

Figure 17. Measured variables from the experiment for the typical period of clear windless warm weather.

recorded parameters were the temperature, relative humidity, and wind velocities in the control points, as is shown in Fig. 16.

Due to the large volume of measuring points and results, we will focus on the critical state of windless conditions in this article. When the airflow in the cavity of DSTF is based on natural convection. Recording of the measured variables in the cavity for the period of clear windless warm weather is illustrated in Fig. 17.

5. Results and discussion

The following conclusions were found based on long-term measurements of temperatures, the effects of solar radiation and relative humidity in-situ conditions when the facade was treated under windless conditions, Fig. 18:

- the convection occurs in the cavity at every time step with the velocity ranging from $0.05 \leq v$ [m/s] ≤ 0.2 to 0.3,
- the convective velocity through the cavity increases due to the growth of global solar radiation,
- the energy regime in the cavity is characterised by inhomogeneity due to the alternating position of the air inlet and air outlet modules,
- in the cavity, there are 3 characteristic zones for aerodynamic and thermal regimes:

  zone of increasing temperatures (around 29 °C) along the height of the cavity in the inlet – the movement of convective airflow,

  a large area with temperatures in the air outlet-stagnation of air (around 47 °C)

  a small area with particularly high temperatures in the upper part of the inlet (around 53 °C) – the state of no flow, stagnation of air. This means a 29 °C temperature gradient as compared to the outside temperature.

Based on these results, we can evaluate a constant airflow in any climatic situation, even in windless conditions. It confirms the correct physical function of the cavity and testifies to the quality of DSTF in terms of its aerodynamic dimensions.

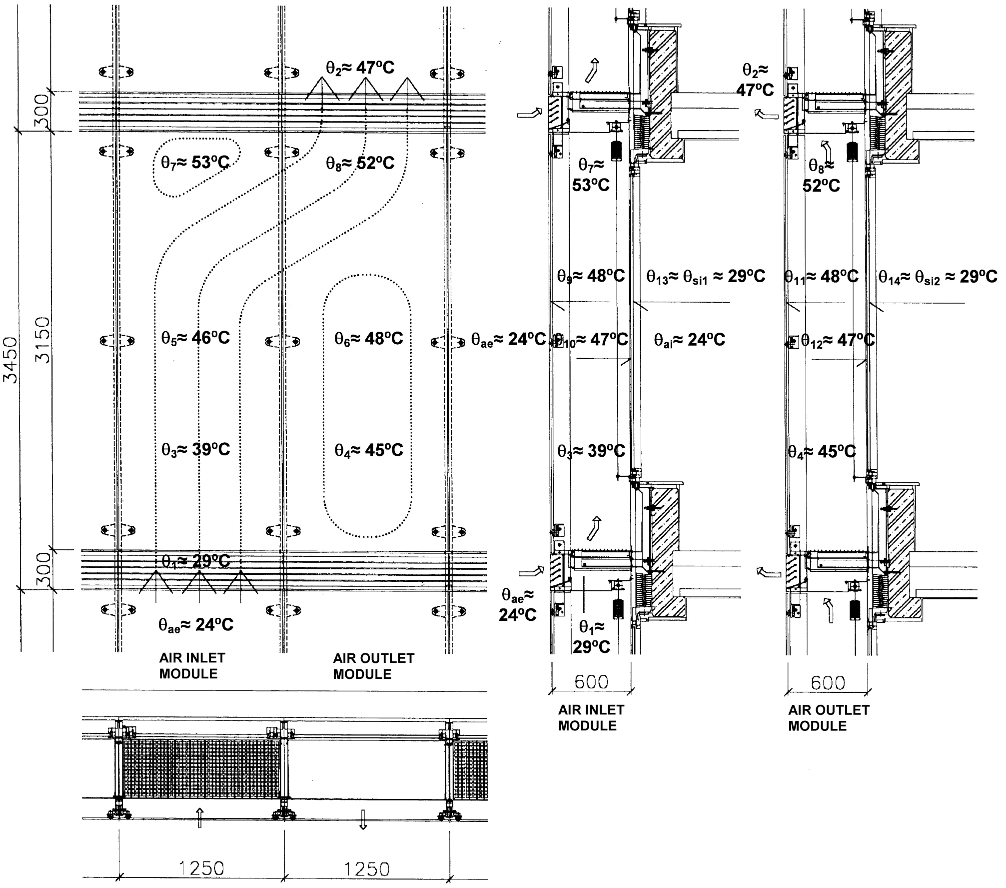

FIGURE 18. The resulting temperature zones during the clear windless warm weather.

6. CONCLUSIONS

The theory and practice of natural physical cavities is a very significant area of the future façade technologies of intelligent buildings. It is directly connected with two very efficient and available alternative energy sources, solar radiation and wind energy, but most often, their very significant combinations. Natural physical cavities allow for wide modifications in the creation of the new façade technology of buildings in the material-structural and shape-aesthetic concepts of modern architecture.

The functional aerodynamics of the cavity of the DSTF in any climatic situation (even in a critical windless state) is an essential precondition for its optimal temperature and energy regime. It can be seen from the experience of the implementation of naturally ventilated DSTF in the modern world that underestimating the dimensioning of elements can lead to severe defects. It can lead to an uncomfortable temperature regime (stagnation of hot air in the cavity in summer). To quantify the temperature and energy regime of DSTF, we must know two basic aerodynamic inputs:

(1.) aerodynamic quantification of the building characterised by an external pressure coefficient, which we can obtain from experimental measurements in the BLWT or from CFD simulations,

(2.) aerodynamic quantification of the interspace characterised by its total aerodynamic resistance.

With their help, we can quantify the air flow through the cavity, the increase in temperature and the resulting energy efficiency of the façade. In-situ measurements of the temperature, aerodynamic, and energy regime of the DSTF during its operation can serve as a standard for debugging and refining calculation procedures and simulation programs. These results significantly contribute to the development of the science and practice.

The design of DSTF has to integrate the multidiscipline approach to ensure the low energy needs. Only a global view can provide a development in the field of architecture.

ACKNOWLEDGEMENTS

This work was supported by the Scientific Grant Agency MŠVVŠ SR and SAV under VEGA 1/0113/19, Slovak Research and Development Agency under the contract No. APVV-21-0144.

REFERENCES

[1] B. Bielek, J. Híreš, D. Lukášik, M. Bielek. *Development of technology in architecture for sustainable society.* Nakladatel'stvo STU, Bratislava, 2012.

[2] B. Todorovic, B. Maric. *The influence of double facades on building heat losses and cooling loads.*

Faculty of Mechanical Engineering, Belgrade University, Belgrade, Yugoslavia, 1999.

[3] D. M. Arons. *Properties and applications of double-skin building facades*. Ph.D. thesis, Massachusetts Institute of Technology, 2000. `http://hdl.handle.net/1721.1/8724`.

[4] G. Gan. Thermal transmittance of multiple glazing: computational fluid dynamics prediction. *Applied Thermal Engineering* **21**(15):1583–1592, 2001. `https://doi.org/10.1016/S1359-4311(01)00016-3`.

[5] D. Saelens, H. Hens. Experimental evaluation of airflow in naturally ventilated active envelopes. *Journal of Thermal Envelope and Building Science* **25**(2):101–127, 2001. `https://doi.org/10.1106/CU0X-XL16-6QTA-29QC`.

[6] J. Hensen, M. Bartak, F. Drkal. Modeling and simulation of a double-skin façade system. *ASHRAE Transactions* **108**(2):1251–1259, 2002.

[7] D. Saelens. *Energy performance assessment of single storey multiple-skin facades*. Ph.D. thesis, Katholieke Universiteit Leuven, Belgium, 2002.

[8] E. Gratia, A. De Herde. Natural ventilation in a double-skin facade. *Energy and Buildings* **36**(2):137–146, 2004. `https://doi.org/10.1016/j.enbuild.2003.10.008`.

[9] J. von Grabe. A prediction tool for the temperature field of double facades. *Energy and Buildings* **34**(9):891–899, 2002. `https://doi.org/10.1016/S0378-7788(02)00065-8`.

[10] N. Mingotti, T. Chenvidyakarn, A. W. Woods. The fluid mechanics of the natural ventilation of a narrow-cavity double-skin facade. *Building and Environment* **46**(4):807–823, 2011. `https://doi.org/10.1016/j.buildenv.2010.09.015`.

[11] K. Nore, B. Blocken, J. Thue. On CFD simulation of wind-induced airflow in narrow ventilated facade cavities: Coupled and decoupled simulations and modelling limitations. *Building and Environment* **45**(8):1834–1846, 2010. `https://doi.org/10.1016/j.buildenv.2010.02.014`.

[12] J. M. Blanco, P. Arriaga, E. Rojí, J. Cuadrado. Investigating the thermal behavior of double-skin perforated sheet façades: Part A: Model characterization and validation procedure. *Building and Environment* **82**:50–62, 2014. `https://doi.org/10.1016/j.buildenv.2014.08.007`.

[13] H. Manz, H. Simmler. Experimental and numerical study of a mechanically ventilated glass double façade with integrated shading device. In *Research in Building Physics*, pp. 519–526. CRC Press, 2020. `https://doi.org/10.1201/9781003078852-71`.

[14] Z. Zeng, X. Li, C. Li, Y. Zhu. Modeling ventilation in naturally ventilated double-skin façade with a venetian blind. *Building and Environment* **57**:1–6, 2012. `https://doi.org/10.1016/j.buildenv.2012.04.007`.

[15] J. Parra, A. Guardo, E. Egusquiza, P. Alavedra. Thermal performance of ventilated double skin façades with venetian blinds. *Energies* **8**(6):4882–4898, 2015. `https://doi.org/10.3390/en8064882`.

[16] W. Streicher, R. Heimrath, H. Hengsberger, et al. On the typology, costs, energy performance, environmental quality and operational characteristics of double skin façades in european buildings. *Advances in Building Energy Research* **1**(1):1–28, 2007. `https://doi.org/10.1080/17512549.2007.9687267`.

[17] B. Bielek, M. Bielek, M. Palko. *Double-skin transparent facades of buildings*. Coreal, Bratislava, 2002.

[18] A. Compagno. *Intelligent glass facades: material, practice, design*. Birkhauser, 1995.

[19] E. Oesterle. *Double skin facades: integrated planning; building physics, construction, aerophysics, air-conditioning, economic viability*. Prestel, 2001.

[20] M. Palko, A. Palková. Selected aerodynamic problems of double skin facade. *Advanced Materials Research* **1057**:137–144, 2014. `https://doi.org/10.4028/www.scientific.net/AMR.1057.137`.

[21] STN EN 1991-1-4. Eurocode 1: Actions on structures. Part 1-4: General actions. Wind actions. Slovak Office of Standards, Metrology And Testing, 2007.

[22] O. Hubová, M. Macák, M. Franek, V. Mitro. *CFD Simulation and Experimental Verification of Wind Flow around Building Complex in Budapest*. Slovak University of Technology, 2017.

[23] M. Franek. *Impact of the interference effects on the distribution of the external pressure coefficient for elliptic high – rise buildings*. Ph.D. thesis, Slovak University of Technology, 2017.

[24] L. Ilg, B. Bauhofer. *Slowakische Nationalbank Zentrale in Bratislava – Windrück an der Gebäudekülle – Windkanalstudie*. ETH Zürich – HL-Technik AG München, 1996.

[25] D. C. Wilcox, et al. *Turbulence modeling for CFD*, vol. 2. DCW industries La Canada, CA, 1998.

[26] K. Hanjalić, B. Launder. *Modelling turbulence in engineering and the environment: second-moment routes to closure*. Cambridge University Press, 2011.

Acta Polytechnica **62**(4):473–478, 2022
`https://doi.org/10.14311/AP.2022.62.0473`

EVALUATION OF RESIDUAL STRENGTH OF POLYMERIC YARNS SUBJECTED TO PREVIOUS IMPACT LOADS

Gabriela Hahn[a],
Antonio Henrique Monteiro da Fonseca Thomé da Silva[b, c],
Felipe Tempel Stumpf[d], Carlos Eduardo Marcos Guilherme[a, *]

[a] *Universidade Federal do Rio Grande, Policab – Stress Analysis Laboratory, Av. Itália km. 8, 96203-000 Rio Grande, Brazil*

[b] *Petróleo Brasileiro SA – Petrobras, CENPES R&D Centre, Ilha Cidade Universitária - Cidade Universitária, 21941-915 Rio de Janeiro, Brazil*

[c] *Universidade Federal Fluminense – Departamento de Engenharia Mecânica, Rua Passo da Pátria 156 Bl. D., 24210-240 Niterói, Brazil*

[d] *Universidade Federal do Rio Grande do Sul, Departamento de Engenharia Mecânica, Rua Sarmento Leite 425, 90050-170 Porto Alegre, Brazil*

[*] corresponding author: `carlosguilherme@furg.br`

Abstract.

The discovery of oil fields in deep and ultra-deep waters provided an opportunity to evaluate the use of synthetic ropes, complementarily or alternatively to traditional steel-based mooring lines in offshore units, mainly because of the former's lower specific weight. Considering the series of complex dynamic-mechanical mainly axial loads to which these structures may be subjected, originated from different sources, such as wind, water current, tide, etc., there may be cases when at least one of these lines may possibly face an abrupt, shock-like axial load of considerably larger magnitude. The goal of the present study is to evaluate the residual tensile strength of three different synthetic yarns (polyester, and two grades of high modulus polyethylene) after exposure to such axial impact loads. It was observed that, for the tested materials, polyester is the one with the largest impact resistance to the conditions evaluated herein, mainly because of its comparatively greater energy absorption properties.

Keywords: Offshore mooring, ultra deep-water, impact load.

1. Introduction

Since the end of the World War II, there has been an increase in the application of synthetic materials, mainly because of the reduction of their production costs and their significantly advantageous mechanical properties [1]. As an example, one can mention the construction of polymeric ropes, which can be used in a wide range of sports and industrial applications, such as climbing, rescue operations, mooring of offshore structures, shipping operations, etc. [2].

During the 1990s, the offshore oil industry began to replace the traditional mooring system based on steel cables and chains by systems consisting mainly of polyester cables. The main motivation for this shift was the severe increase in the water depth in which these structures were now being anchored, requiring compliant ropes with low specific weight in order to reduce the overall weight of the floating system [3, 4]. Nowadays, as examples, one can mention the synthetic fibres typically used for mooring ropes manufacturing: polyester (PET), high modulus polyethylene (HMPE), polyamide (PA), liquid crystal polymer (LCP), aramid and polypropylene (PP).

Apart from the mechanical loads originating from the movement of the floating unit, such anchoring systems may be subjected to some degree of environmental damage caused, for example, by ultraviolet incidence and hydrolysis, depending on the fibre group [5, 6]. Yarn-on-yarn abrasion is another (now a mechanical) degradation mechanism, even more relevant than the previous ones, that can affect the material's mechanical behaviour [7]. For characterisation purposes considering mooring ropes applications, static and dynamic stiffness of polymeric multifilaments are typically assessed according to ISO 18692 [8] and ISO 14909 [9, 10].

Polyester yarns have a high mechanical resistance, good tenacity and abrasion resistance [7, 11, 12]. When exposed to the environment under typical mooring conditions, they do not degrade considerably and are resistant to hydrolysis and ultraviolet incidence [5, 13]. Polyester is also not biodegradable, has a negligible creep behaviour at room temperature and, when exposed to high temperatures, it contracts instead of expanding [14, 15].

High modulus polyethylene is produced from a gel spinning process, resulting in a highly crystalline structure, oriented and extended along the fibre axis, with many different grades available in the market with specific properties. In general, HMPE fibres present a lower-than-water density allowing its buoyancy in regular water, which makes it a very interesting choice for marine applications. As for its mechanical properties, the fibre has a high tenacity and stiffness as compared to similar materials. Also, the deformation of HMPE at rupture is very low, but it shows remarkable creep behaviour at lower temperatures [16, 17].

There is a lack of previous studies in the literature regarding the influence of severe and abrupt tensile loads on the mechanical properties of polymeric materials applied to mooring ropes. However, it represents a relevant topic in regards to synthetic fibres used for mooring and operation lines since during its lifetime, an anchoring or operation line might be exposed to such loads several times. One important factor that influences the capacity to support shock loads is the degree of crystallinity, which is inversely proportional to the resistance to high, instantaneous tensile forces [18, 19].

Considering the aforementioned, the main goal of this paper is to assess the residual tensile strength of polyester and high modulus polyethylene yarns exposed to a prior shock-like axial load.

2. Materials and methods

2.1. Materials

In the present work, one grade of PET and two different grades of HMPE are evaluated, referred to as PET, HMPE1 and HMPE2, respectively. The materials have titers of 3300 dtex, 1761 dtex, and 1759 dtex, respectively.

2.2. Methods

2.2.1. Environmental conditions during tests

All tests were performed with 500 mm long yarn specimens conditioned according to ISO 139:2014, which determines that the samples must stay for at least two hours in an environment at 20 ± 2 °C and a relative humidity of 65 ± 4 % prior to any experimental procedure. The tests themselves must also be performed in such environmental conditions.

2.2.2. Tensile tests in reference unexposed samples

To determine the YBL reference values, for comparison purposes, unexposed fibres were tested according to ASTM D2256. 30 rupture tests were performed for 500 mm long yarn samples of PET, HMPE1 and HMPE2 at 250 mm/min. Prior to tensile testing, samples were twisted along their axes with 60rounds per meter. An EMIC DL2000 universal testing machine with a 1 kN load cell was used.

2.2.3. Impact tests

It is considered that there is a critical velocity, above which the material shows brittle behaviour. The British standard BS EN 892:2012 proposes impact tests in mountaineering ropes, which consists in the application of an instantaneous tensile force applied by a free-falling mass (Figure 1) [20]. The input data to the experiment are the rope length, the free fall height, the mass of the falling object, and standard atmospheric conditions, such as temperature and relative humidity. BS EN 892:2012 brings different procedures depending on the investigated factors, such as stiffness, cycle number for impact load, transmitted force in the rope and maximum stretching.

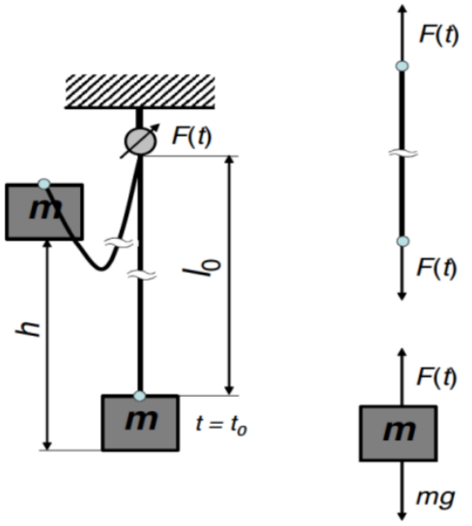

Figure 1. Free-fall diagram. Source [20].

Multifilaments used in the impact test are expected to present the capacity of dissipation and absorption of the potential energy. Specimens must be capable of preserving their original elastic behaviour, granting structural integrity and not compromising their mechanical properties. In the present paper, we apply such loads to the specimens and investigate eventual changes in their yarn break load (YBL) in the two distinct moments: immediately after the impact load, and 24 hours after the test. The YBL of the tested material is compared to that of an unexposed sample.

The application of the abrupt tensile forces was performed with increasingly heavier dead weights, typically from 1 % to 7 % YBL (and higher whenever applicable) increased by 2 % YBL steps. If samples did not fail when exposed to the chosen dead weight, residual strength was evaluated (as described in the next sections) and a new set of impact tests with increased dead weight was performed. In all tests, the dead weight was released from a 250 mm height, which corresponds to a half of the samples' length. A total of 30 untwisted samples were used for each of the investigated materials.

2.2.4. Residual strength tests

2.2.4.1. Residual strength of partially impacted samples

In order to evaluate the intermediate residual quasi-static tensile strength of the materials after the application of each of the impact loads steps detailed in Section 2.2.3, those samples that did not fail by

Material	YBL (N/tex)	Specific deformation at break (%)
PET	0.76 ± 0.01	10.90 ± 0.04
HMPE1	3.04 ± 0.15	3.30 ± 0.14
HMPE2	3.08 ± 0.10	3.20 ± 0.09

Table 1. Yarn break load of reference unexposed samples of PET, HMPE1 e HMPE2.

Material	Maximum impact load promoted by the 1 % YBL dead weight (N/tex)	YBL (N/tex) after impact	Specific deformation at break (%)
HMPE1	1.24 ± 0.03	3.25 ± 0.09	3.30 ± 0.12
HMPE2	1.33 ± 0.02	3.23 ± 0.10	3.20 ± 0.12

Table 2. Results of the tensile tests for residual strength evaluation immediately after the impact load of 1 % YBL.

Material	Maximum impact load promoted by the 3 % YBL dead weight (N/tex)	YBL (N/tex) after impact	Specific deformation at break (%)
PET	0.31 ± 0.01	0.76 ± 0.01	10.30 ± 0.40
HMPE1	2.14 ± 0.13	3.15 ± 0.17	3.20 ± 0.20
HMPE2	2.22 ± 0.10	3.11 ± 0.11	3.20 ± 0.11

Table 3. Results of the tensile tests for residual strength evaluation immediately after the impact load of 3 % YBL.

rupture were subjected to tensile tests using the procedure of Section 2.2.2. The time interval between both experiments was of 1 minute and 30 seconds, during which the samples were kept under the same controlled environmental conditions of Section 2.2.1. The same EMIC DL2000 machine was used.

2.2.4.2. Residual Strength of samples after resting time

A second round of tensile tests was performed in order to evaluate the influence of the resting time of the samples between the impact experiments and the residual tensile strength measurements. For that, instead of testing the samples for their residual YBL immediately after the shock-like events, they were first left to rest for 24 hours in a controlled environment (see Section 2.2.1). After this period, the tensile tests were performed according to the procedure detailed in Section 2.2.2.

3. Results and discussion

3.1. Yarn break load of reference (unexposed) samples

Table 1 shows the results for YBL of PET, HMPE1 e HMPE2, determined according to the experimental setup detailed in Section 2.2.2 considering 30 samples each. It can be seen that PET shows a lower YBL and a higher elongation at break when compared to both grades of HMPE, as expected.

3.2. Tensile tests immediately after the impact loads

As detailed in Section 2.2.3, each material was tested with abrupt tensile loads using an initial dead weight equivalent to 1 % YBL, which exposed the samples to a specific impact load. Due to technical difficulties in measuring the very small force during the tests for PET (approximately 2.5 N), this material was excluded from this first experimental batch.

After the tests with 1 % YBL, no visible damage was observed in any of the HMPE samples. Moreover, no sample has failed during the impact load. Immediately after the impact tests, tensile tests were performed in order to observe eventual changes in the materials' original YBL. Table 2 shows the results considering 30 samples each.

Although the impact forces applied to the samples were close to half of the materials' original YBL, both HMPE showed an apparent increase in their tensile strength: HMPE1 increased its YBL by about 7 % and HMPE2 by about 5 %, when compared to the materials' reference YBL (see Table 1). There was no significant change in the specific deformation at break. It was observed that the standard deviation of the HMPE1 samples decreased as compared to the results in the reference unexposed samples.

Then, additional impact tests were performed, increasing the dead weight to 3 % of the materials' original YBL, now including PET samples. Again, there was no visible damage in any of the samples after the application of the sudden axial loads. Table 3 shows

Material	**Maximum impact load promoted by the 5 % YBL dead weight (N/tex)**	**Number of samples impact tested**	**Samples broken during impact**	**YBL (N/tex) after impact**	**Specific deformation at break (%)**
PET	0.50 ± 0.02	30	0	0.77 ± 0.02	10.50 ± 0.40
HMPE1	2.86 ± 0.12	78	48	Not applicable	
HMPE2	2.98 ± 0.10	54	24	3.09 ± 0.12	3.20 ± 0.13

Table 4. Results of the tensile tests for residual strength evaluation immediately after the impact load of 5 % YBL.

Material	**Maximum impact force caused by dead weight drop (N/tex)**	**Number of samples impact tested**	**Samples broken during impact**	**YBL (N/tex) after impact**	**Specific deformation at break (%)**
PET 7 %	0.62 ± 0.02	30	10	0.77 ± 0.02	10.50 ± 0.35
PET 9 %	0.69 ± 0.01	47	17	0.77 ± 0.02	10.30 ± 0.41
PET 11 %	1.12 ± 0.02	58	28	Not applicable	
HMPE2 6 %	3.09 ± 0.09	52	22	Not applicable	

Table 5. Results of the tensile tests for residual strength evaluation immediately after impact load – higher dead weights.

the results of the tensile tests performed after the impacts considering 30 samples each.

Here, the axial load for the HMPE samples exceeds almost 70 % of the materials' original YBL, while for polyester, it was close to 50 % of its original YBL. The results for PET showed no significant difference when compared to the unexposed reference material (Table 1). Both HMPE samples showed, after impact, a higher YBL than that of the reference samples, but now only 3 % higher for HMPE1 and 1 % for HMPE2. Again there was no significant change in the specific deformation at the break. The high standard deviation of HMPE1 may be an indication of permanent damage caused to the multifilament structure during the impact tests even thoughthe quasi-static mechanical behaviour was not jeopardized.

Increasing the deadweight to 5 % YBL, more than 50 % of the HMPE1 samples failed by rupture during the impact test, which means that the impact strength of that material was reached. Less than half of HMPE2 samples showed failure by rupture. Some of the samples that did not break during the impact test showed visible, macroscopic damage in their structure, while all PET samples did not show any visible structural damage. Table 4 shows the residual tensile strength test results. Impact sampling was performed in order to always guarantee around 30 viable samples for the residual tensile strength tests afterwards.

Results show that, the higher the impact load, the higher the standard deviation and, in this case, it is reaching the limits of the impact tolerance for the HMPE fibres, with a significant amount of fibres already failing under impact. Again, PET showed a very small increase in its tensile strength, while the specific deformation at break remained almost unchanged.

The next set of tests was performed with a deadweight of 7 % YBL. As expected, all samples of HMPE2 have broken during impact, so, for that material, the load was decreased to 6 % YBL, in order to find its impact strength. Following the procedure of increasing the load by 2 % YBL, PET was further tested up to 11 % YBL, which was found to be beyond the material's impact strength. Table 5 shows these results.

3.3. TENSILE TESTS 24 HOURS AFTER THE IMPACT LOADS

In this section, the effect of the time interval between the impact test and subsequent tensile tests on the quasi-static residual strength of the fibres was observed, aiming to observe any potential microstructural accommodation. Therefore, because of the similar mechanical behaviour of HMPE1 and HMPE2, only PET and HMPE1 were chosen to undergo this new set of experiments.

Samples of PET were subjected to an impact load of 5 % YBL and HMPE1 to 3 % YBL. These values were chosen because they were found to be the highest impact loads (among the loads tested in the study) that do not cause macroscopic damage to the material (see Section 3.2). After the impact experiment, the samples were left to rest for 24 hours in a controlled environment as determined by ISO 139:2014. Table 6 shows the results.

In Table 3, it can be seen that PET has a tensile strength of 1.12 ± 0.02 N/tex when the tensile test is performed immediately after the impact test. When

Material	Number of samples	Maximum impact force (N/tex)	YBL (N/tex) after impact	Specific deformation at break (%)
PET 5 % YBL	30	0.50 ± 0.02	0.77 ± 0.02	11.20 ± 0.33
HMPE1 3 % YBL	30	2.14 ± 0.13	3.11 ± 0.01	3.20 ± 0.12

Table 6. Results of the tensile tests for residual strength evaluation 24 hours after impact load.

the tensile test was conducted 24 hours after the impact experiment, the YBL was measured as 1.13 ± 0.02 N/tex. For HMPE1, the equivalent results are of 3.15 ± 0.17 N/tex (immediately after impact) and 3.11 ± 0.01 N/tex (24 hours after impact). It was concluded that the materials tested do not restore their tensile strength after a considerable time interval of 24 hours after the impact test.

4. Conclusions

The main goal of this article is to evaluate an eventual loss in tensile strength of polyester and (two grades of) high modulus polyethylene yarns after an exposure to abrupt, axial impact loads (as a percentage of materials' original YBL). This is made by measuring the YBL of the unexposed reference material's YBL, and comparing it to the YBL of samples previously exposed to different levels of impact loads.

The obtained results suggest that, among the tested materials, PET is the one being less affected by a % YBL impact load, having shown impact strength to an axial load equivalent to about 9 % of its original YBL (see Table 5). Both evaluated grades of HMPE, HMPE1 and HMPE2, presented an impact strength equal to 5 % YBL and 6 % YBL, respectively (see Tables 4 and 5). A possible explanation is that PET's elongation at break (∼10 %) is significantly larger than those of HMPE's (∼3.3 %), which means that the former is more capable of absorbing strain energy than the latter.

Because of the absence of similar studies in the literature, this study is considered to be pioneer in terms of the assessment of the consequences of axial, abrupt loads for the posterior tensile strength of polymeric yarns. The methodology followed here is considered adequate to be applied when one intends to quantitatively compare the impact strength of different polymeric fibres. It should be noted that due to the difference between the axial stiffness of the different tested materials, naturally, the strain rate is expected not to be the same when this approach, based on deadweight release, is used. If one intends to apply exactly the same strain rate to the materials being compared, more sophisticated experimental apparatus must be employed. It is also important to note that the results regarding impact strength can be highly affected by the temperature during the experiments, so it is recommended to perform the shock-like experiments at the service temperature of the materials for more accurate comparisons.

References

[1] Jr. W. D. Callister and D. R. Rethwisch. *Materials Science and Engineering: An Introducion.* John Wiley & Sons, 2007.

[2] A. J. McLaren. Design and performance of ropes for climbing and sailing. *Proceedings of the Institution of Mechanical Engineers, Part L: Journal of Materials: Design and Applications* **220**(1):1–12, 2006. `https://doi.org/10.1243/14644207JMDA75`.

[3] V. Sry, Y. Mizutani, G. Endo, et al. Consecutive impact loading and preloading effect on stiffness of woven synthetic-fiber rope. *Journal of Textile Science and Technology* **3**:1–16, 2017. `https://doi.org/10.4236/jtst.2017.31001`.

[4] K. H. Lo, H. Xü, L. A. Skogsberg. Polyester rope mooring design considerations. In *Ninth International Offshore and Polar Engineering Conference.* Brest, France, 1999. ISOPE-I-99-1691999.

[5] J. P. Duarte, C. E. M. Guilherme, A. H. M. F. T. da Silva, et al. Lifetime prediction of aramid yarns applied to offshore mooring due to purely hydrolytic degradation. *Polymers and Polymer Composites* **27**(8):518–524, 2019. `https://doi.org/10.1177/0967391119851386`.

[6] M. M. Shokrieh, A. Bayat. Effects of ultraviolet radiation on mechanical properties of glass/polyester composites. *Journal of Composite Materials* **41**(20):2443–2455, 2007. `https://doi.org/10.1177/0021998307075441`.

[7] S. R. da Silva Soares, V. E. Fortuna, F. E. G. Chimisso. Yarn-on-yarn abrasion behavior for polyester, with and without marine finish, used in offshore mooring ropes. In *9th Youth Symposium on Experimental Solid Mechanics*, pp. 60–64. 2010.

[8] International Organization for Standardization. Fibre ropes for offshore stationkeeping – Part 2: Polyester (ISO Standard No. 18692-2), 2019.

[9] International Organization for Standardization. Fibre ropes for offshore stationkeeping – High modulus polyethylene (HMPE) (ISO Standard No. 14909), 2012.

[10] F. T. Stumpf, C. E. M. Guilherme, F. E. G. Chimisso. Preliminary assessment of the change in the mechanical behavior of synthetic yarns submitted to consecutive stiffness tests. *Acta Polytechnica CTU Proceedings* **3**:75–77, 2016. `https://doi.org/10.14311/APP.2016.3.0075`.

[11] T. S. Lemmi, M. Barburski, A. Kabziński, K. Frukacz. Effect of thermal aging on the mechanical properties of high tenacity polyester yarn. *Materials* **14**(7):1666, 2021. `https://doi.org/10.3390/ma14071666`.

[12] G. Susich. Abrasion damage of textile fibers. *Textile Research Journal* **24**(3):210–228, 1954. `https://doi.org/10.1177/004051755402400302`.

[13] M. Moezzi, M. Ghane. The effect of UV degradation on toughness of nylon 66/polyester woven fabrics. *The Journal of The Textile Institute* **104**(12):1277–1283, 2013. `https://doi.org/10.1080/00405000.2013.796629`.

[14] C. Oudet, A. Bunsell. Effects of structure on the tensile, creep and fatigue properties of polyester fibres. *Journal of Material Science* **22**:4292–4298, 1987. `https://doi.org/10.1007/BF01132020`.

[15] H. Y. Jeon, S. H. Kim, H. K. Yoo. Assessment of long-term performances of polyester geogrids by accelerated creep test. *Polymer Testing* **21**(5):489–495, 2002. `https://doi.org/10.1016/S0142-9418(01)00097-6`.

[16] P. Davies, Y. Reaud, L. Dussud, P. Woerther. Mechanical behaviour of HMPE and aramid fibre ropes for deep sea handling operations. *Ocean Engineering* **38**(17-18):2208–2214, 2011. `https://doi.org/10.1016/j.oceaneng.2011.10.010`.

[17] Y. Lian, H. Liu, Y. Zhang, L. Li. An experimental investigation on fatigue behaviors of HMPE ropes. *Ocean Engineering* **139**:237–249, 2017. `https://doi.org/10.1016/j.oceaneng.2017.05.007`.

[18] E. Hage Jr. Resistencia ao impacto. In S. V. Canevarolo Jr. (ed.), *Técnicas de Caracterização de Polímeros*. Artliber, São Paulo, 2003.

[19] E. L. V. Louzada, C. E. M. Guilherme, F. T. Stumpf. Evaluation of the fatigue response of polyester yarns after the application of abrupt tesion loads. *Acta Polytechnica CTU Proceedings* **7**:76–78, 2017. `https://doi.org/10.14311/APP.2017.7.0076`.

[20] I. Emri, A. Nikonov, B. Zupančič, U. Florjančič. Time-dependent behavior of ropes under impact loading: A dynamic analysis. *Sports Technology* **1**(4-5):208–219, 2008. `https://doi.org/10.1080/19346182.2008.9648475`.

Acta Polytechnica **62**(4):479–487, 2022
`https://doi.org/10.14311/AP.2022.62.0479`

ACTIVE DISTURBANCE REJECTION CONTROL-BASED ANTI-COUPLING METHOD FOR CONICAL MAGNETIC BEARINGS

Danh Huy Nguyen[a], Minh Le Vu[a], Hieu Do Trong[a],
Danh Giang Nguyen[b], Tung Lam Nguyen[a,*]

[a] *Hanoi University of Science and Technology, School of Electrical Engineering, 1 Dai Co Viet st, Hanoi 100000, Vietnam*

[b] *National University of Civil Engineering, Faculty of Mechanical Engineering, 55 Giai Phong st, Hanoi 100000, Vietnam*

[*] corresponding author: `lam.nguyentung@hust.edu.vn`

Abstract. Conical-shape magnetic bearings are currently a potential candidate for various magnetic force-supported applications due to their unique geometric nature reducing the number of required active magnets. However, the bearing structure places control-engineering related problems in view of underactuated and coupling phenomena. The paper proposes an Adaptive Disturbance Rejection Control (ADRC) for solving the above-mentioned problem in the conical magnetic bearing. At first, virtual current controls are identified to decouple the electrical sub-system, then the active disturbance rejection control is employed to eliminate coupling effects owing to rotational motions. Comprehensive simulations are provided to illustrate the control ability.

Keywords: Conical active magnetic bearings, over-actuated systems, ADRC, coupling mechanism, linearization.

1. Introduction

Recently, active magnetic bearing (AMB) has been of increasing interest to the manufacturing industry due to its contactless, lubrication-free, no mechanical wear, and high-speed capability [1–3]. These characteristics enable them to be employed in a variety of applications, including artificial hearts [4], vacuum pumps [5], and flywheel energy storage systems [6] and [7], etc. The motion resolution of the suspended object in translation or high-speed rotation is restricted solely by the actuators, sensors, and the servo system utilised due to the non-contact nature of a magnetic suspension. As a result, magnetic bearings can be utilised in almost any environment as long as the electromagnetic parts are suitably shielded, for example, in open air at temperatures ranging from 235 °C to 450 °C [8]. Many researchers, in particular, have endeavored to design a range of AMBs that are compact and simple-structured while still performing well. Because of the advantages of a cone-shaped active magnetic bearing (AMB) system, such as its simple structure, low heating, and high dependability, there is an increasing number of studies on it [9, 10]. The structure of a conical magnetic bearing is identical to that of a regular radial magnetic bearing, with the exception that both the stator and rotor working surfaces are conical, allowing force to be applied in both axial and radial directions [11, 12]. The conical form saves axial space, which can be used to install gears and other components for an added mechanical benefit. It also conserves energy for an optimal load support. Conical electromagnetic bearings feature two coupled properties as compared to ordinary radial electromagnetic bearings: current-coupled and geometry-coupled effects, making dynamic modelling and control of these systems particularly difficult. The current-coupled effect exists because the axial and radial control currents flow in the bearing coils simultaneously. Furthermore, the inclined angle of the magnet core causes a geometry-coupled effect. Coupled dynamic characteristics of the rotor conical magnetic bearing system became known due to the existence of the two coupled effects. So far, several researchers have discussed the modelling and control of cone-shaped AMBs [2, 13, 14]. Lee CW and Jeong HS presented a control method for conical magnetic bearings in [12], which allows the rotor to float in the air stably. They proposed a completely connected linearised dynamic model for the cone-shaped magnet coil that covers the relationships between the input voltage and output current. The connected controller uses a linear quadratic regulator with integral action to stabilise the AMB system, while the decoupled controller is used to stabilise the five single DOF systems. Abdelfatah M. Mohamed et al. [11] proposed the Q-parameterization method for designing system stabilisation in terms of two free parameters. The proposed technique is validated using a digital simulation. As a result, plant parameters such as transient and forced response are good, and stiffness characteristics are obtained with small oscillation. Recently, in [15], E. E. Ovsyannikova and A. M. Gus'kov created a mathematical model of a rigid rotor suspended in a blood flow and supported by conical active magnetic bearings. They used the proportional-integral differential (PID) control, which takes into account the influence of hydrodynamic moments, which affect the rotor from the side of the blood flow, as well as external influences on the person. The experimental findings are reported, with a rotor speed range of 5000 to 12000 rpm and a placement error of less than 0.2 mm. Nguyen et al. introduced a control approach considering input and output constraints in the magnetic bearing system in [16] and [17]. The control restricts the rotor displacement in a certain range according to the system structure. In [18], modelling of a conical AMB structure for a complete support of 5-dof rotor system was reported by A. Katyayn and P. K. Agarwal, who improved the system's performance by creating the Interval type-2 fuzzy logic controller (IT2FLC) with an uncertain bound algorithm. This controller reduces the need for a precise system modeling while also allowing for the handling of parameter uncertainty. The simulation results show that the proposed controller outperforms the type-1 fuzzy logic controller in terms of transient responses.

In this paper, we examine the concept of conical magnetic bearings for both the radial and axial displacement control. The governing equations characterising the relationship between magnetic forces, air gaps, gyroscopic force, and control currents are used to build the nonlinear model of the conical magnetic bearing. The main contribution of the paper is that rotational motions are treated as disturbances and are handled by the Active Disturbance Rejection Control (ADRC) [19, 20] to stabilise the cone-shaped AMB system. ADRC was developed as an option that combines the easy applicability of conventional PID-type control methods with the strength of modern model-based approaches. The core of ADRC is an extended observer that treats actual disturbances and modelling uncertainty together, using only a very coarse process model to create a control loop. Because of the excellent abilities of ADRC, the paper also tackles the unwanted dynamics due to rotational motions, which are normally neglected in other related works. The ignorance might lead to system degradation due to a high operating speed resulting in strong coupling effects. The effectiveness of the proposed control structure for stabilising the rotor position and rejecting coupling-phenomenon-induced disturbance is numerically evaluated through comprehensive scenarios.

2. DYNAMIC MODELLING OF CONICAL MAGNETIC BEARINGS

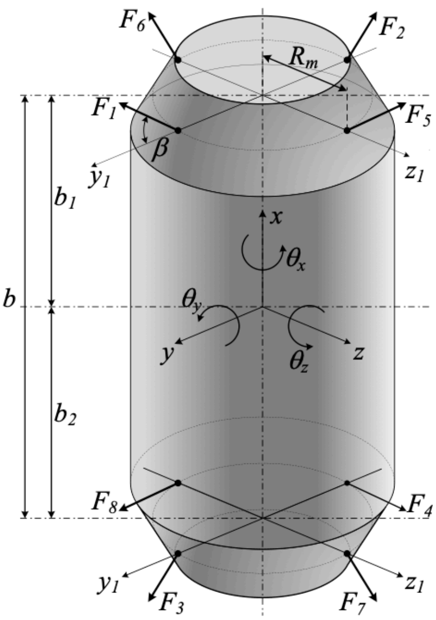

FIGURE 1. Model of a cone-shaped active magnetic bearing system.

Consider the simplified model of a conical magnetic bearing system as shown in Fig. 1. It is assumed that the rotor is rigid and its centre of mass and geometric centre are coincide. Furthermore, the assumptions of non-saturated circuit and negligible flux linkage between magnetic coils are made. R_m and β are the effective radius and inclined angle of the magnetic core, b_1 and b_2 are the distances between the two radical magnetic bearing and the centre of gravity of the rotor; F_j (j =1 to 8) are the magnetic forces produced by the stator and exerted on the rotor; (x, y, z) and $(\theta_x, \theta_y, \theta_z)$ are the displacement and angular coordinates defined with respect to the centre of mass. The cone-shaped active magnetic bearing system can be modelled as follows:

$$\begin{aligned} m\ddot{x} &= (F_1 + F_2 + F_5 + F_6)\sin\beta \\ &\quad - (F_3 + F_4 + F_7 + F_8)\sin\beta - mg. \\ m\ddot{y} &= (F_1 - F_2 + F_3 - F_4)cos\beta. \\ m\ddot{z} &= (F_5 - F_6 + F_7 - F_8)cos\beta. \\ J_d\ddot{\theta}_y &= [(F_6 - F_5)b_1 + (F_7 - F_8)b_2]\mathrm{cos}\beta \\ &\quad + (F_5 - F_6 + F_8 - F_7)R_m\sin\beta + J\dot{\theta}_x\dot{\theta}_z. \\ J_d\ddot{\theta}_z &= [(F_1 - F_2)b_1 + (F_4 - F_3)b_2]\mathrm{cos}\beta \\ &\quad + (F_2 - F_1 + F_3 - F_4)R_m\sin\beta + J\dot{\theta}_x\dot{\theta}_y \end{aligned} \tag{1}$$

where J is the moment of inertia of the rotor about the axis of rotation. The mass and moment of inertia of the rotor are m and J_d, respectively. We also consider the effect of the x-axis rotation on the other two axes.

Here, the first three equations in Eq. (1) are the kinematics of the rotor's transverse motion, while the last two equations represent the rotor's rotational dynamics. In addition, in the two rotational kinematics equations, there is an additional component of the feedback force. Suppose that when the rotor rotates rapidly if a force is applied to the y-axis (z-axis) that is sufficiently large to deflect the rotor from the axis of motion by a small angle, the rotor itself will also react back to a torque of the corresponding magnitude equal to $J\dot{\theta}_x\dot{\theta}_z$. Similarly, the component of gyro force

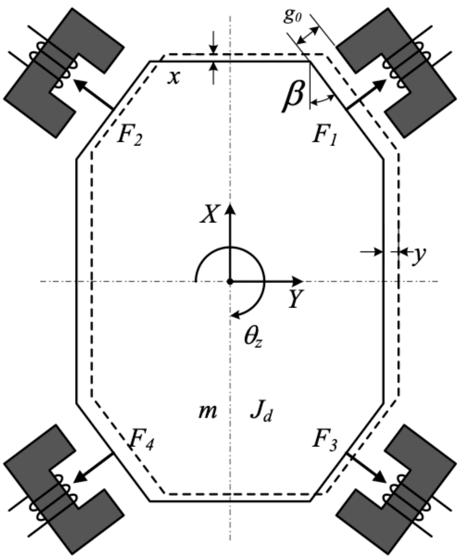

Figure 2. Simplified model of the cone-shaped AMB system.

along the z-axis is computed. In order to linearise, the dynamic equation (1), small motions of the rotor are considered. Fig. 2 shows the change of the air gap of the cone-shaped magnet, which is written as:

$$\begin{aligned} g_{y_{1,2}} &= g_o - x\sin\beta \pm (y + b_1\theta_z)\cos\beta \\ g_{y_{3,4}} &= g_o + x\sin\beta \pm (y - b_2\theta_z)\cos\beta \\ g_{z_{1,2}} &= g_o - x\sin\beta \pm (z + b_1\theta_y)\cos\beta \\ g_{z_{3,4}} &= g_o + x\sin\beta \pm (z + b_2\theta_y)\cos\beta \end{aligned} \tag{2}$$

where g_o is the steady-state nominal air gap. The magnetic force can be written regrading to he actual air gap and the current as:

$$\begin{aligned} F_{1,2} &= \frac{\mu_o A_p N^2 (I_{o_1} + i_{y_{1,2}})^2}{4{g_{y_{1,2}}}^2} \\ F_{3,4} &= \frac{\mu_o A_p N^2 (I_{o_2} + i_{y_{3,4}})^2}{4{g_{y_{3,4}}}^2} \\ F_{5,6} &= \frac{\mu_o A_p N^2 (I_{o_1} + i_{z_{1,2}})^2}{4{g_{z_{1,2}}}^2} \\ F_{7,8} &= \frac{\mu_o A_p N^2 (I_{o_2} + i_{z_{3,4}})^2}{4{g_{z_{3,4}}}^2} \end{aligned} \tag{3}$$

where $\mu_o (= 4\pi \times 10^{-7} H/m)$ is the permeability of free space; $A_p = A/cos\beta$, A is the cross-sectional area, N is the number of coil turns; $i_{q_j} (j = \overline{1,4} \& q = y, z)$ is the control current of each magnet; I_{o_1} and I_{o_2} are the bias currents in the upper and lower bearing. Assume that the current change and the displacement of the rotor are small relative to the bias current I_o and the nominal air gap. Apply Eq. (2) to Eq. (3) and use the Taylor expansion series to obtain the magnetic force, which is linearised as:

$$\begin{aligned} F_{1,2} &= F_{o_1} + K_{i_1} i_{y_{1,2}} + K_{q_1} x \sin\beta \\ &\quad \pm K_{q_1}(y + b_1\theta_z)\cos\beta \\ F_{3,4} &= F_{o_2} + K_{i_2} i_{y_{3,4}} + K_{q_2} x \sin\beta \\ &\quad \pm K_{q_2}(y - b_2\theta_z)\cos\beta \\ F_{5,6} &= F_{o_1} + K_{i_1} i_{z_{1,2}} + K_{q_1} x \sin\beta \\ &\quad \pm K_{q_1}(z - b_1\theta_y)\cos\beta \\ F_{7,8} &= F_{o_2} + K_{i_2} i_{z_{3,4}} + K_{q_2} x \sin\beta \\ &\quad \pm K_{q_2}(z + b_2\theta_y)\cos\beta \end{aligned} \tag{4}$$

where $F_{oj} = \frac{\mu_o A_p N^2 {I_{oj}}^2}{4{g_o}^2}, j = 1,2$ are the steady-state magnetic forces and $k_{qj} = \frac{2F_{oj}}{g_o}, k_{ij} = \frac{2F_{oj}}{I_{oj}}, j = 1,2$ are the position and current stiffnesses, respectively.

From the combination of Eqs. (1) and (4), the linear differential equation showing the kinematics of the 5 degrees of freedom conical-AMB drive system can be rewritten as:

$$\mathbf{M}_b \ddot{\mathbf{q}}_b + \mathbf{K}_b \mathbf{q}_b = \mathbf{K}_{ibm} \mathbf{i}_m + G\dot{\mathbf{q}}_b \tag{5}$$

where

$$\mathbf{q}_b = \{\, x, y, z, \theta_y, \theta_z \}^{\,T}$$

$$\mathbf{i}_m = \{\, i_{y_1}, i_{y_2}, i_{y_3}, i_{y_4}, i_{z_1}, i_{z_2}, i_{z_3}, i_{z_4} \}^{\,T}$$

$$\mathbf{K}_b = \begin{bmatrix} -K_{xx} & 0 & 0 & 0 & 0 \\ 0 & -K_{yy} & 0 & 0 & -K_{y\theta_z} \\ 0 & 0 & -K_{zz} & -K_{z\theta_y} & 0 \\ 0 & 0 & -K_{\theta_y z} & -K_{\theta_y\theta_y} & 0 \\ 0 & -K_{\theta_z y} & 0 & -K_{\theta_z\theta_z} & 0 \end{bmatrix}$$

$$G = \begin{bmatrix} 0 & 0 & 0 & 0 & 0 \\ 0 & 0 & 0 & 0 & 0 \\ 0 & 0 & 0 & 0 & 0 \\ 0 & 0 & 0 & 0 & J\dot{\theta}_x \\ 0 & 0 & 0 & J\dot{\theta}_x & 0 \end{bmatrix}$$

$$\mathbf{K}_{ibm} = \begin{bmatrix} K_{i_1}\mathrm{S}\beta & K_{i_1}\mathrm{C}\beta & 0 & 0 & K_{i_1}\sigma \\ K_{i_1}\mathrm{S}\beta & -K_{i_1}\mathrm{C}\beta & 0 & 0 & -K_{i_1}\sigma \\ -K_{i_2}\mathrm{S}\beta & K_{i_2}\mathrm{C}\beta & 0 & 0 & K_{i_2}\gamma \\ -K_{i_2}\mathrm{S}\beta & -K_{i_2}\mathrm{C}\beta & 0 & 0 & -K_{i_2}\gamma \\ K_{i_1}\mathrm{S}\beta & 0 & K_{i_1}\mathrm{C}\beta & K_{i_1}\alpha & 0 \\ K_{i_1}\mathrm{S}\beta & 0 & -K_{i_1}\mathrm{C}\beta & -K_{i_1}\alpha & 0 \\ -K_{i_2}\mathrm{S}\beta & 0 & K_{i_2}\mathrm{C}\beta & K_{i_2}\gamma & 0 \\ -K_{i_2}\mathrm{S}\beta & 0 & -K_{i_2}\mathrm{C}\beta & -K_{i_2}\gamma & 0 \end{bmatrix}$$

$$\mathbf{M}_b = \begin{bmatrix} m & 0 & 0 & 0 & 0 \\ 0 & m & 0 & 0 & 0 \\ 0 & 0 & m & 0 & 0 \\ 0 & 0 & 0 & J_d & 0 \\ 0 & 0 & 0 & 0 & J_d \end{bmatrix}$$

$$K_{xx} = 4\,(K_{q_1} + K_{q_2})\,\mathrm{S}^2\beta$$

$$K_{yy} = K_{zz} = 2\mathrm{C}^2\beta\,(K_{q_1} + K_{q_2})$$

$$K_{y\theta_z} = K_{z\theta_y} = 2\mathrm{C}^2\beta\,(K_{q_1} b_1 + K_{q_2} b_2)$$

$$
\begin{aligned}
K_{\theta_y z} &= 2\mathrm{C}^2\beta\left(K_{q_1}b_1 + K_{q_2}b_2\right)\\
&\quad + \mathrm{S}(2\beta)R_m\left(K_{q_1} - K_{q_2}\right)\\
K_{\theta_z y} &= 2\mathrm{C}^2\beta\left(K_{q_1}b_1 - K_{q_2}b_2\right)\\
&\quad - \mathrm{S}(2\beta)R_m\left(K_{q_1} - K_{q_2}\right)\\
K_{\theta_y\theta_y} &= 2\mathrm{C}^2\beta\left(K_{q_1}{b_1}^2 - K_{q_2}{b_2}^2\right)\\
&\quad + \mathrm{S}(2\beta)R_m\left(K_{q_1}b_1 + K_{q_2}b_2\right)\\
K_{\theta_z\theta_z} &= 2\mathrm{C}^2\beta\left(K_{q_1}{b_1}^2 + K_{q_2}{b_2}^2\right)\\
&\quad - \mathrm{S}(2\beta)R_m\left(K_{q_1}b_1 + K_{q_2}b_2\right)\\
\alpha &= b_1\mathrm{C}\beta + R_m\mathrm{S}\beta; \sigma = b_1\mathrm{C}\beta - R_m\mathrm{S}\beta\\
\gamma &= b_2\mathrm{C}\beta - R_m\mathrm{S}\ \beta
\end{aligned}
$$

Here, $\mathbf{q}_b$ is the displacement vector defined in the mass centre coordinates; $\mathbf{i}_m$ is the control current vector and $\mathbf{M}_b$, $\mathbf{K}_b$ and $\mathbf{K}_{ibm}$ are the mass, position stiffness, and current stiffness matrices, respectively. As can be observed, the system's equation is complicated and coupled because the components outside the main diagonal of the matrices, $\mathbf{K_b}$, $\mathbf{K}_{ibm}$ and $\mathbf{G}$ are non-zero. Due to this characteristic, conventional linear control rules cannot be applied directly to each motion direction. As a result, the Active Disturbance Rejection Control (ADRC) algorithm is employed to handle the coupling effects by taking these effects as system disturbances.

3. Control system design

The conical AMB system is naturally unstable, a closed-loop control is required to stabilise the rotor position. The control current of the system can be calculated through the control structure "different driving mode", which is shown in Fig. 3.

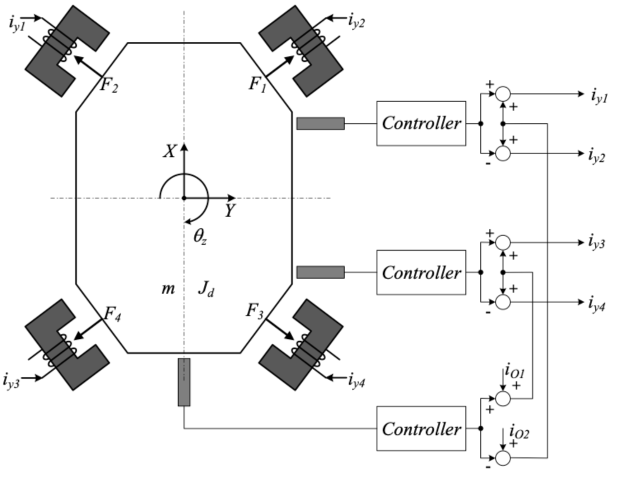

Figure 3. Conceptual control loop of the cone-shaped active magnetic bearings.

The main principle of the aforementioned structure: where controlling the position of the rotor according to the $Y - axis$ and $Z - axis$, the magnet pairs are in the poles that are opposite each other. For example, i_{y_1} and i_{y_2} magnets, as well as, i_{y_3} and i_{y_4}, i_{z_1} and i_{z_2}, i_{z_3} and i_{z_4} are similarly controlled by this structure. Here, the magnet in each pair is controlled by the sum of the bias current and control current, and the other with the difference of the bias current and control current. This means that when the rotor is displaced from its equilibrium position, the "different driving mode" controls the pairs of magnets, whereas when the rotor is in its equilibrium position, only the bias current is present on each pair of the magnets. When the rotor deviates from the equilibrium position, the current through the pairs of magnets is written as in the following equation:

$$
\begin{bmatrix} i_{y_1}\\ i_{y_2}\\ i_{y_3}\\ i_{y_4}\\ i_{z_1}\\ i_{z_2}\\ i_{z_3}\\ i_{z_4}\end{bmatrix}
=
\begin{bmatrix} I_{o_1}\\ I_{o_1}\\ I_{o_2}\\ I_{o_2}\\ I_{o_1}\\ I_{o_1}\\ I_{o_2}\\ I_{o_2}\end{bmatrix}
+
\begin{bmatrix}
1 & 0 & 0 & 0 & -1\\
-1 & 0 & 0 & 0 & -1\\
0 & 1 & 0 & 0 & 1\\
0 & -1 & 0 & 0 & 1\\
0 & 0 & 1 & 0 & -1\\
0 & 0 & 0 & -1 & -1\\
0 & 0 & 0 & 1 & 1\\
0 & 0 & 0 & -1 & 1
\end{bmatrix}
\begin{bmatrix} I_{yt}\\ I_{yd}\\ I_{zt}\\ I_{zd}\\ I_x\end{bmatrix}
\tag{6}
$$

where $\mathbf{I}_o = [I_{o_1}, I_{o_1}, I_{o_2}, I_{o_2}, I_{o_1}, I_{o_1}, I_{o_2}, I_{o_2}]^T$ is the bias current. At steady-state, consider $\mathbf{I}_o = 0$, $\mathbf{i}_r = [I_{yt}, I_{yd}, I_{zt}, I_{zd}, I_x]^T$ is the x, y, and z axes' virtual control current. I_x is the virtual control current of x-axes. The virtual control current in the upper half of the y and z axes is (I_{yt}, I_{zt}) , whereas the virtual control current in the bottom half is (I_{yd}, I_{zd}).

$$
\mathbf{H} = \begin{bmatrix}
1 & -1 & 0 & 0 & 0 & 0 & 0 & 0\\
0 & 0 & 1 & -1 & 0 & 0 & 0 & 0\\
0 & 0 & 0 & 0 & 1 & 0 & 0 & 0\\
0 & 0 & 0 & 0 & 0 & -1 & 1 & -1\\
-1 & -1 & 1 & 1 & -1 & -1 & 1 & 1
\end{bmatrix}^T
$$

In this case, Eq. (5) can be rewritten as:

$$
\mathbf{M}_b\ddot{\mathbf{q}}_b - \mathbf{G}\dot{\mathbf{q}}_b + \mathbf{K}_b\mathbf{q}_b = \mathbf{K}_{ibm}\mathbf{H}\mathbf{i}_r \tag{7}
$$

Since the control is performed in the bearing coordinates, rewriting the equations of motion in bearing coordinates utilising the relationship between the mass-centre coordinates $(x, y, z, \theta_y, \theta_z)$ and the bearing coordinates (x, y_1, y_2, z_1, z_2), given by:
$\mathbf{q}_b = \{\ x, y, z, \theta_y, \theta_z\}\ ^T$ and $\mathbf{q}_{se} = \{\ x, y_1, y_2, z_1, z_2\}\ ^T$
$\mathbf{q}_{se} = \mathbf{T}\mathbf{q}_b$ with $\mathbf{T}$ is the coordinate transfer matrix

$$
\mathbf{T} = \begin{bmatrix}
1 & 0 & 0 & 0 & 0\\
0 & 1 & 0 & 0 & b_1\\
0 & 1 & 0 & 0 & -b_2\\
0 & 0 & 1 & -b_1 & 0\\
0 & 0 & 1 & b_2 & 0
\end{bmatrix}
$$

Eq. (1) shows that the inter-channel effect occurs at $\mathbf{K}_b$ and $\mathbf{K}_{ibm}\mathbf{H}$ because the major non-diagonal components are not zero. The $\mathbf{K}_b$ and $\mathbf{K}_{ibm}\mathbf{H}$ are invertible. The following control structure is used to eliminate the interstitial component:

$$
\mathbf{i}_r = (\mathbf{K}_{ibm}\mathbf{H})^{-1}(\mathbf{v} + \mathbf{K}_b\mathbf{T}^{-1}\mathbf{q}_{se}) \tag{8}
$$

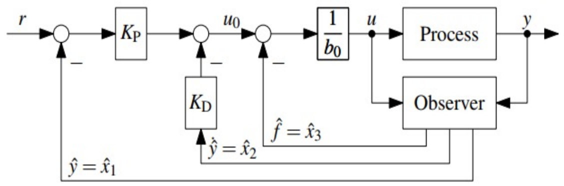

Figure 4. Control loop structure with active disturbance rejection control (ADRC).

Eq. (7) can be rewritten as:

$$\mathbf{M}_b\ddot{\mathbf{q}}_b - \mathbf{G}\dot{\mathbf{q}}_b = \mathbf{v} \tag{9}$$

where $\mathbf{v}$ is the new control signal's vector. The interstitial component has been removed in the control channels (x, y, z) leaving just the interstitial component in the control channel (θ_y, θ_z) owing to the gyroscope force.

The original model of the magnetic bearing is a complex, multivariable nonlinear system, through the process of linearity and decoupling, we have the linear form of the system shown in Eq. (9) with 5 inputs and 5 outputs. The full form of Eq. (9) is shown as follows:

$$\begin{cases} m\,\ddot{x} = v_1 \\ m\,\ddot{y} = v_2 \\ m\,\ddot{z} = v_3 \\ J_d\,\ddot{\theta}_y + J\,\dot{\theta}_x\,\dot{\theta}_z = v_4 \\ J_d\,\ddot{\theta}_z + J\,\dot{\theta}_x\,\dot{\theta}_y = v_5 \end{cases} \tag{10}$$

Remark: It is noted that the first three equations of Eq. (10) characterise the transnational motions and can be readily stabilized using v_1, v_2, and v_3. The last two equation indicate coupling mechanism related to the rotational motion of the rotor that is normally ignored. In practice, the magnetic bearing is normally employed to operate in high speed range, hence rotational motion effects can not be neglected.

In this section, the ADRC controller will be used to remove the remaining coupling components as well as to stabilise the control object. An ADRC controller is used for each input and output pair $(x, v_1), (y, v_2), (z, v_3), (\theta_y, v_4), (\theta_z, v_5)$. In ADRC design, $f(t)$ is unknown and is considered as a "generalized disturbance", and b_0 is the available information concerning the model. The according structure of the control loop with ADRC is presented in Fig. 4. The fundamental idea of ADRC is to implement an extended state observer (ESO) that provides an estimate, $\hat{f}(t)$, such that we can compensate the impact of $f(t)$ on our system. The equation for the extended state observer is given as:

$$\begin{aligned} \begin{pmatrix} \dot{\hat{x}}_1(t) \\ \dot{\hat{x}}_2(t) \\ \dot{\hat{x}}_3(t) \end{pmatrix} &= \begin{pmatrix} 0 & 1 & 0 \\ 0 & 0 & 1 \\ 0 & 0 & 0 \end{pmatrix} \begin{pmatrix} \hat{x}_1(t) \\ \hat{x}_2(t) \\ \hat{x}_3(t) \end{pmatrix} \\ &+ \begin{pmatrix} 0 \\ b_0 \\ 0 \end{pmatrix} u(t) + \begin{pmatrix} l_1 \\ l_2 \\ l_3 \end{pmatrix} (y(t) - \hat{x}_1(t)) \\ &= \underbrace{\begin{pmatrix} -l_1 & 1 & 0 \\ -l_2 & 0 & 1 \\ -l_3 & 0 & 0 \end{pmatrix}}_{A-LC} \begin{pmatrix} \hat{x}_1(t) \\ \hat{x}_2(t) \\ \hat{x}_3(t) \end{pmatrix} \\ &+ \underbrace{\begin{pmatrix} 0 \\ b_0 \\ 0 \end{pmatrix}}_{B} u(t) + \begin{pmatrix} l_1 \\ l_2 \\ l_3 \end{pmatrix} y(t) \end{aligned} \tag{11}$$

where $\hat{x}_1(t) = \hat{y}(t)$; $\hat{x}_2(t) = \dot{\hat{y}}(t)$; $\hat{x}_3(t) = \hat{f}(t)$. Removing the unknown components is done through the following control law:

$$\begin{aligned} \ddot{y}(t) &= (f(t) - \hat{f}(t)) + u_0(t) \approx u_0(t) \\ &\approx K_P.((r(t) - y(t)) - K_D.\dot{y}(t)) \end{aligned} \tag{12}$$

where r is the setpoint. In order to work properly, observer parameters, l_1, l_2, l_3, in Eq. (11) still have to be determined. According to [20], the ADRC's parameters can be chosen to tune the closed-loop to a critically damped behaviour and a desired 2% settling time T_{settle}. The tuning procedure is summarised as follows:

$$\begin{aligned} &K_p = \left(s^{CL}\right)^2, K_D = -2.s^{CL} \\ &l_1 = -3.s^{ESO}, l_2 = 3.\left(s^{ESO}\right)^2, l_3 = \left(s^{ESO}\right)^3 \end{aligned} \tag{13}$$

with $s^{CL} = -\frac{6}{T_{settle}}$ being the negative-real double closed-loop pole.

$s^{ESO} \approx (3...10).s^{CL}$ is the observer pole. Using the ADRC controller to calculate the variable x, y and z are calculated similarly:

$$\begin{aligned} \ddot{x} &= \underbrace{(\frac{1}{m}.d(t) + \Delta b.u(t))}_{f(t)} + b_{01}v_1 \\ &= f(t) + b_{01}.v_1(t) \\ v_1(t) &= K_{P1}.((r(t) - \hat{x}(t)) - K_{D1}.\dot{\hat{x}}(t)) \end{aligned} \tag{14}$$

For equations containing the two variables (θ_y and θ_z), which have an interleaved component between the two equations. Because the interleaved component is unknown, the extended observer can be used to estimate and analyse it, using the ADRC controller with variable θ_y, as follows:

$$\begin{aligned} \ddot{\theta}_y &= (\frac{1}{J}d(t) + \Delta b.v_4(t) + J\theta_x\theta z) + b_{04}v_4 \\ &= f(t) + b_{04}.v_4(t) \\ b_{04} &= \frac{1}{J} \\ v_4(t) &= K_{P4}.((r(t) - \hat{\theta}_y(t)) - K_{D4}.\dot{\hat{\theta}}_y(t)) \end{aligned} \tag{15}$$

Name	Symbol
$b_{01} = b_{02} = b_{03}$	$1/m$
$b_{04} = b_{05}$	$1/J$
T_{settle}	$0.1\ (s)$
s^{CL}	-60
$K_{Pi}\ (i = 1, \dots, 5)$	3600
$K_{Di}\ (i = 1, \dots, 5)$	120
s^{ESO}	-420
$l_{1i}\ (i = 1, \dots, 5)$	1260
$l_{2i}\ (i = 1, \dots, 5)$	529200
$l_{3i}\ (i = 1, \dots, 5)$	74088000

TABLE 1. Controller parameters.

4. NUMERICAL SIMULATIONS

In this section, we consider two scenarios to evaluate the effectiveness of using the ADRC controller in the case of variable speed rotation and rotor load disturbance.

Bearing design parameters	Value
Radial air gap g_0	0.5 mm
Cross-sectional area A	18*10 mm
Inclined angle β	10^o
Magnetic coils N	300 turns
Resistance R	2 Ω
Inductance of wire L_0	20 mH
Rotor mass M	1.86 Kg
Moment of inertia J_d	0.00647 kgm^2
Moment of inertia J_p	0.00121 kgm^2
Bias current I_{01}, I_{02}	1.6 A,1 A
Bearing span b_1, b_2	81.7 mm,71.6 mm

TABLE 2. System parameters.

4.1. SIMULATION SCENARIO 1:

We design an ADRC controller with a rotor rotation speed of 3000 rpm. The initial values of the rotor's centre of mass position are: $x_0 = 0.25.10^{-3}; y_0 = 0.2.10^{-3}; z_0 = 0.125.10^{-3}; \theta_y = 0.1.10^{-3}; \theta_z = 0.2.10^{-3}$. Select the coefficients of the ADRC as follows $s^{CL} = -\frac{6}{0.1}, s^{ESO} = 7s^{CL}, K_P = (s^{CL})^2, K_D = -2s^{CL}, l_1 = -3s^{ESO};\ l_2 = 3\left(s^{ESO}\right)^2, l_3 = -(s^{ESO})^3$.

The position of the centre of mass and the deflection angle of the rotor return to the equilibrium position after a time interval of 0.1 seconds and there is no overshoot in Fig. 5 and Fig. 6. From Fig. 7, initially, when the rotor position deviates from the equilibrium position, a control current is generated to bring the rotor back to the equilibrium position. After the rotor is in the equilibrium position, the control current is zero so that the bias currents I_{01} and I_{02} keep the rotor in this equilibrium state. The impact force of the magnet is shown in Fig. 8 as having a significant value at first to bring the rotor to equilibrium, but once the rotor returns to equilibrium, the force is kept stable at the values F_{01} and F_{02}. From the above results, it can be concluded that the controller is designed to completely satisfy the requirements.

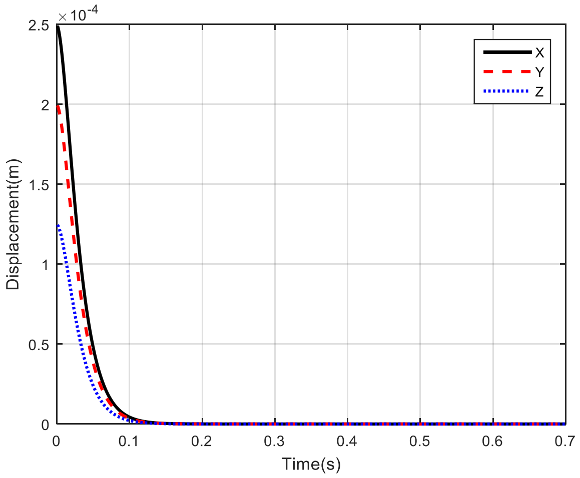

FIGURE 5. Response to the position of the x, y, z axes.

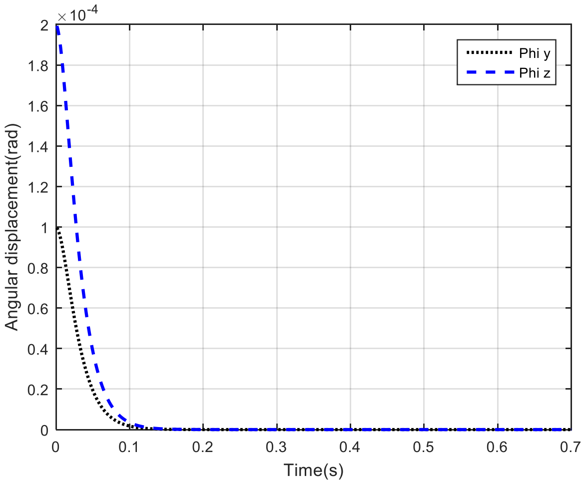

FIGURE 6. The position of the axis angle θ_y, θ_z.

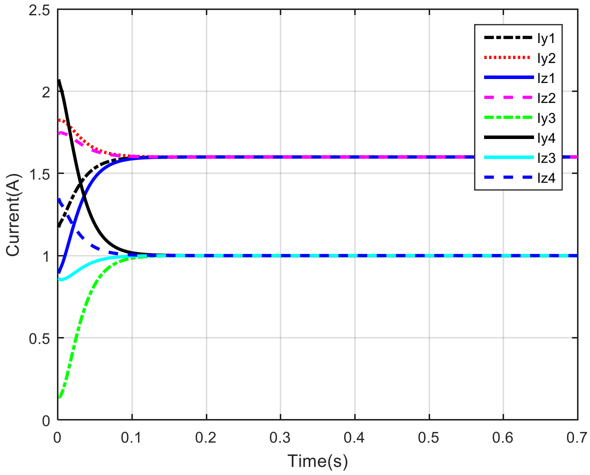

FIGURE 7. Control current response.

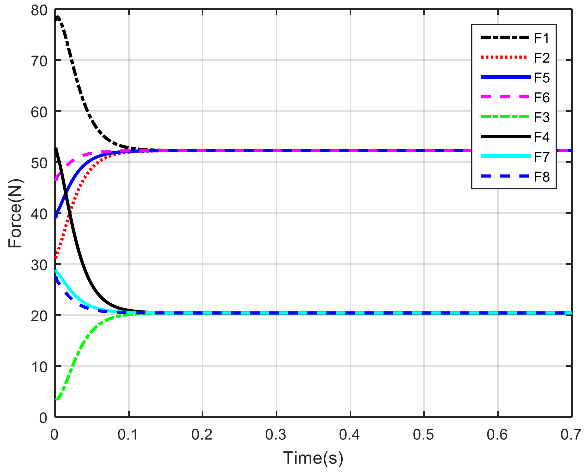

Figure 8. Impact force of electromagnets.

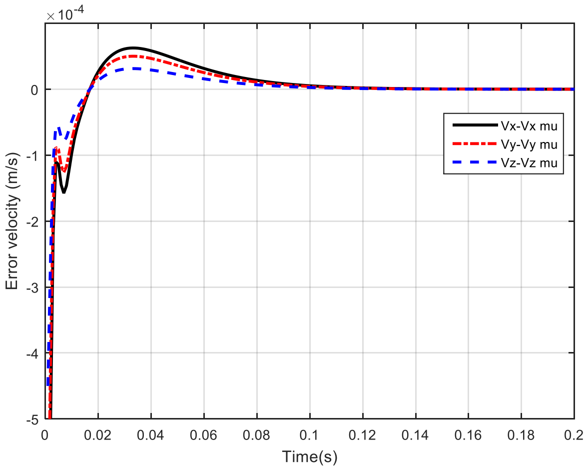

Figure 9. Velocity deviation of x, y, z axes according to observer.

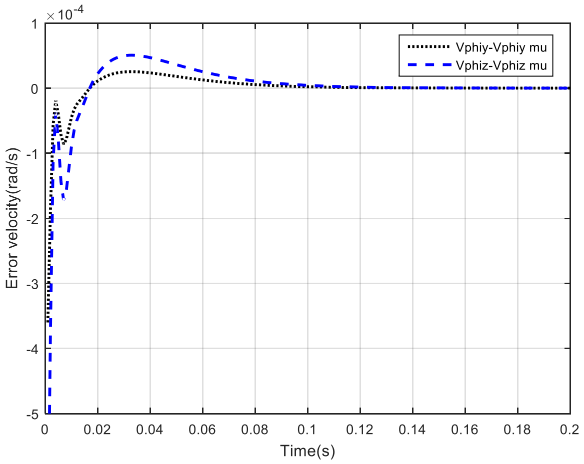

Figure 10. Velocity deviation of θ_y, θ_z axes according to observer.

Based on Fig. 9 and Fig. 10, the observer satisfied the requirements, and the estimated velocity values were near to the real velocity value after 0.1 s.

4.2. Simulation scenario 2:

The rotor speed will be changed to 12000 rpm to evaluate the controllability of the controller when the rotor is in the high-speed region, the initial value of the rotor's centre of mass is: $x_0 = 0.25.10^{-3}; y_0 = 0.2.10^{-3}; z_0 = 0.125.10^{-3}; \theta_y = 0.1.10^{-3}; \theta_z = 0.2.10^{-3}$.

The simulation results on the x, y, and z axes are identical to the first simulation scenario, as shown in Fig. 12, where the angular position responses of the axes θ_y, θ_z have an undershoot and the response time has been increased to 0.2 seconds. Only the θ_y and θ_z axes are impacted when the rotor rotates at high speeds, but it soon returns to equilibrium. The suggested controller takes into account the rotor speed factor and demonstrates its capacity to function well in the high-speed region.

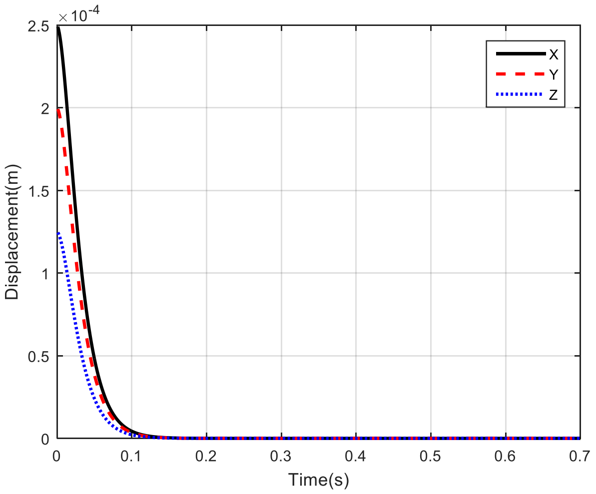

Figure 11. Response to the position of the x, y, z axes.

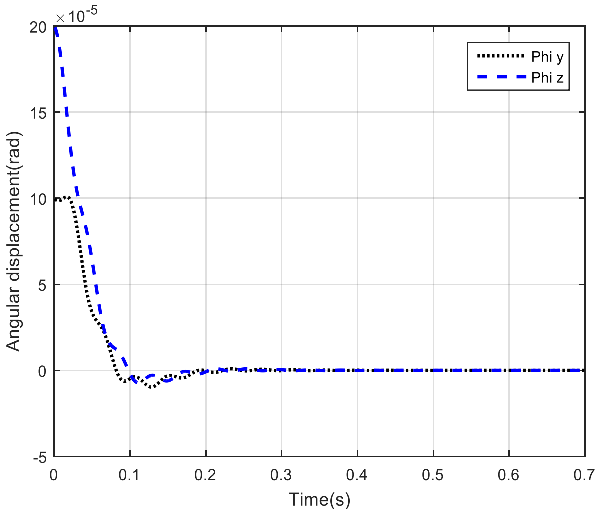

Figure 12. The position of the axis angle θ_y, θ_z.

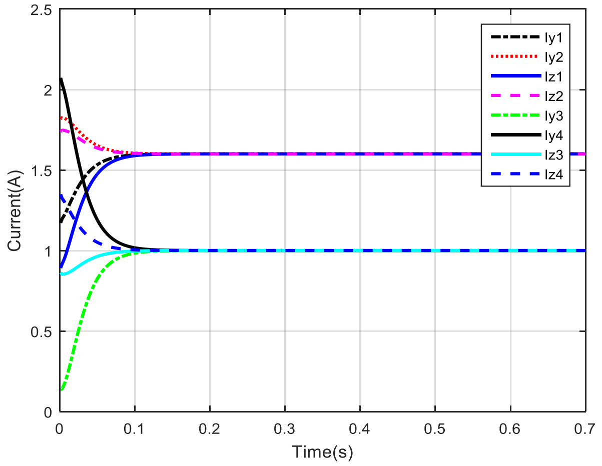

Figure 13. Control current response.

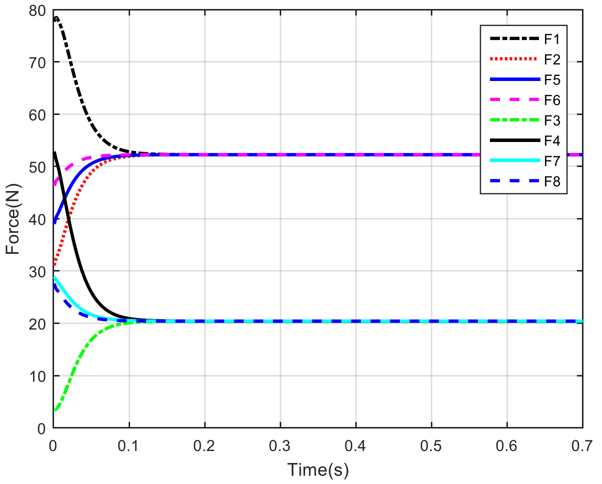

Figure 14. Impact force of electromagnets.

5. Conclusions

In the paper, we consider the cone-shaped magnetic bearing, which is characterised as a class of underactuated and strongly coupled systems. Based on control current distribution, the coupling mechanism in electrical sub-system is solved. Subsequently, an active disturbance control is adopted to tackle the rotational-motion-induced disturbance acting on the system. The simulations are carried out proving that the proposed control can effectively bring the the rotor to equilibrium. The results also indicate that the coupling effects from low to high rotational speeds do not have a noticeable impact on the transnational motions of the rotor. In the future, experimental study will be carried out.

Acknowledgements

This research is funded by the Hanoi University of Science and Technology (HUST) under project number T2021-PC-001.

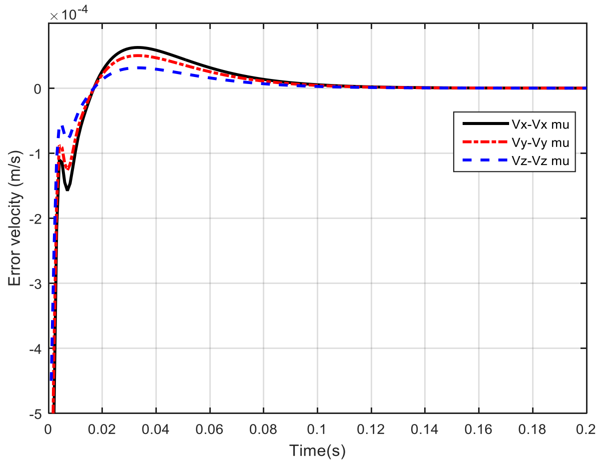

Figure 15. Velocity deviation of x, y, z axes according to observer.

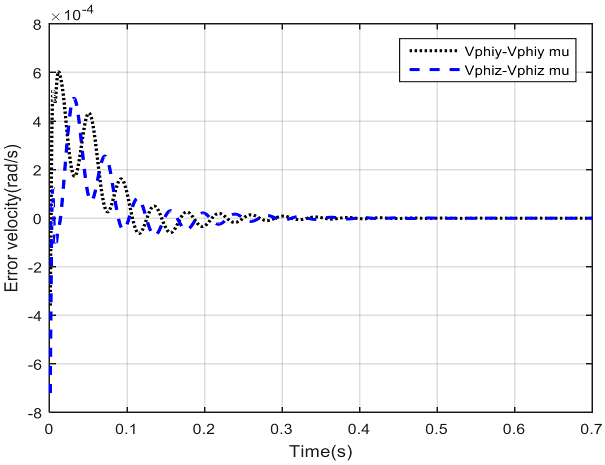

Figure 16. Velocity deviation of θ_y, θ_z axes according to observer.

References

[1] C. R. Knospe. Active magnetic bearings for machining applications. *Control Engineering Practice* **15**(3):307–313, 2007. `https://doi.org/10.1016/j.conengprac.2005.12.002`.

[2] W. Ding, L. Liu, J. Lou. Design and control of a high-speed switched reluctance machine with conical magnetic bearings for aircraft application. *IET Electric Power Applications* **7**(3):179–190, 2013. `https://doi.org/10.1049/iet-epa.2012.0319`.

[3] P. Imoberdorf, C. Zwyssig, S. D. Round, J. Kolar. Combined radial-axial magnetic bearing for a 1 kW, 500,000 rpm permanent magnet machine. In *APEC 07 - Twenty-Second Annual IEEE Applied Power Electronics Conference and Exposition*, pp. 1434–1440. 2007. `https://doi.org/10.1109/APEX.2007.357705`.

[4] J. X. Shen, K. J. Tseng, D. M. Vilathgamuwa. A novel compact PMSM with magnetic bearing for artificial heart application. *IEEE Transactions on Industry Applications* **36**(4):1061–1068, 2000. `https://doi.org/10.1109/28.855961`.

[5] M. D. Noh, S. R. Cho, J. H. Kyung, et al. Design and implementation of a fault-tolerant magnetic bearing

system for turbo-molecular vacuum pump. *IEEE/ASME Transactions on Mechatronics* **10**(6):626–631, 2005. `https://doi.org/10.1109/TMECH.2005.859830`.

[6] B. Han, S. Zheng, Y. Le, S. Xu. Modeling and analysis of coupling performance between passive magnetic bearing and hybrid magnetic radial bearing for magnetically suspended flywheel. *IEEE Transactions on Magnetics* **49**(10):5356–5370, 2013. `https://doi.org/10.1109/TMAG.2013.2263284`.

[7] D. H. Nguyen, M. L. Nguyen, T. L. Nguyen. Decoupling Control of a Disc-type Rotor Magnetic Bearing. *The International Journal of Integrated Engineering* **13**(5):247–261, 2021. `https://doi.org/10.30880/ijie.2021.13.05.026`.

[8] A. H. Slocum. Introduction to Precision Machine Design. *Precision Machine Design* pp. 390–399, 1992.

[9] H. S. Jeong, C. S. Kim. Modeling and Control of Active Magnetic Bearings, 1994.

[10] S. Xu, J. Fang. A Novel Conical Active Magnetic Bearing with Claw Structure. *IEEE Transactions on Magnetics* **50**(5), 2014. `https://doi.org/10.1109/TMAG.2013.2295060`.

[11] A. Mohamed, F. Emad. Conical magnetic bearings with radial and thrust control. In *Proceedings of the 28th IEEE Conference on Decision and Control*, pp. 554–561. 1989. `https://doi.org/10.1109/CDC.1989.70176`.

[12] C. W. Lee, H. S. Jeong. Dynamic modeling and optimal control of cone-shaped active magnetic bearing systems. *Control Engineering Practice* **4**(10):1393–1403, 1996. `https://doi.org/10.1016/0967-0661(96)00149-9`.

[13] J. Fang, C. Wang, J. Tang. Modeling and analysis of a novel conical magnetic bearing for vernier-gimballing magnetically suspended flywheel. *Proceedings of the Institution of Mechanical Engineers, Part C: Journal of Mechanical Engineering Science* **228**(13):2416–2425, 2014. `https://doi.org/10.1177/0954406213517488`.

[14] S. J. Huang, L. C. Lin. Fuzzy modeling and control for conical magnetic bearings using linear matrix inequality. *Journal of Intelligent and Robotic Systems: Theory and Applications* **37**(2):209–232, 2003. `https://doi.org/10.1023/A:1024137007918`.

[15] E. E. Ovsyannikova, A. M. Gus'kov. Stabilization of a Rigid Rotor in Conical Magnetic Bearings. *Journal of Machinery Manufacture and Reliability* **49**(1):8–15, 2020. `https://doi.org/10.3103/S1052618820010100`.

[16] D. H. Nguyen, T. L. Nguyen, M. L. Nguyen, H. P. Nguyen. Nonlinear control of an active magnetic bearing with output constraint. *International Journal of Electrical and Computer Engineering (IJECE)* **8**(5):3666, 2019. `https://doi.org/10.11591/ijece.v8i5.pp3666-3677`.

[17] D. H. Nguyen, T. L. Nguyen, D. C. Hoang. A non-linear control method for active magnetic bearings with bounded input and output. *International Journal of Power Electronics and Drive Systems* **11**(4):2154–2163, 2020. `https://doi.org/10.11591/ijpeds.v11.i4.pp2154-2163`.

[18] A. Katyayn, P. K. Agarwal. Type-2 fuzzy logic controller for conical amb-rotor system. In *2017 4th International Conference on Power, Control & Embedded Systems (ICPCES)*, pp. 1–6. 2017. `https://doi.org/10.1109/ICPCES.2017.8117616`.

[19] J. Han. From PID to active disturbance rejection control. *IEEE Transactions on Industrial Electronics* **56**(3):900–906, 2009. `https://doi.org/10.1109/TIE.2008.2011621`.

[20] G. Herbst. A simulative study on active disturbance rejection control (ADRC) as a control tool for practitioners. *Electronics* **2**(3):246–279, 2013. `https://doi.org/10.3390/electronics2030246`.

Acta Polytechnica **62**(4):488–497, 2022
`https://doi.org/10.14311/AP.2022.62.0488`

A COMPARATIVE STUDY OF FERROFLUID LUBRICATION ON DOUBLE-LAYER POROUS SQUEEZE CURVED ANNULAR PLATES WITH SLIP VELOCITY

Niru C. Patel[a], Jimit R. Patel[a,*], Gunamani M. Deheri[b]

[a] *Charotar University of Science and Technology (CHARUSAT), P. D. Patel Institute of Applied Sciences, Department of Mathematical Sciences, CHARUSAT campus, Changa 388 421, Gujarat, India*

[b] *Sardar Patel University, Department of Mathematics, V. V. Nagar 388 120, Anand, Gujarat, India*

[*] corresponding author: `patel.jimitphdmarch2013@gmail.com`

Abstract.

This article makes an effort to present a comparative study on the performance of a Shliomis model-based ferrofluid (FF) lubrication of a porous squeeze film in curved annular plates taking slip velocity into account. The modified Darcy's law has been adopted to find the impact of the double-layered porosity, while the slip velocity effect has been calculated according to Beavers and Joseph's slip conditions. The modified Reynolds equation for the double-layered bearing system is solved to compute a dimensionless pressure profile and load-bearing capacity (LBC). The graphical results of the study reveal that the LBC increases in the case of magnetization, volume concentration and upper plate's curvature parameter while it decreases with other parameters for both the film thickness profile. A comparative study suggests that the exponential film thickness profile is more suitable to enhance LBC for the annular plates lubricated by ferrofluid, including the presence of a slip. The study shows that the slip model performed quite well and there is a potential for improving the performance efficiency. Besides, multiple methods have been presented to enhance the performance of the above mentioned bearing system by selecting various combinations of parameters governing the system.

Keywords: Shliomis model, curved annular plates, double-layered porous, slip velocity, exponential and hyperbolic film profile, ferrofluid.

1. Introduction

Porous materials seem to be ubiquitous and play a notable role in many aspects of day-to-day life. They are extensively used in various areas, such as energy management, vibration automotive, heat insulation, processes of sound, turbine industries and fluid filtration.

Due to the phenomenon known as self-lubrication, the porous bearing has a porous film filled with some amount of lubricants so that it does not require more lubrication throughout the life period of the bearing. The lubricant comes out of the porous layer and is deposited between the annular plates to inhibit friction and wear, as well as withstanding the original load applied to the annular plates. Therefore, the impact of lubrication due to the double porous layer is better than that of the single porous layer. Due to the remarkable mechanical properties and wide applications of the annular plates, many researchers have been focused on analysing annular bearing systems, such as Lin [1], Shah and Bhat [2], Bujurke et al. [3], Deheri et al. [4], Fatima et al. [5] and Hanumangowda et al. [6].

Also, numerous studies (Ting [7], Gupta et al. [8], Bhat and Deheri [9], Shah et al. [10], Shimpi and Deheri [11], Patel and Deheri [12], Rao and Agarwal [13], Vasanth et al. [14] and Shah et al. [15]) have been carried out to examine the impact of porosity on the effectivity of annular plates.

A synthetic fluid, namely "ferrofluid", is a mixture of colloidal dispersions containing ferromagnetic particles in a liquid carrier. Besides being used in elastic dampers to reduce noise, FFs are used in cooling and heating cycles, long-term sealing of rotating shafts, and reducing unwanted resonances in loudspeakers. In the last four decades, several investigators (Kumar et al. [16], Sinha et al. [17], Shah and Bhat [18], Patel and Deheri [19], Shah and Shah [20] and Munshi et al. [21]) have worked on a FF lubrication theory to examine the behaviour of various bearing systems.

Alternative physical boundary conditions were proposed in the advanced study of Beavers and Joseph [22] that allowed a non-zero tangential velocity (called slip velocity) at the surfaces and uncovered that slip velocity had a broad effect on the bearing performance. Several studies have been documented in the literature about slip velocities for different conditions in bearing systems (Chattopadhyay and Majumdar [23], Shah and Parsania [24], Shah and Patel [25], Venkata et al. [26], Deheri and Patel [27], Patel and Deheri [28], Shah et al. [29], and Mishra et al. [30]).

In their studies, Fragassa et al. [31], Janevski et al. [32] and Geike [33] analysed the theory of static-dynamic load and lubricated contacts, respectively. These investigations confirm that the load profile remains crucial for the bearing design. Patel and Deheri [34] examined the influence of variations of viscosity of the ferrofluid on long bearings. It was noticed that the viscosity variation does not help to increase the LBC in the case of long bearings. Patel and Deheri [35] presented a comparison of a porous structure on shliomis-model-based ferrofluid lubrication of a squeeze film between rotating rough-curved circular plates. It has been ascertained that the Kozeny-Carman model has an edge over the Irmay's model in improving the LBC. A study of thin film lubrication at nanoscale appears in Patel and Deheri [36], where a ferrofluid-based infinitely long rough porous slider bearing has been considered. It has been found that the magnetic fluid induced a higher load and showed a further improvement when the thin film lubrication at nanoscale took place.

Very few studies have been made regarding the ferrofluid lubrication in multi-layered porous plates in the presence of slip velocity. And even lesser amount of studies has been done concerning the comparative studies on the performance of ferrofluid lubricated porous squeeze film in the multi-layered bearing system considering slip velocity. Thus, it was thought proper to put forward a comparative study regarding the performance of a ferrofluid-based squeeze film in two-layered porous annular plates when the slip velocity is taken into account. To what extent can the ferrofluid lubrication counter the adverse effect of porosity and slip velocity? This fundamental question has been addressed while presenting the comparison.

2. Analysis

Figure 1 involves two annular disks (inner and outer radius b and a, respectively ($b < a$)) with curved (exponential and hyperbolic film) upper surface and flat lower surface.

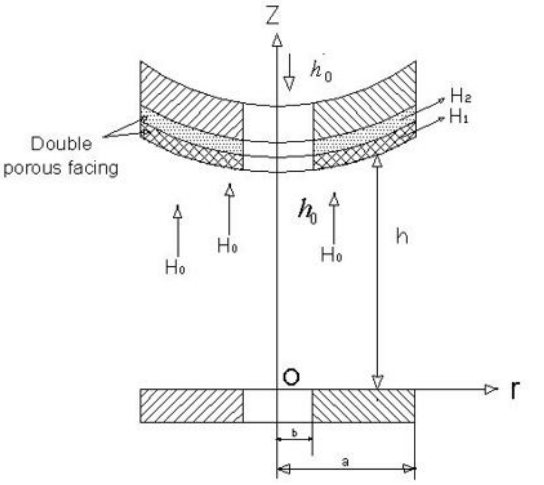

Figure 1. Diagram of the porous annular bearing

In view of Murti [37], Shah and Bhat [2] and Patel and Deheri [38], the thickness profile h of the film is assumed as

$$h(r) = h_0 e^{-\beta r^2},\ b \leq r \leq a$$

for the exponential and

$$h(r) = \frac{h_0}{1+\beta r},\ b \leq r \leq a \tag{1}$$

for the hyperbolic profile.

As per the discussions of Shliomis [39] and Kumar [40], and neglecting the assumptions of Shukla and Kumar [41], the governing equations for the flow of FF as suggested by Shliomis [39] are

$$-\nabla p + \eta \nabla^2 \overline{q} + \mu_0 (\overline{M} \cdot \nabla) \overline{H} + \frac{1}{2\tau_s} \nabla \times (\overline{S} - I\overline{\Omega}) = 0 \tag{2}$$

$$\overline{S} = I\overline{\Omega} + \mu_0 \tau_s (\overline{M} \times \overline{H}), \tag{3}$$

$$\overline{M} = M_0 \frac{\overline{H}}{H} + \frac{\tau_B}{I} (\overline{S} \times \overline{M}), \tag{4}$$

with the continuity equation ($\nabla \cdot \overline{q} = 0$), equations of Maxwell $\nabla \times \overline{H} = 0$, $\nabla \cdot (\overline{H} + \overline{M}) = 0$ and $\overline{\Omega} = \frac{1}{2} \nabla \times \overline{q}$ (Bhat [42]).

Above mentioned equation(2) reduces to

$$-\nabla p + \eta \nabla^2 \overline{q} + \mu_0 (\overline{M} \cdot \nabla) \overline{H} + \frac{1}{2} \mu_0 \nabla \times (\overline{M} \times \overline{H}) = 0 \tag{5}$$

and

$$\overline{M} = \frac{M_0}{H} \left[\overline{H} + \overline{\tau} (\overline{\Omega} \times \overline{H}) \right],$$

where

$$\overline{\tau} = \frac{\tau_B}{1 + \dfrac{\mu_0 \tau_B \tau_s}{I} M_0 H}$$

with the help of equations (3) and (4), as given in Shliomis [39].

Equation(5) takes the following form, as discussed in Bhat [42] and Patel and Patel [43] with u, $\overline{H} = (0, 0, H_0)$ and an axially symmetric flow,

$$\frac{\partial^2 u}{\partial x^2} = \frac{1}{\eta(1+\tau)} \frac{\mathrm{d}p}{\mathrm{d}r} \tag{6}$$

where

$$\tau = \frac{3}{2} \phi \frac{\xi - \tan h\xi}{\xi + \tan h\xi}.$$

Because of Beavers and Joseph's [22] slip boundary conditions

$$u(z = 0) = 0,$$
$$u(z = h) = -\frac{1}{s} \frac{\partial u}{\partial z},$$
$$\eta_a = \eta(1 + \tau),$$

the solution of equation (6) can be transformed to

$$u = -\frac{1}{\eta_a} \frac{z^2 - zsh(z-h)}{2(1+sh)} \frac{\mathrm{d}p}{\mathrm{d}r}. \tag{7}$$

With the help of the above expression (7), one can find the continuity equation $\left(\frac{1}{r}\frac{\mathrm{d}}{\mathrm{d}r}\int_0^h ru\,dz + w_h - w_0 = 0\right)$, as

$$\frac{1}{r}\frac{\mathrm{d}}{\mathrm{d}r}\left(\frac{h^3 r(2+sh)}{1+sh}\frac{\mathrm{d}p}{\mathrm{d}r}\right) = 12\eta_a(w_h - w_0). \tag{8}$$

Assuming the upper surface having a double layered porous facing and the lower flat surface being solid in the annular plate bearing.

In the present study, P_1 and P_2 of the porous region satisfy the following equations, respectively (Bhat [42]),

$$\begin{aligned}&\frac{1}{r}\frac{\partial}{\partial r}\left(\frac{\partial P_1}{\partial r}\right) + \frac{\partial^2 P_1}{\partial z^2} = 0 \quad \text{and}\\ &\frac{1}{r}\frac{\partial}{\partial r}\left(\frac{\partial P_2}{\partial r}\right) + \frac{\partial^2 P_2}{\partial z^2} = 0.\end{aligned} \tag{9}$$

Using the Morgan-Cameron approximation, one gets

$$\begin{aligned}\left(\frac{\partial P_1}{\partial z}\right)_{z=h_1} &= \frac{H_1}{r}\frac{\mathrm{d}}{\mathrm{d}r}\left(r\frac{\mathrm{d}p}{\mathrm{d}r}\right),\\ \left(\frac{\partial P_2}{\partial z}\right)_{z=h_2} &= \frac{H_2}{r}\frac{\mathrm{d}}{\mathrm{d}r}\left(r\frac{\mathrm{d}p}{\mathrm{d}r}\right).\end{aligned} \tag{10}$$

Since the lower surface is solid and the upper surface has a double layer porous facing, the velocity component along z-direction is

$$\begin{aligned}w_0 &= 0\\ w_h &= \dot{h}_0 - \left[\frac{k_1}{\eta_a}\left(\frac{\partial P_1}{\partial z}\right)_{z=h_1}\right.\\ &\qquad \left. + \frac{k_2}{\eta_a}\left(\frac{\partial P_2}{\partial z}\right)_{z=h_2}\right].\end{aligned} \tag{11}$$

Incorporating equation (9) and (10), equation (11) turns into

$$\begin{aligned}w_0 &= 0\\ w_h &= \dot{h}_0 - \left[\frac{k_1}{\eta_a}\left(\frac{H_1}{r}\frac{\mathrm{d}}{\mathrm{d}r}\left(r\frac{\mathrm{d}p}{\mathrm{d}r}\right)\right)\right.\\ &\qquad \left. + \frac{k_2}{\eta_a}\left(\frac{H_2}{r}\frac{\mathrm{d}}{\mathrm{d}r}\left(r\frac{\mathrm{d}p}{\mathrm{d}r}\right)\right)\right].\end{aligned} \tag{12}$$

Using equation (12), and $\eta_a = \eta_0\left(1+\frac{5}{2}\phi\right)(1+\tau)$, equation (8) yields

$$\begin{aligned}&\frac{1}{r}\frac{\mathrm{d}}{\mathrm{d}r}\left(\left\{\frac{h^3(2+sh)}{1+sh} + 12k_1H_1 + 12k_2H_2\right\}r\frac{\mathrm{d}p}{\mathrm{d}r}\right)\\ &\qquad = 12\eta_0\left(1+\frac{5}{2}\phi\right)(1+\tau)\dot{h}_0.\end{aligned} \tag{13}$$

Upon introduction of the non-dimensional measures:

$$\begin{aligned}R &= \frac{r}{b},\\ \overline{h} &= \frac{h}{h_0},\\ \overline{\beta} &= \beta b^2\,\text{(exponential)},\\ \overline{\beta} &= \beta b\,\text{(hyperbolic)},\\ P &= -\frac{{h_0}^3 p}{\eta_0 b^2 \dot{h}_0},\\ \overline{s} &= sh_0,\\ \psi_1 &= \frac{k_1 H_1}{{h_0}^3},\\ \psi_2 &= \frac{k_2 H_2}{{h_0}^3},\end{aligned} \tag{14}$$

and using above equation (14), equation (13) transforms to

$$\begin{aligned}&\frac{1}{R}\frac{\mathrm{d}}{\mathrm{d}R}\left\{\left[\frac{\overline{h}^3(2+\overline{s}\overline{h})}{1+\overline{s}\overline{h}} + 12(\psi_1+\psi_2)\right]R\frac{\mathrm{d}P}{\mathrm{d}R}\right\}\\ &\qquad = -12\left(1+\frac{5}{2}\phi\right)(1+\tau).\end{aligned} \tag{15}$$

Considering boundary conditions of annular plates,

$$P(1) = P(k) = 0, \tag{16}$$

one can find the dimensionless P as

$$P = \int_1^R\left(-\frac{6ER}{G}\right)dR + C_1\int_1^R\left(\frac{1}{GR}\right)dR, \tag{17}$$

where

$$C_1 = \frac{\int_1^k\left(\frac{6ER}{G}\right)dR}{\int_1^k\left(\frac{1}{GR}\right)dR},$$

$$G = \frac{\overline{h}^3(2+\overline{s}\overline{h})}{1+\overline{s}\overline{h}} + 12(\psi_1+\psi_2),$$

$$E = \left(1+\frac{5}{2}\phi\right)(1+\tau),$$

while the non-dimensional LBC of the annular plates can be found as,

$$\begin{aligned}\overline{W} &= -\frac{{h_0}^3 W}{2\pi\eta_0 b^4\dot{h}_0} = \int_1^k RP\,dR\\ &= -\frac{1}{2}\left(\int_1^k -\frac{6ER^3}{G}\,dR + C_1\int_1^k\frac{R}{G}\,dR\right)\end{aligned} \tag{18}$$

3. RESULT AND DISCUSSION

The results for the double-layered porous medium and slip velocity on exponential and hyperbolic film profiles of the annular bearing are discussed in this section. Equation (17) establishes the non-dimensional pressure, while equation (18) represents a dimensionless LBC. In addition, expression (18) is linear in terms of the magnetization parameter, which indicates an improvement of the LBC of annular plates mathematically.

As far as LBC is concerned, a comparison of the film profile is exhibited graphically in Figures 2–13 with double-porous facing in the occurrence of a slip. The first figure demonstrates the exponential film shape and the second figure depicts the impact of the hyperbolic profile. The performance of appearance of the Shliomis' FF lubricated double porous medium annular plates is based on the foundation of several non-dimensional parameters like magnetization, upper plate's curvature, porosity, volume concentration and slip velocity. It can be observed that the exponential film fares better.

It is noticed that equation (18) suggests the LBC of a single layer porous medium when $\psi_2 \to 0$. With $\psi_1 \to 0$ and $\psi_2 \to 0$, this investigation transfers to the non-porous FF based annular bearing system with the slip velocity. Also, this study reduces to a study of a traditional annular bearing by removing the effect of magnetization in the absence of the slip.

For the range of the parameters, one can refer below: τ: 0.1–0.5, ϕ: 0.01–0.05, $\overline{\beta}$: 1.5–1.9, $1/\overline{s}$: 0.02–0.1, ψ_1: 0.001–0.005 and ψ_2: 0.001–0.005.

The dispensation of LBC about the τ, for numerous values of ϕ, $\overline{\beta}$, ψ_1, ψ_2 and $1/\overline{s}$ shown in Figures 2–5, recommends that the LBC rises strictly due to the FF lubricant. A closer examination of the figures emphasizes that the functionality of bearing systems as well as the increase in load is connected with all the parameters for both the film profiles. Exponential film profile registers a higher load as compared to the hyperbolic shape in Figures 2–5.

The behaviour of the volume concentration parameter concerning various parameters of LBC is illustrated in Figures 6–8, respectively. Due to the rise of the volume concentration parameter, the effect of LBC decreases with porosity (in Figure 7) and slip velocity (in Figure 8), while the effect of $\overline{\beta}$ (in Figure 6) increases the LBC. Moreover, Figure 8 suggests a marginally improved effect of the slip velocity in an exponential film bearing, which indicates an enhancement of the overall annular bearing's performance up to some extent.

The profile of a non-dimensional LBC with respect to the $\overline{\beta}$ is described in Figures 9–11. If we increase the $\overline{\beta}$, then the capacity of the load is growing sharply in the case of the hyperbolic function, while a reverse behaviour is observed with porosity and slip velocity. However, the LBC increases slightly for the exponential profile and follows the same trends for the parameters mentioned above. One can visualize an identical scenario for the curvature of exponential and hyperbolic functions, which is shown in Figures 9–11.

The effect of the porosity on the load distribution of the bearing is shown in Figures 12 and 13. In Figure 12, the effect of slip velocity is negligible for the exponential profile. However, Figure 13 suggests that the trends of both the porosity parameters are almost the same. Both layers help to improve the lifespan of the system by creating a film layer between the surfaces.

The graphical representation makes it clear that the following takes place.

(1.) The nature of both porous facings is almost the same with the same values ($\psi_1 = \psi_2$), however, that does not apply when the porosity values differ. (meaning $\psi_1 > \psi_2$ or $\psi_1 < \psi_2$).

(2.) Figure 13 displays the maximum load among all the figures, which means the double porous layer improves the LBC in annular plates bearing systems.

(3.) Higher values of curvature parameter have a negligible effect on the LBC in the case of the exponential profile, but it does reflect on the LBC in the case of the hyperbolic film profile.

(4.) The effect of slip velocity is satisfactory for the exponential surface profile as compared to the hyperbolic surface.

(5.) Finally, this study helps to improve the LBC by considering the proper selection of all parameters and film shapes while designing the bearing system of annular plates.

4. Conclusion

The effect of the double-porous layered on MF lubricated curved annular bearing is investigated theoretically with the theory of Shliomis' flow model of FF, modified Darcy's law for double layer, and Beavers and Joseph's more realistic slip conditions. In view of the bearing's life period, it is evident that some of the parameters appear to have an opposite effect on the performance of the bearing system. Hence, this investigation clarifies that while designing the bearing system, the porosity in two layers, and the slip velocity must be considered. Interestingly, numerous factors (like porosity and slip velocity) disturb the system adversely even though the bearing can support a load without flow, this does not apply in the case of traditional lubricants. Even the upper plate's curvature, either exponential or hyperbolic, may significantly impact the performance of this bearing system, considering the moderate values of volume concentration, slip velocity, and porosity. Lastly, the exponential film profile exhibits a higher load-bearing capacity, in the case of the double-layered porosity with Shliomis' magnetic fluid flow when slip is in place. A pertinent question is to elevate this analysis by incorporating the effect of surface roughness and deformation. An immediate concern is to carry out this analysis for some other types of bearing systems including the circular ones with slip velocity.

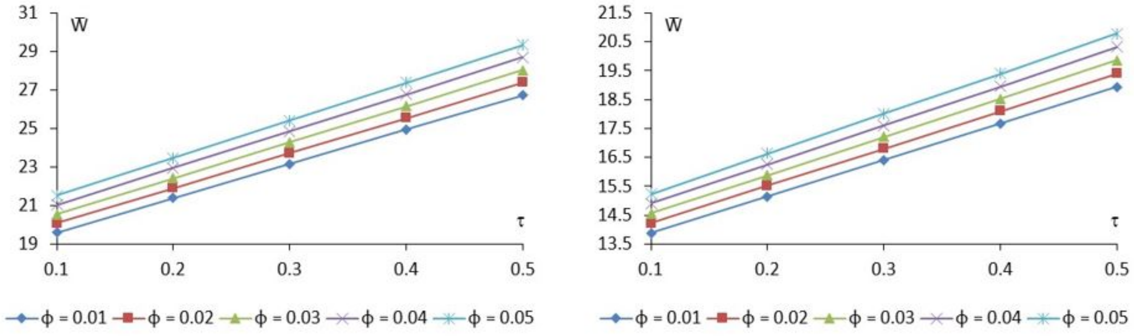

Figure 2. Variation of LBC as regards of τ and ϕ.

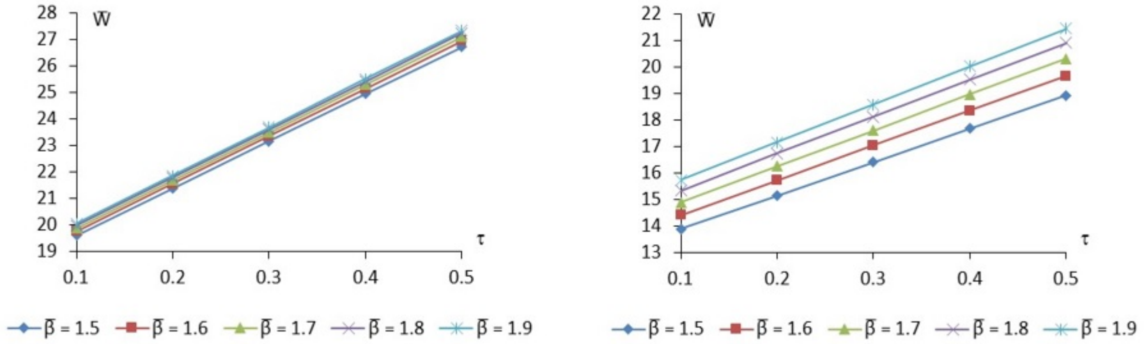

Figure 3. Variation of LBC as regards of τ and $\overline{\beta}$.

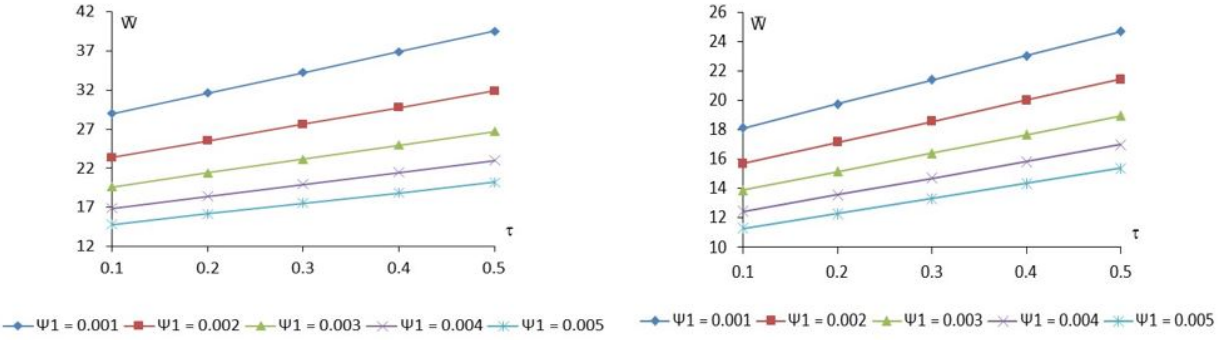

Figure 4. Variation of LBC as regards of τ and ψ_1.

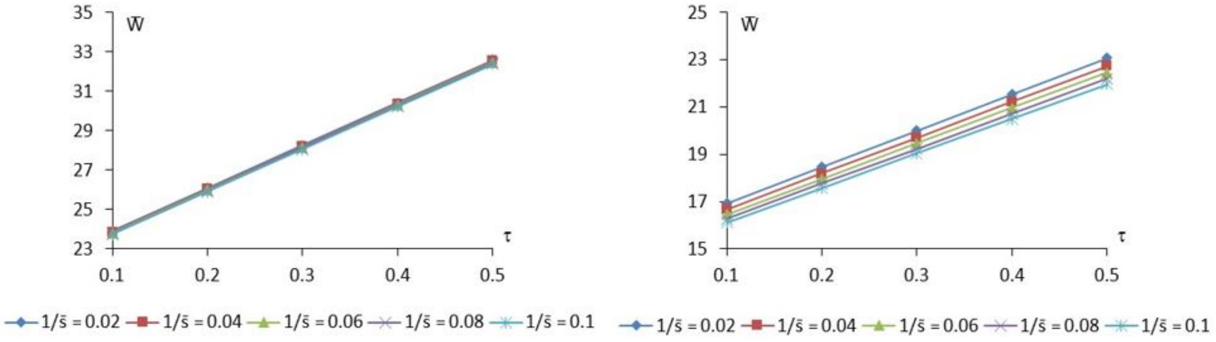

Figure 5. Variation of LBC as regards of τ and $1/\overline{s}$.

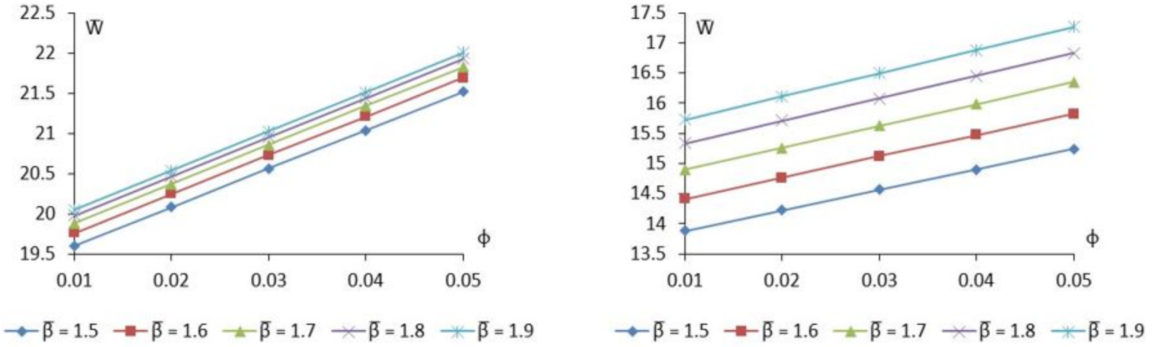

Figure 6. Variation of LBC as regards of ϕ and $\overline{\beta}$.

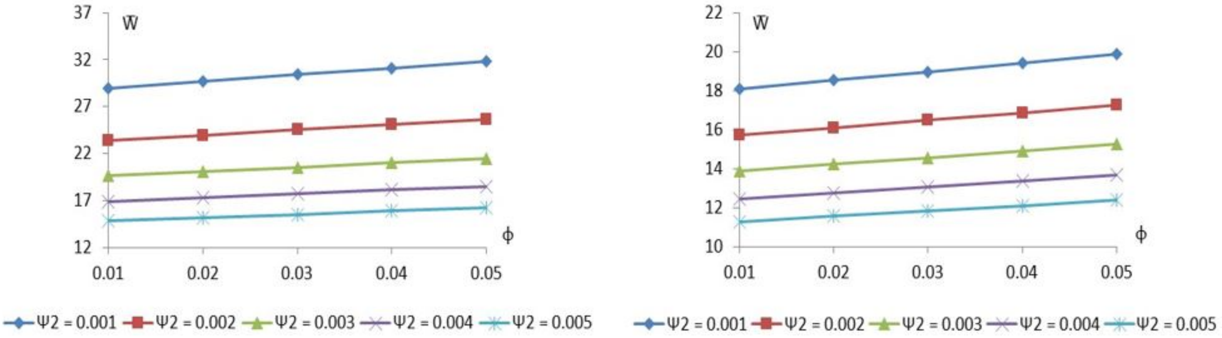

Figure 7. Variation of LBC as regards of ϕ and ψ_2.

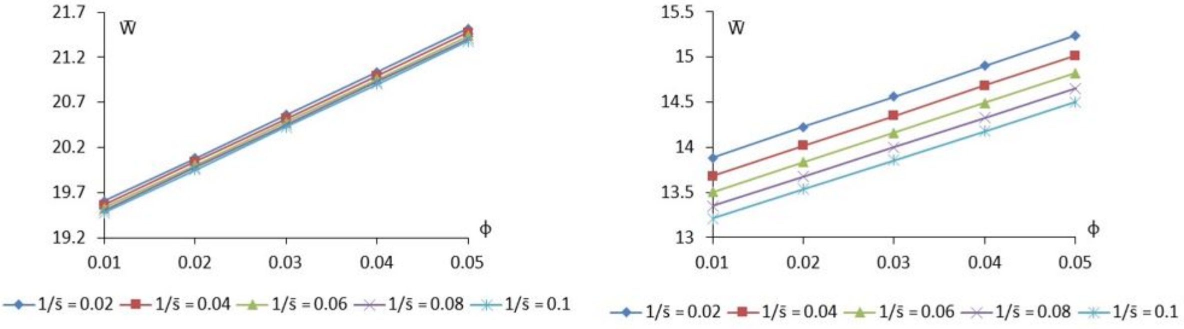

Figure 8. Variation of LBC as regards of ϕ and $1/\overline{s}$.

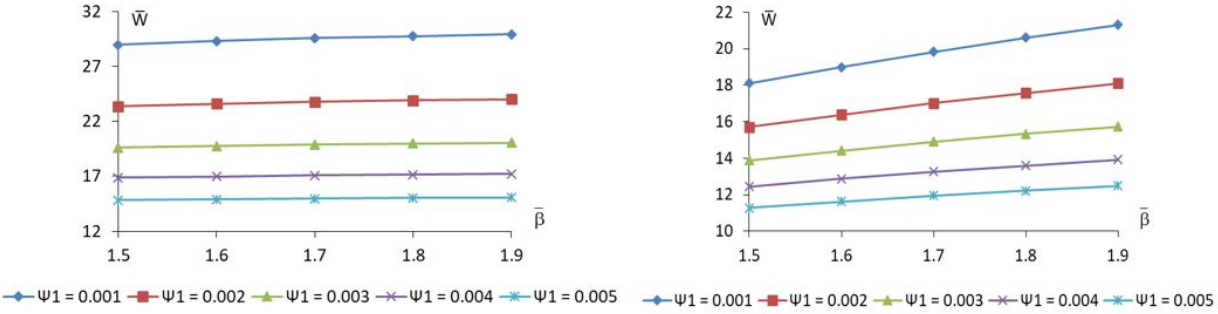

Figure 9. Variation of LBC as regards of $\overline{\beta}$ and ψ_1.

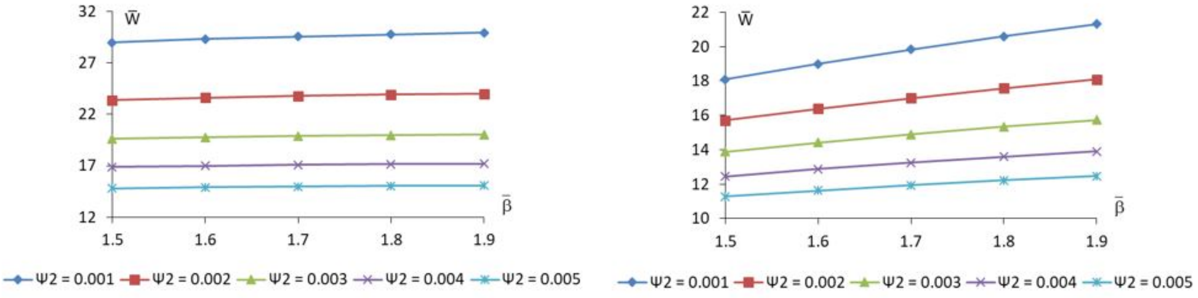

Figure 10. Variation of LBC as regards of $\overline{\beta}$ and ψ_2.

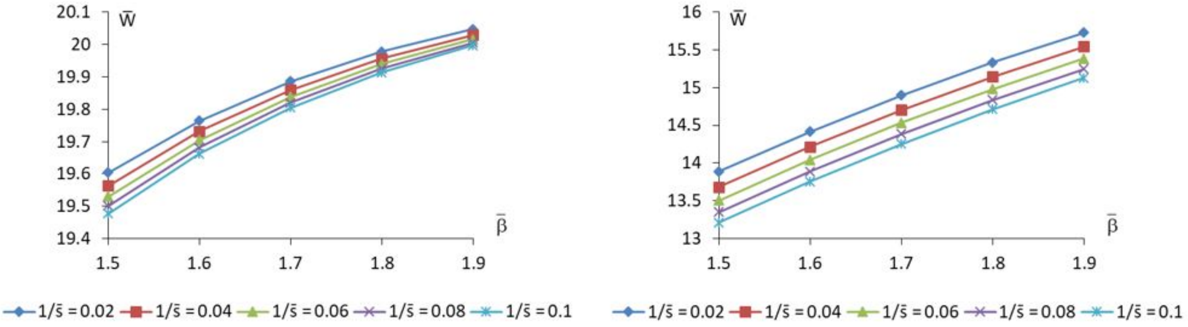

Figure 11. Variation of LBC as regards of $\overline{\beta}$ and $1/\overline{s}$.

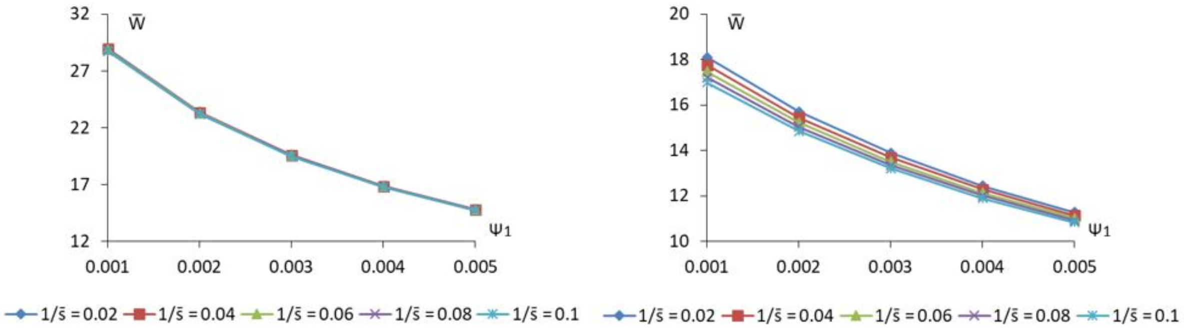

Figure 12. Variation of LBC as regards of ψ_1 and $1/\overline{s}$.

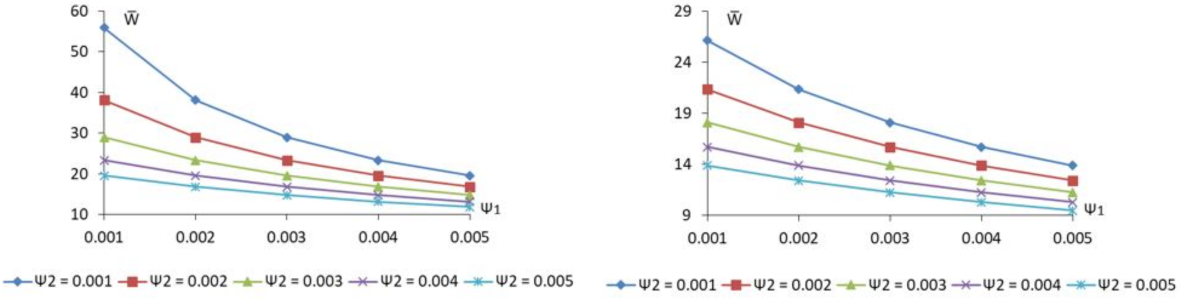

Figure 13. Variation of LBC as regards of ψ_1 and ψ_2.

List of symbols

a	Outer radius of annular plates
b	Inner radius of annular plates
h	Film thickness
r	Radial coordinates
p	Pressure of fluid
u	x – component of $\overline{q}$
w	z – component of $\overline{q}$
H	Magnitude of $\overline{H}$
I	A sum of moments of inertia of the particles per unit volume
$\overline{s}$	Slip velocity
$\overline{q}$	Fluid velocity in the film region
$\overline{M}$	Magnetization vector
$\overline{H}$	An identical magnetic field
$\overline{S}$	Internal angular momentum
h_0	Central film thickness
w_0, w_h	Values of w at $z = 0$, h respectively
h_1	Thickness of lubricant in the inner layer
h_2	Thickness of lubricant in the outer layer
k_1	Permeability of inner layer of the porous region
k_2	Permeability of outer layer of the porous region
M_0	Equilibrium magnetization
H_0	Constant magnetic field
H_1	Thickness of the inner layer adjacent to lubricant layer
H_2	Thickness of the outer layer adjacent to solid wall
P_1	Pressure of inside layer in the porous region
P_2	Pressure of outside layer in the porous region
η	Viscosity of suspension
β	Curvature of the upper plate
ξ	Langevin's parameter
τ	Magnetization parameter
ϕ	Volume concentration
τ_B	Brownian relaxation time parameter
τ_S	Relaxation time parameter
μ_0	Permeability of free space
η_0	Carrier fluid viscosity
ψ_1	Inner layer porous structure parameter
ψ_2	Outer layer porous structure parameter

References

[1] J. Lin. Magneto-hydrodynamic squeeze film characteristics between annular disks. *Industrial Lubrication and Tribology* **53**(2):66–71, 2001. `https://doi.org/10.1108/00368790110384028`.

[2] R. Shah, M. Bhat. Ferrofluid squeeze film between curved annular plates including rotation of magnetic particles. *Journal of Engineering Mathematics* **51**(4):317–324, 2005. `https://doi.org/10.1007/s10665-004-1770-9`.

[3] N. Bujurke, N. Naduvinamani, D. Basti. Effect of surface roughness on the squeeze film lubrication between curved annular plates. *Industrial Lubrication and Tribology* **59**(4):178–185, 2007. `https://doi.org/10.1108/00368790710753572`.

[4] G. Deheri, R. Patel, N. Abhangi. Magnetic fluid-based squeeze film behavior between transversely rough curved annular plates: A comparative study. *Industrial Lubrication and Tribology* **63**(4):254–270, 2011. `https://doi.org/10.1108/00368791111140477`.

[5] S. Fatima, T. Biradar, B. Hanumagowda. Magneto-hydrodynamics couple stress squeeze film lubrication of rough annular plates. *International Journal of Current Research* **9**(9):58007–58014, 2017.

[6] G. Hanumagowda, B.and Savitramma, A. Salma, Noorjahan. Combined effect of piezo-viscous dependency and non-newtonian couple stresses in annular plates squeeze-film characteristics. *Journal of Physics: Conference Series* **1000**(1):1–8, 2018. `https://doi.org/10.1088/1742-6596/1000/1/012083`.

[7] L. Ting. Engagement behavior of lubricated porous annular disks. part i: Squeeze film phase - surface roughness and elastic deformation effects. *Wear* **34**(2):159–172, 1975. `https://doi.org/10.1016/0043-1648(75)90062-9`.

[8] J. Gupta, K. Vora, M. Bhat. The effect of rotational inertia on the squeeze film load between porous annular curved plates. *Wear* **79**:235–240, 1982. `https://doi.org/10.1016/0043-1648(82)90171-5`.

[9] M. Bhat, G. Deheri. Squeeze film behaviour in porous annular discs lubricated with magnetic fluid. *Wear* **151**(1):123–128, 1991. `https://doi.org/10.1016/0043-1648(91)90352-u`.

[10] R. Shah, S. Tripathi, M. Bhat. Magnetic fluid based squeeze film between porous annular curved plates with the effect of rotational inertia. *Pramana - Journal of Physics* **58**(3):545–550, 2002. `https://doi.org/10.1007/s12043-002-0064-x`.

[11] M. Shimpi, G. Deheri. A study on the performance of a magnetic fluid based squeeze film in curved porous rotating rough annular plates and deformation effect. *Tribology International* **47**:90–99, 2012. `https://doi.org/10.1016/j.triboint.2011.10.015`.

[12] J. Patel, G. Deheri. Theoretical study of shliomis model based magnetic squeeze film in rough curved annular plates with assorted porous structures. *FME Transactions* **42**(1):56–66, 2014. `https://doi.org/10.5937/fmet1401056p`.

[13] P. Rao, S. Agarwal. Couple stress fluid-based squeeze film between porous annular curved plates with the effect of rotational inertia. *Iranian Journal of Science and Technology, Transactions A: Science* **41**(4):1171–1175, 2017. `https://doi.org/10.1007/s40995-017-0295-9`.

[14] K. Vasanth, J. Hanumagowda, J. Santhosh Kumar. Combined effect of piezoviscous dependency and non-newtonian couple stress on squeeze-film porous annular plate. *Journal of Physics: Conference Series* **1000**(1):1–8, 2018. `https://doi.org/10.1088/1742-6596/1000/1/012080`.

[15] R. Shah, D. Patel, D. Patel. Ferrofluid-based annular squeeze film bearing with the effects of roughness and micromodel patterns of porous structures. *Tribology - Materials, Surfaces & Interfaces* **12**(4):208–222, 2018. `https://doi.org/10.1080/17515831.2018.1542192`.

[16] P. Kumar, D.and Sinha, P. Chandra. Ferrofluid squeeze film for spherical and conical bearings. *International Journal of Engineering Science* **30**(5):645–656, 1992. `https://doi.org/10.1016/0020-7225(92)90008-5`.

[17] P. Sinha, P. Chandra, D. Kumar. Ferrofluid lubrication of cylindrical rollers with cavitation. *Acta Mechanica* **98**:27–38, 1993. `https://doi.org/10.1007/bf01174291`.

[18] R. Shah, M. Bhat. Ferrofluid squeeze film in a long journal bearing. *Tribology International* **37**:441–446, 2004. `https://doi.org/10.1016/j.triboint.2003.10.007`.

[19] J. Patel, G. Deheri. Performance of a ferrofluid based rough parallel plate slider bearing: A comparison of three magnetic fluid flow models. *Advances in Tribology* **2016**:1–9, 2016. `https://doi.org/10.1155/2016/8197160`.

[20] R. Shah, R. Shah. Derivation of ferrofluid lubrication equation for slider bearings with variable magnetic field and rotations of the carrier liquid as well as magnetic particles. *Meccanica* **53**(4-5):857–869, 2017. `https://doi.org/10.1007/s11012-017-0788-9`.

[21] M. Munshi, A. Patel, G. Deheri. Lubrication of rough short bearing on shliomis model by ferrofluid considering viscosity variation effect. *International Journal of Mathematical, Engineering and Management Sciences* **4**(4):982–997, 2019. `https://doi.org/10.33889/ijmems.2019.4.4-078`.

[22] G. Beavers, D. Joseph. Boundary conditions at a natural permeable wall. *Journal of Fluid Mechanics* **30**(1):197–207, 1967. `https://doi.org/10.1017/s0022112067001375`.

[23] A. Chattopadhyay, B. Majumdar. Steady state solution of finite hydrostatic porous oil journal bearings with tangential velocity slip. *Tribology International* **17**(6):317–323, 1984. `https://doi.org/10.1016/0301-679x(84)90095-1`.

[24] R. Shah, M. Parsania. Ferrofluid lubrication equation for non-isotropic porous squeeze film bearing with slip velocity. *Mathematics today* **28**(2):43–49, 2012.

[25] R. Shah, D. Patel. Squeeze film based on ferrofluid in curved porous circular plates with various porous structure. *Applied Mathematics* **2**(4):121–123, 2012. `https://doi.org/10.5923/j.am.20120204.04`.

[26] J. Venkata, R. Murthy, M. Kumar. Effect of slip parameter on the flow of viscous fluid past an impervious sphere. *International Journal of Applied Science and Engineering* **12**(3):203–223, 2014. `https://doi.org/10.6703/IJASE.2014.12(3).203`.

[27] G. Deheri, S. Patel. Combined effect of slip velocity and surface roughness on a magnetic squeeze film for a sphere in a spherical seat. *Indian Journal of Materials Science* **2015**:1–9, 2015. `https://doi.org/10.1155/2015/159698`.

[28] J. Patel, G. Deheri. Numerical modeling of jenkins model based ferrofluid lubrication squeeze film performance in rough curved annular plates under the presence of slip velocity. *Facta Universitatis, Series: Mathematics and Informatics* **31**(1):11–31, 2016.

[29] N. Shah, R.and Patel, R. Kataria. Some porous squeeze film-bearings using ferrofluid lubricant: A review with contributions. *Proceedings of the Institution of Mechanical Engineers, Part J: Journal of Engineering Tribology* **230**(9):1157–1171, 2016. `https://doi.org/10.1177/1350650116629096`.

[30] M. Mishra, S.and Barik, G. Dash. An analysis of hydrodynamic ferrofluid lubrication of an inclined rough slider bearing. *Tribology - Materials, Surfaces & Interfaces* **12**(1):17–26, 2018. `https://doi.org/10.1080/17515831.2017.1418280`.

[31] C. Fragassa, G. Minak, A. Pavlovic. Measuring deformations in the telescopic boom under static and dynamic load conditions. *Facta Universitatis, Series: Mechanical Engineering* **18**(2):315–328, 2020. `https://doi.org/10.22190/FUME181201001F`.

[32] G. Janevski, P. Kozic, A. Pavlovic, S. Posavljak. Moment lyapunov exponents and stochastic stability of a thin-walled beam subjected to axial loads and end moments. *Facta Universitatis, Series: Mechanical Engineering* **19**(2):209–228, 2021. `https://doi.org/10.22190/FUME191127014J`.

[33] T. Geike. Bubble dynamics-based modeling of the cavitation dynamics in lubricated contacts. *Facta Universitatis, Series: Mechanical Engineering* **19**(1):115–124, 2021. `https://doi.org/10.22190/FUME210112027G`.

[34] J. Patel, G. Deheri. Influence of viscosity variation on ferrofluid based long bearing. *Reports in Mechanical Engineering* **3**(1):37–45, 2022. `https://doi.org/10.31181/rme200103037j`.

[35] J. Patel, G. Deheri. Effect of various porous structures on the shliomis model based ferrofluid lubrication of the film squeezed between rotating rough curved circular plates. *Facta Universitatis, Series: Mechanical Engineering* **12**(3):305 – 323, 2014.

[36] J. Patel, G. Deheri. A study of thin film lubrication at nanoscale for a ferrofluid based infinitely long rough porous slider bearing. *Facta Universitatis, Series: Mechanical Engineering* **14**:89–99, 2016. `https://doi.org/10.22190/FUME1601089P`.

[37] P. Murti. Squeeze films in curved porous circular plates. *Journal of Lubrication Technology* **97**(4):650–652, 1975. `https://doi.org/10.1115/1.3452699`.

[38] J. Patel, G. Deheri. Jenkins model based magnetic squeeze film in curved rough circular plates considering slip velocity: A comparison of shapes. *FME Transactions* **43**(2):144–153, 2015. `https://doi.org/10.5937/fmet1502144p`.

[39] M. Shliomis. Effective viscosity of magnetic suspensions. *Soviet Physics – JETP* **34**(6):1291–1294, 1972.

[40] D. Kumar. *Lubrication with a Magnetic fluid.* Ph.D. thesis, IIT Kanpur, 1991.

[41] J. Shukla, D. Kumar. A theory for ferromagnetic lubrication. *Journal of Magnetism and Magnetic Materials* **65**(2-3):375–378, 1987. `https://doi.org/10.1016/0304-8853(87)90075-8`.

[42] M. Bhat. *Lubrication with a Magnetic fluid.* Team Spirit (India) Pvt. Ltd., India, 2003.

[43] N. Patel, J. Patel. Magnetic fluid-based squeeze film between curved porous annular plates considering the rotation of magnetic particles and slip velocity. *Journal of Serbian Society for Computational Mechanics* **14**(2):69–82, 2020. `https://doi.org/10.24874/jsscm.2020.14.02.05`.

LaTeX class errors and warnings

- **Warning:** Article ‘adeshara‘ has [eprint] option
- **Warning:** Article ‘bui‘ has [eprint] option
- **Warning:** Article ‘chudoba‘ has [eprint] option
- **Warning:** Article ‘dibyo‘ has [eprint] option
- **Warning:** Article ‘dittrich‘ has [eprint] option
- **Warning:** Article ‘fomin‘ has [eprint] option
- **Warning:** Article ‘franek‘ has [eprint] option
- **Warning:** Article ‘hahn‘ has [eprint] option
- **Warning:** Article ‘nguyen‘ has [eprint] option
- **Warning:** Article ‘patel‘ has [eprint] option